ERROR CORRECTIONS ON ESTIMATED AERODYNAMIC CHARACTERISTICS OF TRANSONIC TRANSPORT AIRPLANE

UENO Makoto

Abstract

This dissertation aims to improve the methods of estimating aerodynamic characteristics of transport airplanes by both saving the cost in computational fluid dynamics (CFD) and keeping errors in wind tunnel testing (WTT) reasonably small. The results should be used mainly in the preliminary design phase of airplanes including shape optimizations through CFD and its validation through WTT. The dissertation consists of the following three topics.

First, the extrapolated true value of the drag-coefficient C_D of the NASA Common Research Model (CRM) was validated by applying the drag-decomposition method on the flow fields acquired through CFD. The NASA CRM was chosen as the main target of the worldwide campaign for efficient and accurate drag prediction based on the CFD performed with moderate grid density up to a few tens of millions of computational grid points. The present method can remove the "spurious drag", which is an unphysical numerical extra drag production inherent to CFD that necessitates a grid convergence study in which CFD simulations are performed for several grid sizes to extrapolate the true value. As a result, the difference between the C_D value estimated using the present method with every single CFD simulation and that estimated by the conventional extrapolation (Richardson extrapolation using simulations for three grid sizes) is found to be less than 1.5 drag counts. Thus, the increments of the estimated drag used in the analysis are shown to be due to the spurious drag. This implies that an efficient estimation of the true C_D value could be obtained through such a coarse grid as 2.8 million cells.

Furthermore, a new technique is introduced to reduce the computational cost for the profile-drag in the drag-decomposition method. In the conventional drag-decomposition method, iterative computations are necessary to determine the domain that needs to be integrated for the profile-drag, whereas in the new method, it is estimated more efficiently without iteration by using a new boundary layer sensor, which employs the concept of

detecting the boundary layer thickness in the Baldwin–Lomax turbulence model. The accuracy of the new method is validated on the basis of the grid-convergence study and the conventional drag-decomposition method.

Finally, this paper presents the data correction in WTT. A new method is proposed for correcting the error due to the model deformation of the main wings caused by dynamic pressure. In this method, the attack angle to the virtual un-deformable wings is estimated from the measured data of the model deformation, and then the pressure distribution on the main wings are corrected by using the estimated virtual attack angle. The corrected value is integrated to estimate the error in aerodynamic coefficients, such as lift and drag coefficients. The new method reduces the error in the lift coefficient, ΔC_L from 0.060 to 0.019.

The results of this dissertation contribute to the reduction both of cost in CFD and error unavoidable in WTT for the estimation of aerodynamic characteristics of transonic transport airplanes. These include the more accurate and efficient estimation of aerodynamic drag at lower cost using CFD with using the drag decomposition method than with the conventional surface integral, and the estimation of the aerodynamic characteristics of the designed shape in WTT by correcting the model deformation.

Acknowledgments

Acknowledgments for whole dissertation

The present work was conducted in the Fluid Dynamics Laboratory of the Department of Aerospace Engineering at Nagoya University. I would like to express my deepest gratitude and greatest appreciation to my adviser, Prof. Emeritus Y. Nakamura. I am sincerely thankful for his constant encouragement and mentoring during my research. I also wish to thank Associate Professor K. Mori and Assistant Professor (at that time) K. Doi for their valuable suggestions and advice on my research. In particular, Associate Professor Mori kindly took over as principal adviser from Professor Nakamura. Moreover, I am grateful to all the students of the Fluid Dynamics Laboratory for their support. I would like to thank the dissertation referees, Associate Professor Mori, Professors Sasoh and Nagata of the same department, Professor Tsuji of the Department of Energy Engineering and Science, and Associate Professor Kitamura from Yokohama National University.

Furthermore, I would like to express great thanks to my colleagues at the Japan Aerospace Exploration Agency (JAXA). They have been very understanding of my research activity at Nagoya University and provided considerable support. Finally, I express my great thanks to my parents for their encouragement and warm support during my studies.

Acknowledgments for Chapter 2

I thank Dr. Norikazu Sudani of JAXA for his support in continuing this study.

Acknowledgments for Chapter 3

I sincerely appreciate the effort of a former Nagoya University graduate student, Mr. Yasunori Shibata, who helped me construct the computational grids used in this Chapter.

Acknowledgments for Chapter 4

I gratefully acknowledge Ms. Melissa B. Rivers of NASA Langley Research Center for providing essential advice that allowed us to fabricate a copy of the NASA CRM wind tunnel model in JAXA. She and the staff of the National Transonic Facility of NASA kindly gave us practical information about their own model. The author express appreciation to Dr. John C. Vassberg of the Boeing Company for cleaning up the surface data of the nose part of the NASA CRM, to Mr. Kentaro Tanaka and Mr. Tohru Hirai for their support, mainly in computational operations, and to Dr. Kanako Yasue and Dr. Kentaro Imagawa for their long-term efforts on output definitions of JAXA's CRM test campaigns.

Notice

Contents

List of Tables

List of Figures

Nomenclature

A	aspect ratio of main wing
a	speed of sound
$A_{\max}$	maximum cross-sectional area of the body
A^+, C_{kleb}	constants for the Baldwin–Lomax turbulence model
b	reference span length
c	chord length
c_a	two-dimensional axial force coefficient at a wing section
C_D	drag coefficient
c_d	two-dimensional drag coefficient at a wing section
cd	drag coefficient contribution in a computational cell
cd_H	drag coefficient contribution in a computational cell due to enthalpy production
cd_s	drag coefficient contribution in a computational cell due to entropy production
C_f	skin friction coefficient
C_L	lift coefficient
c_l	two-dimensional lift coefficient at a wing section
c_n	two-dimensional normal force coefficient at a wing section
c_p	static pressure coefficient

c_{ref} reference chord

D drag

d reference diameter of the body $\sqrt{(4/\pi)A_{\max}}$

F_x, F_y, F_z, M_x, M_y, and M_z six-component force/moment

F_{bl} boundary-layer function

FF form factor

F_{shock} shock function

H total enthalpy

$\boldsymbol{i}$ unit vector in x–direction

i_H horizontal-tail incidence

L lift

l length of the body

M Mach number

M_{pc} Mach number calculated using plenum chamber static pressure

$\boldsymbol{n}$ unit normal vector pointing outside the control volume

N total number of grid points

n_x x–component of $\boldsymbol{n}$

p_0 total pressure

p_{pc} plenum chamber static pressure

p static pressure

Q component interference factor

q flow of heat through unit area per unit time

R gas constant

Re Reynolds number

Re_c Reynolds number based on the reference chord length c_{ref}

S surface

S_{ref} reference area

S_{wet} wetted area of component

T temperature

t time

t_{wing} thickness of the wing

T_0 total temperature

$\boldsymbol{u}$ velocity vector

U velocity

U_∞ freestream velocity

U_e shear-layer edge velocity

u_τ $\sqrt{\frac{\tau_{\text{wall}}}{\rho}}$

u, v, and w velocity components in the x, y, and z directions, respectively

V control volume

W_A wake region on cut plane

$(x/c)_m$ chord-wise location of the airfoil maximum thickness point

x, y, z cartesian coordinate axes

y^+ dimensionless wall distance in law-of-the-wall, $\frac{\rho_{\text{wall}} u_\tau y}{\mu_{\text{wall}}}$

∂V control volume surface

α attack angle

α_{cs} closure coefficient of Cebeci–Smith turbulence model

Δb spanwise width of a wing section

ΔH total enthalpy increment

Δs entropy increment

Δu velocity increment

δ_v^* boundary layer velocity thickness

η spanwise section location normalized by half-span length $b/2$

γ specific heat ratio

κ Kármán constant

Λ_m sweep of the maximum-thickness line

μ_l molecular viscosity

μ_t eddy viscosity

ν kinematic molecular viscosity, μ/ρ

ψ two–dimensional scalar function

ρ density

$\boldsymbol{\tau}$ viscous stress tensor

τ_{wall} surface shear stress

ξ vorticity magnitude in cut plane

Subscripts

i attributed to lift-induced component

irr attributed to irreversible process

l	laminar
sp	attributed to numerical diffusion
t	turbulent
v	attributed to boundary layer and viscous wake
w	attributed to shock wave
wall	quantity at wall
∞	freestream
A	closed body surface
D	downstream outer boundary
F	upstream and lateral outer boundary

Chapter 1

Introduction

1.1 Increasing Use of Computational Fluid Dynamics in Airplane Design

The accurate estimation of aerodynamic characteristics is essential in airplane development. There are three main methods for estimating airplane aerodynamic characteristics. The first is an empirical method based on the statistical data of airplanes developed in the past [5]. This approach is still important in the concept-study phase of airplane development. The second is the wind tunnel testing (WTT) of scaled models [6] and the third is computational fluid dynamics (CFD). In airplane development, different CFD methods based on different fidelity have been used: the isentropic panel method, inviscid simulations solving the Euler equations, Reynolds-averaged Navier–Stokes (RANS) simulations, large eddy simulations (LES), and direct numerical simulations (DNS) [7, 8]. Currently, RANS codes are mainly used.

In general, the CFD is inferior in terms of accuracy but superior to WTT in terms of turnaround time and cost for small shape modification. Thus, the CFD is especially useful in shape-optimization processes, in which many calculations of various shapes are necessary. Although SpaceShipOne, the first manned private spaceplane, was developed without any WTT [9], in modern airplane development, CFD is applied in such cases as shape optimization, and in special cases in which the WTT is difficult to implement, for example, a full-scale thrust reverser performance test [10], and preliminary computations previous to WTT to plan the WTT conditions and specifications of models [11, 12]. WTT

is used more broadly for validating shape optimizations, parametric studies of aerodynamic models (including the effects of deflection of control surfaces such as elevators and ailerons), and measurement of aerodynamic performance under off-design conditions.

However, according to Garretson [7], necessary cases in WTTs are increasing because of the increase in the design complexity and the demands to reduce the design margins of the modern airplane. The pressure to increase the test number is motivating further usage of CFD. Therefore, it is necessary to validate the reliability of CFD [7]. The issues are summarized by NASA [13].

1.2 Problems Revealed in Drag Prediction Workshops

To improve the reliability of the CFD for airplane development, the Applied Aerodynamics Technical Committee of the American Institute of Aeronautics and Astronautics (AIAA) has been hosting the AIAA CFD Drag Prediction Workshops (DPWs) [14, 15, 16, 4, 17], which provide benchmarks of CFD techniques for drag prediction of transonic transport airplane under cruise conditions. The 4th AIAA CFD DPW (DPW-IV) [4], was epoch-making because of the introduction of the NASA Common Research Model (CRM), which was designed as a typical modern transonic transport similar to Boeing 777-200. So far, the NASA CRM has been tested in different high-precision wind tunnel facilities [18, 19, 20, 21, 22, 23], and the model is now the most widely studied airframe worldwide [24]. The AIAA DPW and the NASA CRM are briefly summarized in Appendix A.

As a result of a series of the DPWs, the following two problems are highlighted. The first problem is the grid dependence of the CFD results, and the second problem is the deformation of the airplane model in WTT.

1.2.1 Grid Dependence Problem in CFD

The grid dependence is an unavoidable problem for the finite volume or finite difference methods, which employ discrete computational grids. As described in the summary of the DPW-IV [4], grid dependence or convergence has been a repetitive theme in the DPW series [25]. In the DPW-II, it was difficult to draw meaningful conclusions with respect to grid convergence because of the separated flow region [4].

The CFD results include unphysical errors [26], which can be ignored when the grid quality is good (without twist or skewness) and the grid density is sufficiently high. Here, the

error implies the difference between the computed drag obtained with a certain set of grids and the expected true value, which is deduced by varying the grid density (grid convergence study). If one could employ billions of grid points for a transonic transport under cruise conditions, the computational results should contain computational error of less than 1 drag count ($C_D = 1 \times 10^{-4}$) [27], which is considered in satisfactory airplane development. However, the computational time needed for such a grid is extremely long. For example, Sclafani *et al.* [27] built grids with approximately 2.4 billion cells; however, it took more than 500,000 s of CPU time to obtain a converged solution for only one case. As it is considered necessary to obtain the CFD results within a day or a few hours during a real airplane development, grid points of up to approximately a few tens of millions are considered practical [4, 17]. By using such a moderate number of grid points, the numerically-calculated drag coefficient obtained by integrating the stress tensor on the surface suffers from the so-called "spurious drag," which is the unphysical drag and originates from the numerical entropy production [28]. To estimate the true drag by using moderate number of grid points, it is necessary to remove the spurious drag contribution from the calculated drag, for which the "drag decomposition method" [29, 30] has been introduced. In the conventional airplane aerodynamics, the drag force exerted on an airplane can be decomposed into three components: profile, wave, and induced drags. The flow around an airplane is especially of a high Reynolds number ($Re > 10^7$). Thus, the profile drag is produced in a small domain including the boundary layer and wake, and the wave drag is produced only in a small domain including the shock wave.

In the drag decomposition method (described in detail in Section 2.2.2), aerodynamic drag exerted on an airplane is first defined as the surface integral of the momentum deficit over the outer boundary of the entire computational domain. With the help of the divergence theorem, the surface integral is converted to volume integral. Consequently, the sum of the profile and wave drags is calculated as the integral of the respective momentum deficit in each computational cell. Next, the profile drag can be calculated as volume integral in a special domain including the boundary layer and wake. The wave drag can be calculated in a special domain including the shock wave. Furthermore, the spurious drag can be considered as the momentum deficit that originated from the cells, except for the two above mentioned domains [28]. The induced drag is computed as the surface integral over the downstream surface including wake. Finally, the spurious-drag-excluded total drag force is estimated as the sum of the three components, that is, the profile, wave, and induced

drags obtained from a coarser grid than the case in which the surface integral was used, unless the grid is not so coarse that its flow structure differs from that of a fine enough grid. The name of the drag decomposition method is derived by considering that the three aforementioned components are separately calculated from the flow field. As the profile and wave drag components are calculated by integrating the cells producing drag, some insights about the drag production can also be obtained by examining where the drag is produced.

1.2.2 Main Wing Deformation in WTT

It is impossible to regenerate the ideal inflow representing real flight conditions, which are simulated in the CFD, in a wind tunnel because of wall interference, support interference, Reynolds number difference, flow angularity (=angular error of free-stream direction), and buoyancy. Hence, it is necessary to correct the WTT data before comparing it with the CFD results. There are several correction techniques of WTT, as described in relevant literature [31]. Such efforts have provided satisfactory results, especially for wall interference [32, 33, 34] and support interference [35, 36]. Typical techniques for the support interference are the so-called image method [37, 38] and correction using CFD [39, 40]. Another important problem is the Reynolds number problem. Except for a few cryogenic wind tunnels, such as the National Transonic Facility (NTF) [41] and the European Transonic Windtunnel (ETW) [42], the Reynolds number simulated in most WTTs is much lower than the design point of the airplane, and the acquired drag is much higher. The wet area correction method is the conventional approach for this problem. This method simply corrects the friction change due to the Reynolds number difference by using empirically corrected wall friction forces for the turbulent boundary layer [5, 43]. More comprehensive approaches, which were discussed by the AGARD Fluid Dynamics Panel 09, are well documented in literature [44, 45, 46].

Although the aforementioned correction methods for WTT have been in practice, the correction of model deformation is still controversial [47, 39, 48, 49, 50, 51]. Although the problem was briefly discussed in a previous study [46], the study did not ascertain the necessity of the model deformation due to dynamic pressure in ordinary WTTs. Serious attempts to solve the problem have appeared recently [47] and the problem drew attention in the DPW-IV [4], which performed critical comparisons between CFD and WTT. Typical transonic transport airplane is equipped with a pair of swept main wings. The main wing of the wind tunnel model is twisted because of the large dynamic pressure of the stream,

reducing the effective attack angle at the span-wise station close to the tip than the originally designed value. The resulting lift and lift-induced drag thus decrease than those of the designed shape, for which CFD computations are usually performed. As shown in Chapter 4, the twist angle due to model deformation during WTT exceeds 1.0° for a typical transport-shape model with a full span of 1.269 m at cruise conditions. This level of twist angle significantly affects the pressure distribution on the main wings [52]. Thus, it is necessary to develop a correction method for model deformation effects.

Conventional correction methods for model deformation employ the CFD results [47, 39, 48, 49, 50, 51]. However, it is apparent that such correction methods based on CFD are not applicable to WTT-based validation of CFD results. Especially, when the flow past a wing is separated significantly, correction methods based on CFD are not expected to work sufficiently. Therefore, new correction methods based solely on the WTT results are required.

1.3 Subjects in Dissertation

1.3.1 Drag Decomposition Study of the NASA CRM

1.3.1.1 Spurious Drag Removal

Chapter 2 reveals the influence of the spurious drag on grid convergence characteristics of CFD results of the NASA CRM by the application of the drag decomposition method. As stated in Section 1.2.1, grid convergence has been a repetitive theme in the DPW series [25]. Nevertheless, previous studies did not analyze the cause of the aerodynamic drag variations of the DPW results due to grid density. However, in the current study, the author performed the analysis on results [53] of the DPW-IV [54]. The drag variations of the CFD results might be caused by spurious drag or numerical error, or flow structure corruption due to the use of extremely coarse grids; the drag-decomposition method would be able to clarify which of these causes the variations. The objectives of the chapter is to reveal the cause of the drag variations in the DPW-IV, which is recently the most important benchmark result for transonic transport aircrafts. The drag-decomposition method can be used to remove the spurious drag. The agreement between the drag without spurious drag and the estimated value obtained using the conventional Richardson extrapolation method implies its validity as the true drag value through CFD. However, if drag variations due to the grid

density remain, the flow structure might be corrupted because of extremely low grid density. Note that the drag-decomposition method can visualize the drag production distribution as well because it integrates the momentum deficits in each computational cell. This could give an insight about drag productions in flow fields. Therefore, in this study, the CFD drag without spurious drag was quantitatively examined and the drag production in the flow fields was qualitatively observed. The obtained results could encourage attempts of estimating the aerodynamic drag through CFD, such as the DPWs, which have important impacts on the industrial CFD drag estimation of airplanes.

1.3.1.2 Improvement of Drag Decomposition Procedure

The basic concept for domain selection in the drag decomposition method was established by one of the author's collaborator, Tognaccini [29, 26]. Most of the studies, so far, have employed his method[26, 55]. However, iterative calculations (which are time consuming) are necessary for determining the profile-drag domain (including the boundary-layer and wake) and wave-drag domain. The present study (in Chapter 3) also proposes a new method for determining the profile-drag domain without iterative calculation; this method sometimes needs more than 100 iterations. In the new method, a technique based on the Baldwin–Lomax turbulence model [56] is introduced to determine the height of the boundary layer without any iterations. In addition, the domain within the determined boundary layer height is determined as the profile drag domain.

The new method results in significant cost reductions for drag decomposition analysis. The domain captured using the new method is validated through a comparison with the conventional method.

1.3.2 New Correction Method for Main Wing Deformation in WTT

Chapter 4 is devoted to the explication of a new correction method of WTT to solve the main wing deformation problem described in Section 1.2.2. The effect of the main wing deformation was corrected only according to the measured deformation data and its pressure distributions. Pressure data on each wing section were corrected using optically measured deformation data. Then, the corrected pressure distributions were integrated to correct the lift force. As only the twist changes are significant for aerodynamic characteristics [39], the bending of the wings was not considered in this analysis.

Chapter 2

Drag Decomposition of Transonic Transport

2.1 Introduction

As introduced in Chapter 1, the drag decomposition method is applied to CFD flow fields around the NASA CRM. The NASA CRM is a shape for aerodynamic analysis of contemporary transonic transport, which was developed for the 4th AIAA DPW (DPW–IV) [4] in 2009. The geometry of the NASA CRM is publicly available, and it has been widely used for performing aerodynamic research for transonic transport not only in numerical researches summarized in [4, 17] but also in experimental activities [18, 19, 57, 39, 58, 11, 59, 60]. Description of the DPW–IV and the NASA CRM are summarized in Appendix A.1.

The drag decomposition method, or the far-field method, has some advantages over the conventional surface integral, or the near-field method, for the postprocessing of the CFD. As its name indicates, it can decompose the drag exerted on the airplane into the components such as the profile, wave, and lift-induced drags. Although the theory of the drag decomposition method is described in Section 2.2.2, profile and wave drag components are calculated as volume integrals of momentum deficit. Moreover, the lift-induced drag for a 3-D flow is usually calculated separately by using Maskell's method [61, 62] as the surface integral of induced momentum due to lift on a Trefftz plane [63]. The drag decomposition method can also remove the "spurious drag" [28], which is an unphysical numerical drag production inherent to CFD because of a numerical error with finite computational grid used in the simulations.

In this chapter, drag decomposition analysis is performed on CFD flow fields around the NASA CRM. Next, the method is used to show that the aerodynamic drag of the NASA CRM estimated by Richardson extrapolation in a grid convergence study does not include spurious drag. The method also includes the procedure of drag decomposition which is related to the second study described in Chapter 3. Moreover, as an application of the drag decomposition method, contribution of each drag components on drag divergence is revealed using variation of the decomposed drags in increase of the attack angle.

2.2 Methods

2.2.1 CFD Solution

The target flow fields to be analyzed in this drag decomposition study are solutions of the three-dimensional RANS equations of the flow around the NASA CRM provided from a numerical simulation performed by Yamamoto *et al.* [53]. The UPACS [64, 65], which is a standard CFD code for multi-block structured-grids at JAXA based on a cell-centered finite volume method, is used as the flow solver. In the computation, the second-order scheme of Roe's flux difference splitting for convection terms [66] is used with MUSCL extrapolation and van Albada's differentiable limiter [67]. The viscous terms were discretized by the second order central difference. Time integration was conducted using the Matrix Free Gauss-Seidel (MFGS) implicit method [68].

The grid wraps around the geometry near the model surface with an O–O grid topology to guarantee good orthogonality within the boundary layer, and then extends outward with an C–O topology. Fig. 2.1 shows the wire-frame image of the grid blocks around the NASA CRM. The reference quantities for the NASA CRM is tabulated in Table A.1 in Section A.1.2 of Appendix. In the computational space, the scale is nondimensionalized by the mean aerodynamic chord.

Three grid resolution levels (coarse, medium, and fine) were prepared and their details are tabulated in Table 2.1.

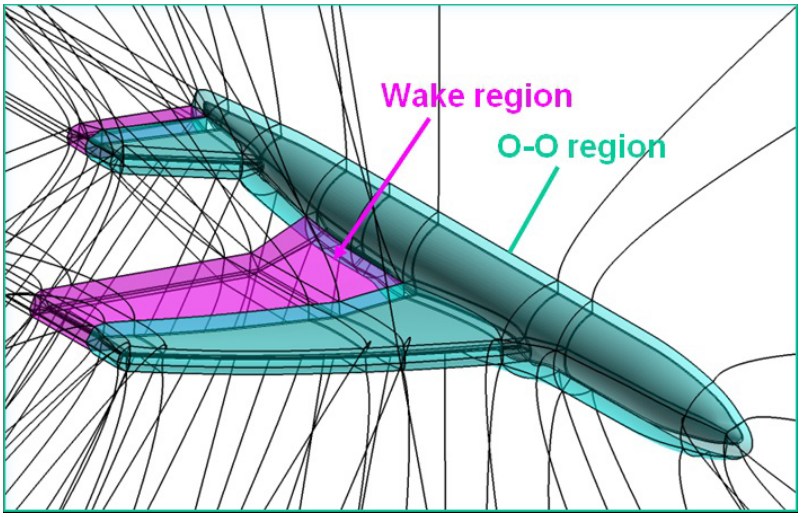

Figure 2.1 Block wire frame around NASA CRM model.

Table 2.1 Multiblock structured grid around NASA Common Research Model.

	Coarse*	Medium	Fine†
Cells	2.8M	9.0M	30.4M
Number of Grid Points (N)	3.2M	9.9M	32.4M
Surface Faces	127K	276K	620K
B.L. 1st-Cell Size [y^+]	1.0	2/3	4/9
B.L. 1st-Cell Size [inch/mm]	1.478e-3 / 0.03754	9.85e-4 / 0.0250	6.57e-4 / 0.0167
B.L. Growth Rate	1.31	1.20	1.13
T.E. Cells	14	20	30

* Based on interpolation of Medium grid.
† Based on interpolation of Medium grid.
"B.L." means "Boundary Layer".
"T.E." means "Trailing Edge of the main wings".

The Spalart–Allmaras one-equation turbulence model [69] is used without the trip term for transition and the *ft2* function, which is intended to suppress production of eddy viscosity due to numerical error. This is because the flow is set fully turbulent in the boundary layer around the airplane (no transition is modelled), and those terms are insignificant when there is no boundary-layer transition. The production of eddy viscosity is initiated using with the free-stream value.

The free-stream Mach number is set to $M_\infty = 0.85$ and the Reynolds number is 5 million. The static temperature is set at 311 K. Solutions for the three grid sizes at a fixed $C_L = 0.5$ are used for grid convergence study, and values of attack angles, $\alpha = 1.5°, 2.0°, 2.5°, 3.0°$, and 4.0° are examined only for the medium grid case in this analysis. The attack angles of $C_L = 0.5$ cases are 2.327°, 2.318° and 2.314° for the coarse, medium and fine grids, respectively. The horizontal stabilizer angle is set at 0°.

2.2.2 Equations for Drag Decomposition Method

In this chapter, the drag decomposition method is used to calculate drag without spurious drag. The theory of the drag decomposition is simple, as stated in this section.

2.2.2.1 Basic Formulation

Given an aerodynamic body immersed in a fluid flow described by the RANS equations, the conservation of mass and momentum in the x–direction (parallel to the free stream) requires

$$\nabla (\rho \boldsymbol{u}) = 0, \tag{2.1}$$

$$\nabla (\rho u \boldsymbol{u}) + \frac{\partial P}{\partial x} - \nabla \boldsymbol{\tau_x} = 0. \tag{2.2}$$

By combining Eqs. (2.1) and (2.2), the following equation is obtained [70]:

$$\nabla \left[\rho (u - U_\infty) \boldsymbol{u} + (p - p_\infty) \boldsymbol{i} - \boldsymbol{\tau_x}\right] = 0. \tag{2.3}$$

A control volume V (Fig. 2.2) around the body has a boundary, $\partial V = S_A + S_F + S_D$, where S_A is the closed body surface, S_F is the upstream and lateral outer boundary, and S_D is the downstream outer boundary. According to Gauss' theorem, Eq. (2.3) leads to

$$\iint\limits_{S_A+S_F+S_D} \left[\rho (u - U_\infty) (\boldsymbol{u} \cdot \boldsymbol{n}) + (p - p_\infty) n_x - (\boldsymbol{\tau_x} \cdot \boldsymbol{n})\right] \mathrm{d}S, \tag{2.4}$$

with $\boldsymbol{n}$ being an outward unit normal vector.

V_v is a volume containing the boundary and viscous shear layers and V_w contains the

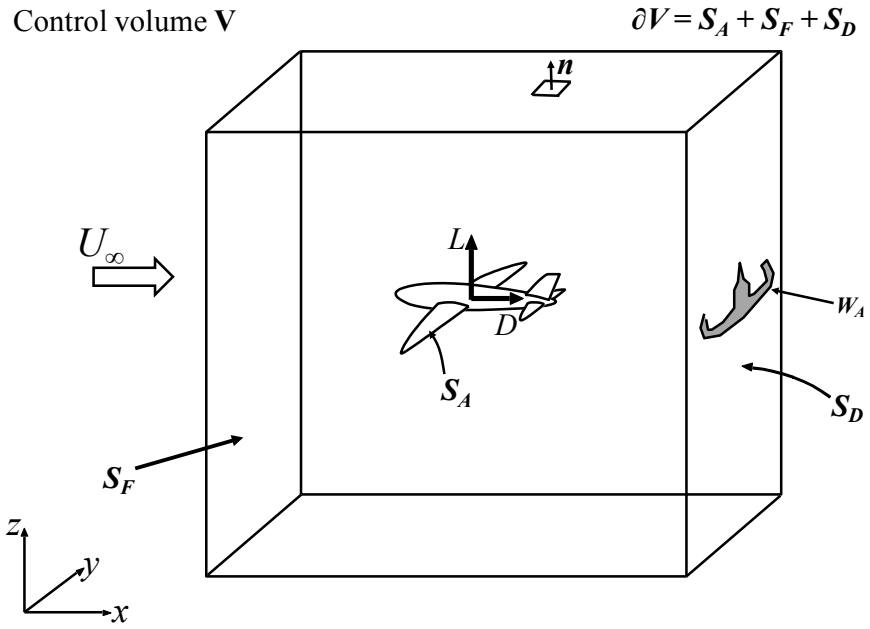

Figure 2.2 Control volume.

shock waves. Given that the flow is truly inviscid outside $V_v + V_w$ and by ignoring the lift-induced drag and its interaction with the other components, only viscous and wave drag are produced. In this case, it is assumed that the condition $\boldsymbol{\tau_x} = 0$ (no perpendicular velocity components exist) holds far downstream at S_D. Thus,

$$D = D_v + D_w = -\iint_{S_D} \rho\,(u - U_\infty)\,(\boldsymbol{u}\cdot\boldsymbol{n})\,\mathrm{d}S, \tag{2.5}$$

where D_v is the viscous drag and D_w is the wave drag. By introducing thermodynamic relations

$$H = \frac{\gamma}{\gamma - 1}\frac{p}{\rho} + \frac{\boldsymbol{u}\cdot\boldsymbol{u}}{2}, \tag{2.6}$$

and the adiabatic relation

$$\frac{p}{p_\infty} = e^{-\frac{\Delta s}{R}}\left(\frac{T}{T_\infty}\right)^{\frac{\gamma}{\gamma-1}}, \tag{2.7}$$

the following expression is obtained [71]:

$$\frac{p}{p_\infty} = e^{-\frac{\Delta s}{R}} \left[1 + \frac{\gamma - 1}{2} M_\infty^2 \left(1 - \frac{u^2 + v^2 + w^2}{U_\infty^2} + 2 \frac{\Delta H}{U_\infty^2} \right) \right]^{\frac{\gamma}{\gamma - 1}}. \tag{2.8}$$

As S_D is placed far downstream, the assumption $p = p_\infty$ and $v = w = 0$ holds. Then, u can be expressed as follows:

$$u = U_\infty \sqrt{1 + 2 \frac{\Delta H}{U_\infty^2} - \frac{2}{(\gamma - 1) M_\infty^2} \left[\left(e^{\frac{\Delta s}{R}} \right)^{\frac{\gamma - 1}{\gamma}} - 1 \right]} \tag{2.9}$$

Thus, the following relation is yielded,

$$u - U_\infty = \Delta u, \tag{2.10}$$

with Δu formulated as

$$\Delta u = U_\infty \sqrt{1 + 2 \frac{\Delta H}{U_\infty^2} - \frac{2}{(\gamma - 1) M_\infty^2} \left[\left(e^{\frac{\Delta s}{R}} \right)^{\frac{\gamma - 1}{\gamma}} - 1 \right]} - U_\infty. \tag{2.11}$$

Next, using Gauss' theorem, Eq. (2.5) leads to

$$D_v + D_w = - \iiint_{V_v + V_w} \nabla \left(\rho \Delta u \boldsymbol{u} \right) \, \mathrm{d}V, \tag{2.12}$$

which expresses the sum of viscous and wave drags. Assuming that the volumes V_v and V_w are not overlapped, Eq. (2.12) reduces to

$$D_v = - \iiint_{V_v} \nabla \left(\rho \Delta u \boldsymbol{u} \right) \, \mathrm{d}V, \quad D_w = - \iiint_{V_w} \nabla \left(\rho \Delta u \boldsymbol{u} \right) \, \mathrm{d}V, \tag{2.13}$$

as shown by Vooren and Destarac [70]. It can also be rewritten as

$$D_v = - \iiint_{V_v} cd \, \mathrm{d}V, \quad D_w = - \iiint_{V_w} cd \, \mathrm{d}V, \tag{2.14}$$

where $cd = \nabla \left(\rho \Delta u \boldsymbol{u} \right)$. Tognaccini [29] expanded Eq. (2.13) by using Taylor's series to the

second order and obtained approximate expressions for the drag. They can be written as

$$D_v = -U_\infty \iiint_{V_v} \nabla\left(\rho g \boldsymbol{u}\right) \,\mathrm{d}V, \quad D_w = -U_\infty \iiint_{V_w} \nabla\left(\rho g \boldsymbol{u}\right) \,\mathrm{d}V, \tag{2.15}$$

where

$$g\left(\frac{\Delta s}{R}, \frac{\Delta H}{U_\infty^2}\right) = f_{s1}\frac{\Delta s}{R} + f_{s2}\left(\frac{\Delta s}{R}\right)^2 + f_{H1}\frac{\Delta H}{U_\infty^2} + f_{H2}\left(\frac{\Delta H}{U_\infty^2}\right)^2,$$

while

$$f_{s1} = -\frac{1}{\gamma M_\infty^2},\ f_{s2} = -\frac{1}{\gamma M_\infty^2},\ f_{H1} = 1, f_{H2} = -\frac{1}{2}.$$

By nondimensionalizing the integrand by the dynamic pressure for entropy and enthalpy, Eq. (2.15) can be written as

$$C_{Dv} = \iiint_{V_v} cd_s \,\mathrm{d}V + \iiint_{V_v} cd_H \,\mathrm{d}V, \quad C_{Dw} = \iiint_{V_w} cd_s \,\mathrm{d}V + \iiint_{V_w} cd_H \,\mathrm{d}V. \tag{2.16}$$

The aforementioned expressions (Eq. (2.13) or (2.15)) realize the volume integrals of the drag components. Hence, given the unique definitions of the viscous (boundary layer and wake) and shock wave drag domains, the domain V can be decomposed as $V = V_v \cup V_w \cup V_{\mathrm{sp}}$. The domains V_v and V_w were previously defined, above and V_{sp} specifies the remaining part of the flow–field in which drag is produced because of numerical diffusion, that is, spurious drag. Thus, the drag components via irreversible phenomena, that is, entropy production can be decomposed into three contributions:

$$D_{\mathrm{irr}} = D_v + D_w + D_{\mathrm{sp}}. \tag{2.17}$$

2.2.2.2 Domain Selection

To decompose drag into its components, the regions to be integrated must be selected as described earlier. The drag integration of cells selected as the wave-drag regions yields a wave drag, and the integration of the cells selected as the boundary layer and wake yields a profile drag. The remaining cells are considered to produce a spurious drag. Then, the following sensors have been used in the drag decomposition, to select the domains. The

cells in which the sensor value is larger than a selected cutoff (=threshold) are chosen as the cells included in the domain.

2.2.2.2.1 Shock Wave Domain The following "shock function" has been used to select the shock wave domain [26]:

$$F_{\text{shock}} = \frac{\boldsymbol{u} \cdot \nabla p}{a|\nabla p|}, \tag{2.18}$$

where a is the local speed of sound.

2.2.2.2.2 Boundary–layer Domain Eddy viscosity has been used as a viscous domain sensor. This works well for fully turbulent flows. The adopted sensor in this chapter is:

$$F_{\text{bl}} = \frac{\mu_l + \mu_t}{\mu_l}, \tag{2.19}$$

where μ_l and μ_t are the molecular (or dynamic) and eddy viscosities, respectively [26]. The sensor F_{bl} is referred to hereafter as the "boundary-layer function". Note that eddy viscosity-based boundary-layer function will not work perfectly in the following cases:

1. Boundary layer is laminar.
2. Spurious turbulence occurs outside the physical boundary layer due to turbulence model or grid.

2.2.2.3 Maskell's Induced Drag

For a 3-D flow, the induced drag cannot be computed using the previous method in Section 2.2.2.1 because the static–pressure–related drag components are ignored. In this dissertation, the method originated by Maskell [61] and improved by Giles *et al.* [72] and Kusunose [62] is used to compute it. The computational space is cut by a plane at a downstream position normal to the free–stream direction, referred to hereafter as the "cut plane". In Fig. 2.2, S_D corresponds to the cut plane.

By assuming that the S_D is placed on the cut plane located far downstream of the airplane and if the entropy and total enthalpy loss can be ignored, the drag calculated at the far boundary can be written as

$$D_i = -\iint_{S_D} \left[\rho\left(u - U_\infty\right)\left(\boldsymbol{u} \cdot \boldsymbol{n}\right) + \left(p - p_\infty\right) n_x\right] \mathrm{d}S. \tag{2.20}$$

The application of a small disturbance theory, results in [26]

$$\frac{u}{U_\infty} \approx 1 - \frac{v^2 + w^2}{U_\infty} \approx 1, \tag{2.21}$$

and without entropy and total enthalpy loss, Eq. (2.8) becomes [72]

$$p - p_\infty \approx -\frac{1}{2}\rho_\infty \left(v^2 + w^2\right). \tag{2.22}$$

Then, the induced drag, Eq. (2.20), is written as

$$D_i = \frac{1}{2}\rho_\infty \iint_{S_D} \left(v^2 + w^2\right) \mathrm{d}S. \tag{2.23}$$

The vorticity and potential of the flow in the plane are respectively computed using the transverse velocity components v and w on the cut plane and are used to obtain the induced drag at the plane's position. A two-dimensional flow is defined in the plane, and Maskell's induced drag is given by [61, 72, 62] rewriting Eq. (2.23) as

$$D_i = \frac{\rho_\infty}{2} \iint_{W_A} \psi \xi dy dz, \tag{2.24}$$

where ψ is a scalar function defined on the cut plane and is the solution of the Poisson equation

$$\frac{\partial^2 \psi}{\partial y^2} + \frac{\partial^2 \psi}{\partial z^2} = -\xi, \tag{2.25}$$

with the boundary condition of

$$\psi = 0, \tag{2.26}$$

at infinity. The subscript W_A (Fig. 2.2) represents the wake domain on the cut plane, and ξ is vorticity defined on the cut plane. In the downstream flow of a body, the vorticity should be almost zero, except within the wake domain. This is true for actual flow fields, such as in a wind tunnel. However, for CFD flow fields, vortical domain is easily spread, and it is difficult to confine effective domains [73]. There is a risk to include artificial viscosity related to vorticity by considering a larger area than the wake region. However, a satisfactory method to confine vortical domain has not been determined yet. Thus, in this study, almost the entire cut plane, excluding the outer edge of the domain, is integrated to calculate induced drag.

To acquire the total drag, the viscous, wave, and induced drags must be summed up. The volume of viscous and wave drags is integrated using the cells confined to the upstream of the cut plane to compute induced drag. The sum of the volume integral drag and the induced drag then gives the total drag. The difference between the total drag calculated by the drag decomposition method and the conventional surface integral should give the spurious drag.

2.2.3 Drag Decomposition Analysis

As described in Section 1.2.1, the drag decomposition method divides the computational domain into domains producing the profile, wave, and spurious drags. The profile and wave drag domains are selected as domains in which Eqs. (2.18) and (2.19) are larger than appropriate values, respectively. However, in practical drag decomposition analysis, the sensors used for detecting those domains do not function perfectly, and the procedure requires some techniques to select proper domains [2]. In this section, the procedure including such techniques is explained. Notably, the selection of appropriate domains is the most time consuming part of the drag decomposition analysis, and a part of the problem is solved in Chapter 3.

Ueno and Tognaccini [2] reported issues to be solved for domain selection and demonstrated a practical example of the existence of such issues by using CFD results around the NACA0012 airfoil at the free-stream Mach number of 0.7. They are related to spatial oscillations of integrand for drag calculation around the selected domains. In this section, a practical procedure of the drag decomposition method is explained along with results, and is applied to the CFD results of the NASA CRM. The complete procedure to perform drag decomposition for CFD with a practical shape has not been published for practical computations.

2.2.3.1 Removal of Outer Boundary of Computational Domain

First, it is found that the entropy oscillates spatially around the outer boundary of the computational domain (it is hereafter called as "entropy oscillation"), and it should be considered before dividing the computational domain into profile and wave drag domains. The cells adjacent to the outer boundary of the computational domain include entropy oscillation when constant boundary conditions are applied on the computation because of the flow field produced by the target body immersed in the fluid. Fig. 2.3 illustrates the entropy

drag integrand times cell volume ($cd_s \times \mathrm{d}V$ in Eq. 2.16) in a computational domain around the NACA0012 airfoil at an attack angle of 3° [2]. The length scales are nondimensionalized by the chord length of the airfoil and $cd_s \times \mathrm{d}V$ is, therefore, nondimensional value. This indicates that the integrand oscillates around the outer boundary of the computational domain because of the presence of entropy spatial oscillation there. The oscillation is only spatial oscillation and is not time dependent. It should be removed from the domain to be integrated for wave and profile drag calculation before analyzing the drag decomposition.

In the cases of the CRM in this chapter, the removal of only a single layer of cells from the outer boundary is sufficient because the difference by increasing second margin layer is less than 0.2 drag counts.

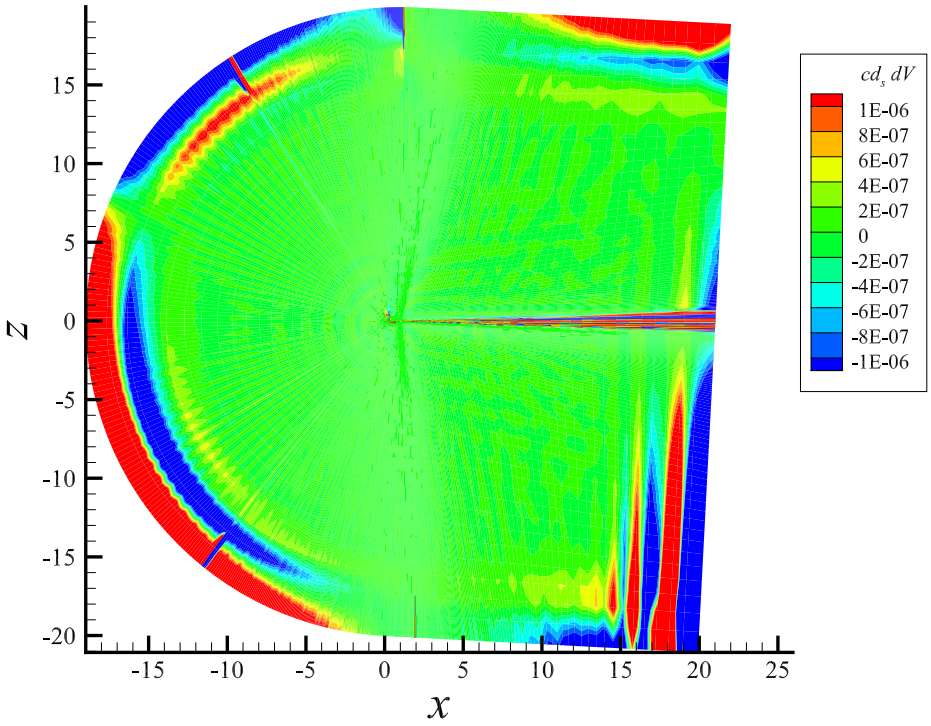

Figure 2.3 Drag integrand $cd_s dV$ around outer boundary of computational domain of the NACA 0012 airfoil at an attack angle of 3° [2]. (The length scales are nondimensionalized by the chord length.)

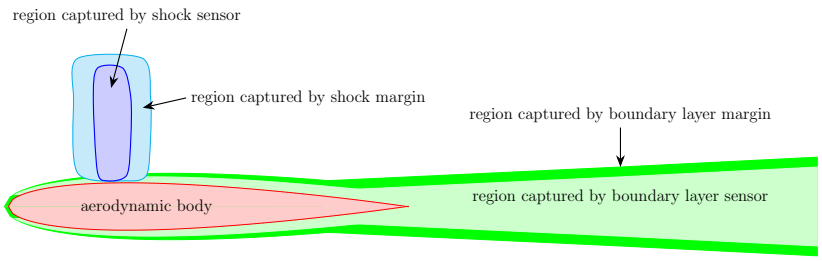

Figure 2.4 Domain selected by shock function, boundary-layer function, shock margin, boundary-layer margin.

2.2.3.2 Domain Selection for Wave and Profile Drags

After removing the entropy oscillation around the outer boundary, the domain is divided into the wave, profile, and spurious drag domains. In this procedure, the wave drag domain is selected first.

2.2.3.2.1 Cutoff Value Determination As described in Section 2.2.2.2, the shock function (Eq. (2.18)) and the boundary-layer function (Eq. (2.19)) are used as sensors to select the cells to be integrated for wave and profile drags, respectively. Specifically, cells are selected if the value of the sensors in those cells exceeds the cutoff (=threshold) value [26]. Actually, those sensors sometimes miss capturing the entire region of the wave and profile drag domain because of spatial oscillations accompanied with the shock waves and the boundary-layer edge. To cover those domains, the selected domain is geometrically extended. The extensions are called as "margins" in this dissertation. The details of the margin setting procedures are described in Section 2.2.3.2.2 and 2.2.3.2.3. Fig. 2.4 shows the domain selection around an aerodynamic body. To determine appropriate sensor cutoff values, numerous drag-decomposition calculations were conducted with varying values of sensors. After selecting appropriate cutoff values for each sensor by using the procedure stated subsequently in this section, the same values can generally be used for similar simulation results acquired using the same solver even if a different grid is used.

At the root of the shock wave, the shock wave interferes with the boundary layer. Therefore, the domains detected by the shock and boundary-layer functions overlap. A strict

decomposition of wave and profile drags in such an interfering area is difficult because the method employed in this dissertation decomposes the drag components by domain division. To determine the quantity of drag components, the type of the interfering domain should be determined. In other words, the quantities of decomposed drags depend on determination technique of the domain division. In this analysis, the shock function is prioritized over the boundary-layer function in such an overlapping area, that is, it is determined as the wave drag domain. In such a case, when a value is set for the boundary-layer function and the shock function cutoff is increased from very low values, the profile drag domain interchanges with the wave drag domain, and the number of cells selected as the boundary layer (contributing to profile drag) increases. As the shock function value is proportional to the local Mach number, the lower shock cutoff value leads to the selection of a greater number of cells. An example of drag-decomposition calculations for cutoff value determination is shown in Fig. 2.5(a). By increasing the shock function cutoff value above the free-stream Mach number, the interchange between the wave and profile drags' cells is stopped, and the value at which this occurs first should be a good number for selecting as a shock function cutoff value because the overlap between wave and profile drag domains is minimum. When the shock cutoff value F_{shock} is small and the overlap exists, the main part of the profile drag domain is invaded by the wave drag domain. In constrast, when the F_{shock} is extremely large and the wave drag domain is small, the main part of the wave drag domain cannot be captured adequately. Therefore, the F_{shock} that realizes the minimum overlap is chosen to capture as maximum a wave drag domain as possible. In this analysis, $F_{\text{shock}} = 0.92$.

It should be noted again that the profile-drag and wave-drag domains are usually overlapped around the foot of the shock wave. Thus, strict separation is impossible while the decomposition is depending on the spatial domain division. That is the limit of the present drag decomposition method and more sophisticated method to achieve strict decomposition is anticipated.

Similar to the shock cutoff, the boundary-layer function requires a cutoff value; therefore, numerous drag-decomposition calculations must be also conducted to determine an appropriate cutoff value. An example of such calculations for profile drag domain detection is shown in Fig. 2.5(b); a logarithmic scale is used for the abscissa because the boundary-layer function cutoff value varies over a wide range. When a very low value is set, almost the entire domain will be selected as the profile drag domain. An increase in the value typically brings a discrete change in the drag coefficient, and it is appearing at around

$F_{\mathrm{bl}} - 1.0 = 0.1$ in Fig. 2.5(b). It is empirically known that the selected domain is almost entirely a computational domain when $F_{\mathrm{bl}} - 1.0$ is less than the previously referred discrete change and suddenly changes only to the boundary layer and wake when the cutoff of F_{bl} is larger. When $F_{\mathrm{bl}} - 1.0$ is larger than 0.1, the selected domain decreases while F_{bl} increases. A plateau of the drag value exists at $0.1 < F_{\mathrm{bl}} - 1.0 < 10$ and it corresponds to the cutoff value region where the proper profile drag domain is captured. Then, any value of F_{bl} at the plateau can be chosen, and the drag variation due to F_{bl} selection on the plateau is compensated by the boundary-layer margin, as shown in Section 2.2.3.2.2. Increasing the cutoff value further eventually results in no cells being selected. The value can be chosen almost anywhere between the discrete change above 0.1 to the point around 10.0, at which the captured boundary-layer cells begin to gradually decrease. For this analysis, $F_{\mathrm{bl}} = 4.0$ is chosen because the captured drag value is at the local maximum. This local maximum appears because the drag integrand cd_s variates at the edge of the boundary layer. The reason for choosing the local maximum is explained subsequently by using Fig. 2.10 in Section 2.2.3.2.2.

Appropriate values are chosen for this analysis by these processes. Practically, visual inspection of selected cells is recommended to confirm that the chosen values select appropriate wave and profile drag cells.

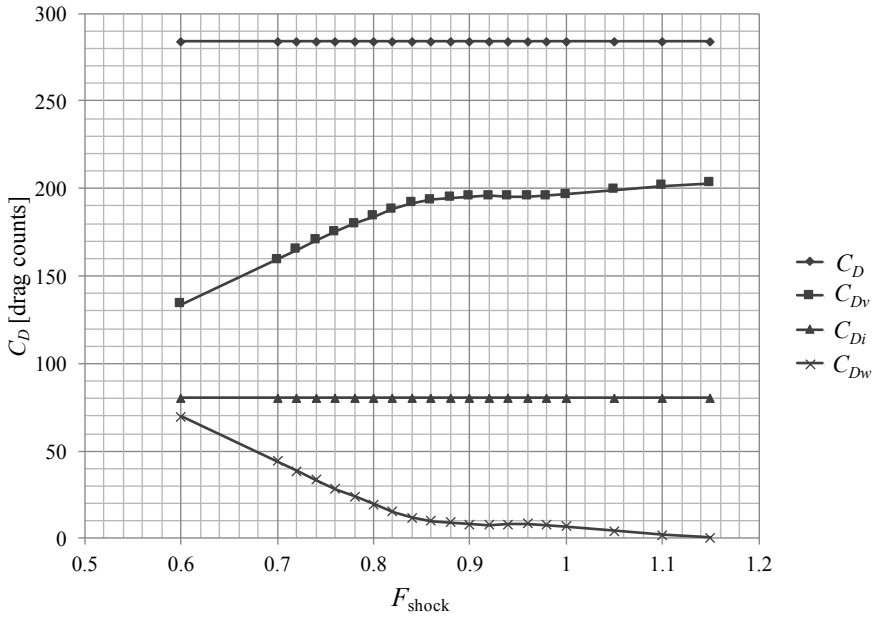

(a) Drag values variation due to shock function value.

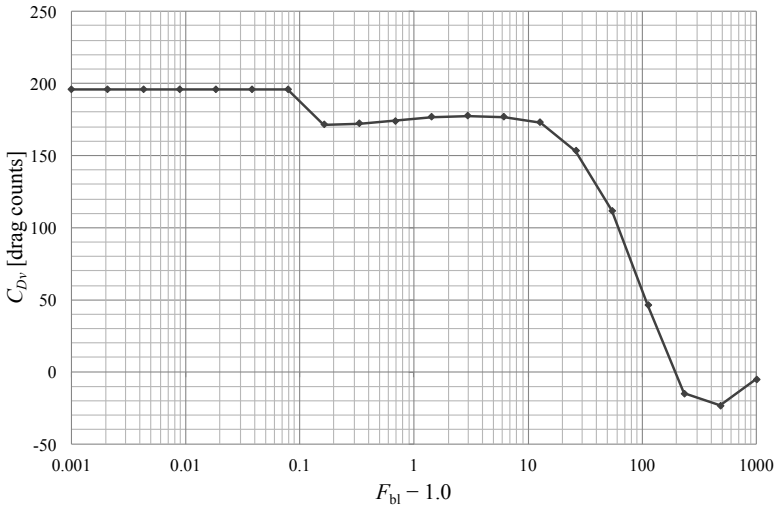

(b) Profile drag variation due to boundary-layer function value.

Figure 2.5 Computed drag versus cutoff value variations of shock and boundary-layer functions (coarse grid case).

2.2.3.2.2 Marginal Domain of Shock and Boundary Layer The domain selected by the shock function is not sufficient because the drag integrand cd_s in Eq. (2.15) accompanied with the shock wave spatially oscillates around it. Fig. 2.6 illustrates the phenomenon described by Ueno and Tognaccini [2]. This figure shows variations of Mach number, shock function, and entropy drag integrand times cell volume ($cd_s \times \mathrm{d}V$) on a line normal to a shock wave, occurring on the surface of the NACA0012 airfoil in the same flow field of Fig. 2.3. The green, pink, and blue lines correspond to the Mach number, shock function, and $cd_s \times \mathrm{d}V$, respectively. The abscissa represent the coordinate, which initiates from the nose of the airfoil and is aligned to the free stream; $X = 1.0$ at the trailing edge when the attack angle is 0.0°. Fig. 2.6 illustrates the case of $\alpha = 3.0°$.

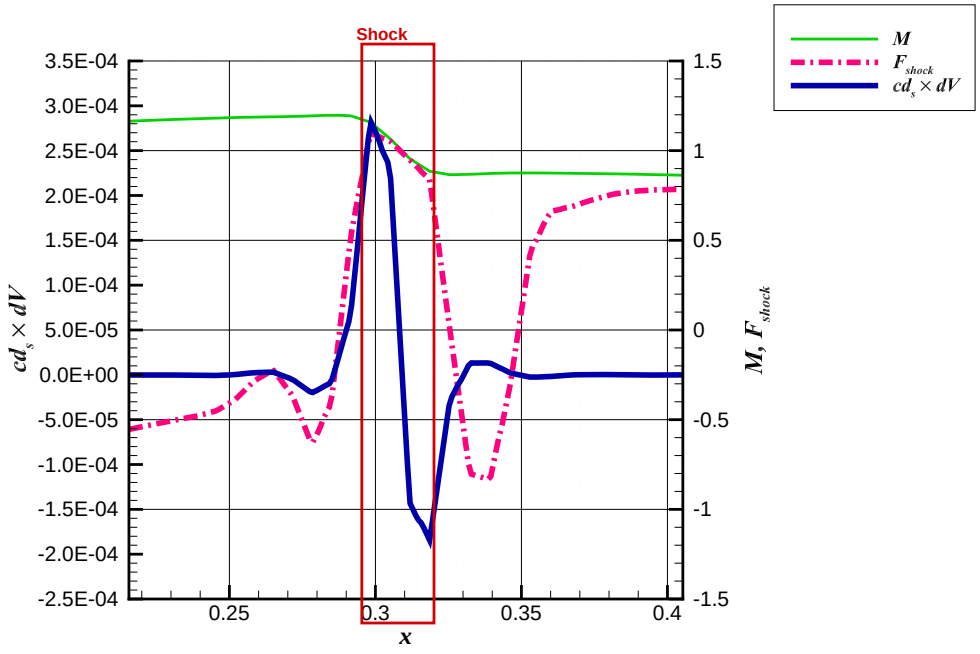

Figure 2.6 Drag production around a shock wave [2]. (Labels and legends are superimposed to fit with Nomenclature of this dissertation.)

In this example, the domain in which the shock function value is higher than 0.87 is selected as the wave drag domain because the Mach number slows down from supersonic to subsonic in that domain. A red rectangle surrounding the wave drag domain is superimposed on the original figure by the author of this dissertation. Although the shock function successfully captured the slowing down domain, the $cd_s \times \mathrm{d}V$ oscillates outside the domain.

A technique to select such domains is necessary because such an oscillation is due to the existence of the shock wave, although it can originates from numerical characteristics of the employed scheme in the simulation. The employment of a lower value for F_{shock} to cover the domain is not appropriate because the domain downstream not related to wave drag production would be selected by such values. An example of such a domain is shown in Fig. 2.6. Although the shock function value is high in the domain, its local Mach number is constantly less than 1.0 and the wave drag does not appear in such a condition.

In addition for the CRM computations, the shock function F_{shock} cannot capture all the spatial oscillations found around the shock. In Fig. 2.7(a) shows the cells captured by the shock function at a normalized span-wise subsection $\eta = 0.5$. The green and gray colors represent cells selected by the shock and boundary-layer functions, respectively, and the other domain comprises the cells that might produce entropy drag but were not captured by either of the functions. The colormap shows the amount of entropy drag integrand cd_s. Around the wave drag cells, pieces of wave drag production failed to be counted. To include those cells, a margin extension of the domains selected by the sensors should be performed.

The missed wave drag is considered to be oscillations attributed to the errors due to representing the discontinuity—the shock wave—by a second order scheme. It is impractical to determine theoretically how far the oscillations reach especially for 2- or higher dimensional computations. In this dissertation, a geometrical margin extension was employed. Fig. 2.8 depicts the strategy used to build the margin extension. The method is simple: a single layer of cells adjacent to the selected domain cells using the shock function (Eq. 2.18) is selected as the domain extension, and the process is repeated such that extension cells are stacked around the selected domain layer by layer. With five margin layers, the wave drag fractions that were originally missed are considered to be included in the integration cells for wave drag in the analysis (Fig. 2.9(a)). In this case, the shock waves over the wings are assumed to be isolated; they are not severely interfered by other shock waves and the space around it does not include shocks. In such cases, geometrical margin extension functions effectively; the drag finally does not change with margin extensions. In addition, because the computational grids used in the computation in this study are built in a structured manner, and the grid density variation is attained without changing grid topology; the oscillation characteristics around the shock can be expected to be dependent only on the scheme characteristics. Thus, common margin layers can be used for all the cases of this study. In Fig. 2.9(a), the drag changes are less than 0.1 drag counts for the

fine and medium grids when the shock margins layers range from 5 to 10, whereas they are larger than 0.4 drag counts for the coarse grid. As the variations less than 0.1 drag counts are practically ignorable variations and the shock wave over the CRM main wings mostly follows the previous isolation assumption, the five layers are judged to be sufficient in this analysis.

While five layers perhaps seem excessive, extending the margin into the main flow domain is usually harmless because the shock wave above the main wings of the transonic transport is generally isolated in the main flow in which no entropy is basically produced.

A phenomenon similar to that of the wave drag appears for the profile drag at the outer edge of the boundary layer, as noticed by Petrosino [74]. Fig. 2.10 shows an example by Ueno and Tognaccini [2]. The figure shows variations of the boundary-layer function (Eq. (2.19)) and drag production normal to the airfoil surface of the same computation for Fig. 2.6. In the figure, the blue and pink lines represent the boundary-layer function F_{bl} and drag integrand times cell volume $cd_s \times \mathrm{d}V$, respectively. The ordinate of the graph starts from the airfoil surface, and the figure is drawn at $X = 0.336$ for $\alpha = 2.0°$. The figure shows that the drag production variates at the ordinate of 0.055 and the larger boundary-layer function cannot capture all the variation. As explained in Section 2.2.3.2.1 using Fig. 2.5(b), the boundary-layer cutoff value prompting the local maximum of drag is chosen in this analysis. When the cutoff value increases, the drag takes positive values, and then acquires a negative peak around $z = 0.056$ in Fig. 2.10. This indicates that the integrated drag acquire a local maximum when the drag curve crosses 0.0 at approximately $z = 0.054$. The oscillation at the edge of the boundary layer should be captured using the boundary-layer margins.

In addition, for the CRM, the boundary-layer marginal domain must be captured. Fig. 2.11(a) shows entropy drag integrand cd_s around the airfoil cut at the wing subsection of $\eta = 0.5$. The green cells represent wave drag cells and the gray cells are cells selected by the boundary-layer function. It is obvious particularly in the aft-domain and wake that the boundary-layer function does not capture all the effects caused by boundary-layer entropy production (Fig. 2.11). By employing the same method to grow the margin around the boundary layer, the gray domain is additionally selected and those cells are sufficient to include almost all of the entropy production due to the boundary layer (Fig. 2.11(b)). Four layers are chosen from the medium and fine grid results because the spatial oscillation due to margin growth almost stops with four layers of boundary-layer margin (Fig. 2.9(b)). Although it is difficult to determine the best number of layers for a coarse grid, the same

number of layers were used because the type of spatial oscillation characteristics depends on the numerical scheme, and the same scheme is consistently used in these flow solutions. This boundary-layer margin effect is significant as seen in Fig. 2.9(b). Therefore, a better boundary-layer detection method is required.

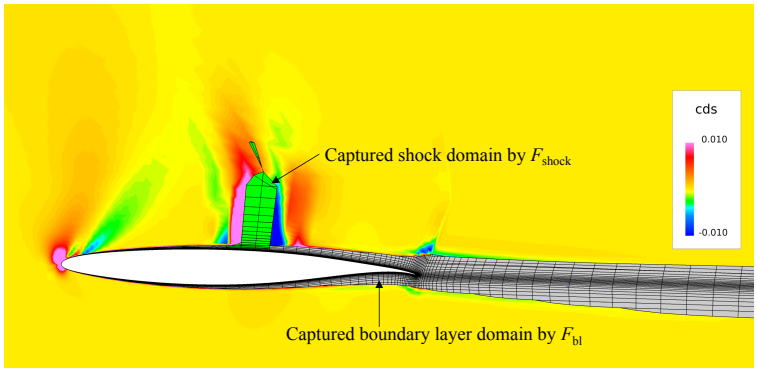

(a) Only with shock function.

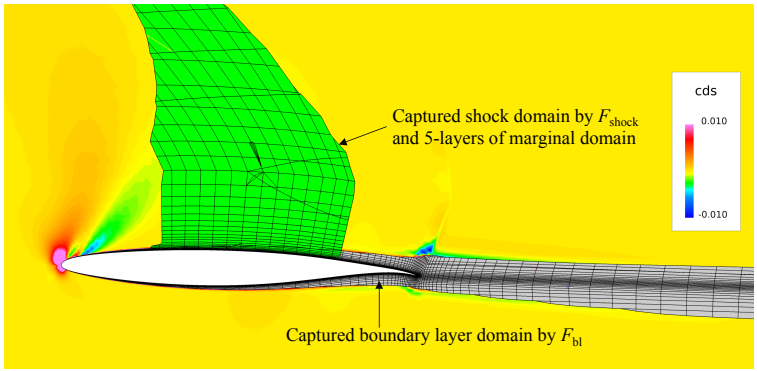

(b) With 5-layers of margin.

Figure 2.7 Selected domain obtained using shock function and margin effect over entropy drag integrand contour (coarse grid, $\eta = 0.5$, white mask: geometry, green cells: wave drag cells, gray cells: profile drag cells, colormap: drag production).

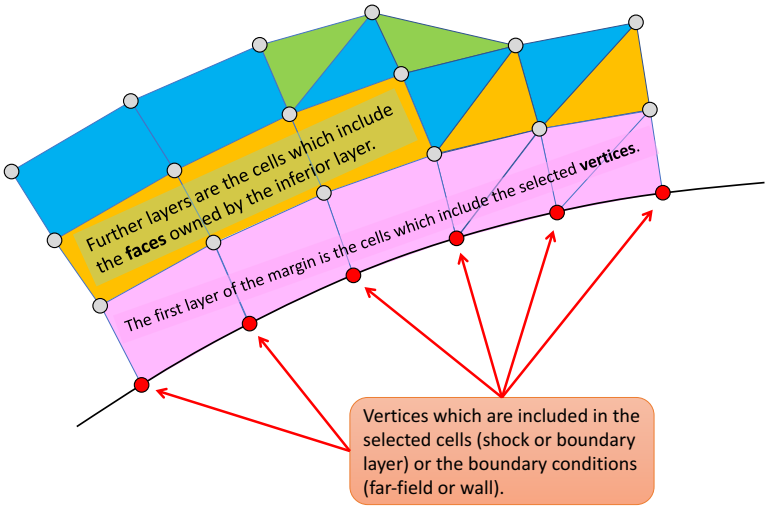

Figure 2.8 Margin layer building strategy (pink cells: first layer, orange cells: second layer, sky blue cells: third layer, green cells: fourth layer).

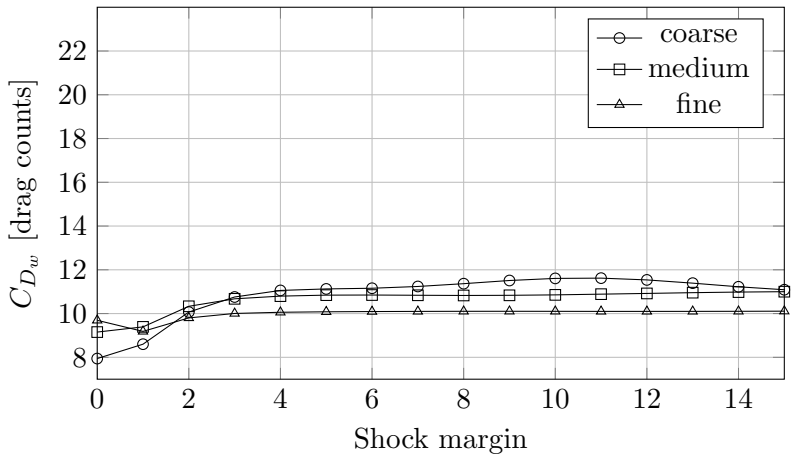

(a) Wave drag coefficient variation due to shock margin increase.

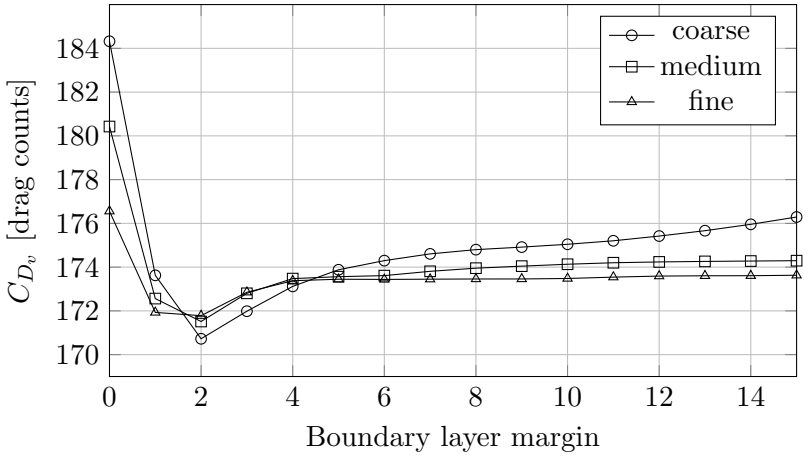

(b) Profile drag coefficient variation due to boundary-layer margin increase. (Shock and wall margins are already set.)

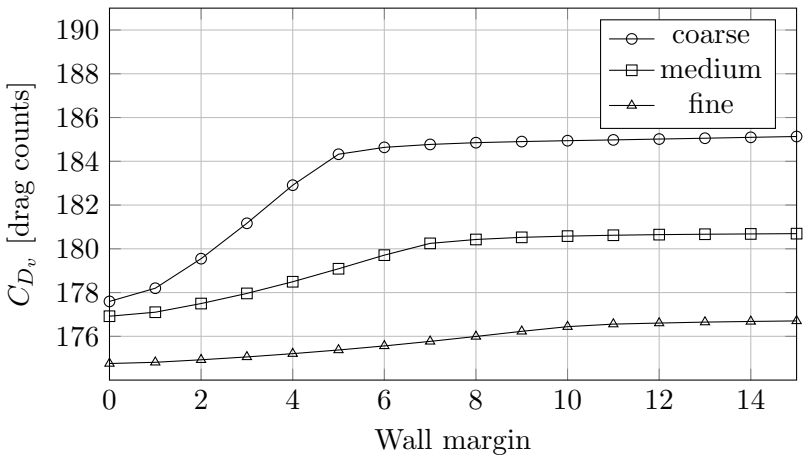

(c) Profile drag coefficient variation due to wall margin increase. (Shock margins are already set.)

Figure 2.9 Drag variations due to numbers of layers of marginal domains.

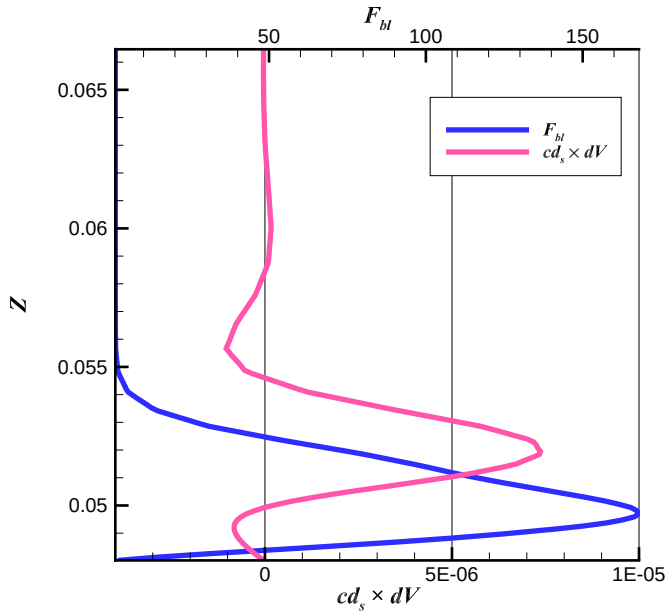

Figure 2.10 Drag production at the edge of the boundary layer [2]. (This figure is reproduced from data of [2].)

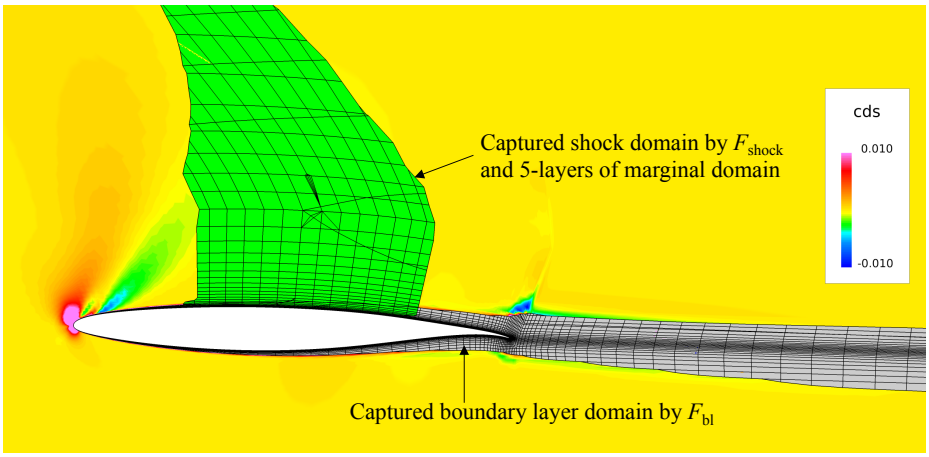

(a) Only with boundary-layer function.

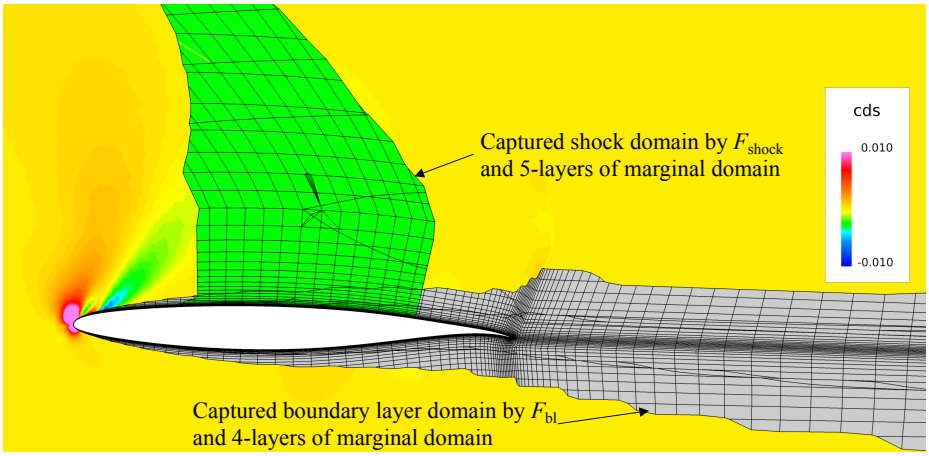

(b) With 4-layers of margin.

Figure 2.11 Domain selection by using boundary-layer function and margin effect (coarse grid, $\eta = 0.5$, white mask: geometry, green cells: wave drag cells, gray cells: profile drag cells, and colormap: drag production).

2.2.3.2.3 Wall Margin Eddy viscosity is very low in the domain adjacent to the model surface. For example, the Cebeci–Smith model [75] is a two-layer model, and the kinematic eddy viscosity ν_{T_i} has the following order of $\nu_{T_i} \approx \kappa\nu y^+$ in the lower layer of the boundary layer where κ is the Kármán constant and ν is the kinematic molecular viscosity [76]. Thus, the eddy viscosity close to the model wall is small. Consequently, cells very close to the model wall could not be captured as the profile drag domains by the cutoff value. To include such cells, margins growing from the model wall were used. When the outer edge of the wall margin reaches the lower edge of the cells selected by the boundary-layer function, the drag variation due to margin growth should become almost flat. Variations of profile drag due to the number of wall margin layers are depicted in Fig. 2.9(c). In this analysis, 5, 8, and 11 layers of wall margins were used for the coarse, medium, and fine grids, respectively. Practically, the wall margin should be applied before the boundary-layer margin, which should be used only to detect the spatial entropy oscillation around the boundary-layer edge.

2.2.3.3 Induced Drag

After determining the cutoff values and margins, volumes of the wave and profile drags can be integrated and induced drag is calculated simultaneously. In the present study, Maskell's method [61] improved by Giles *et al.* [72] and Kusunose [62] is employed to compute the induced drag, as described in Section 2.2.2.3. This method requires a 2-D flow-field on a plane perpendicular to the free-stream direction, and is placed behind the model body without intersecting the model. This 2-D flow-field is obtained through flow-field interpolation. To obtain the proper induced drag by using Maskell's method, the domain close to the outer boundary of the flow field should be removed from the flow-field data for the same reason for which the outer boundary margin should be removed from the control volume as explained in Section 2.2.3.1. In this dissertation, the plane for the induced drag calculation is called as "cut plane." The flow field downstream the cut plane is truncated from the control volume for the volume integral of entropy drag.

The total drag must be constant regardless of the control volume provided that it is enclosing the entire profile and wave drag domains. In addition, the induced drag D_i, which the moving airplane applies to rotate the surrounding air around the trailing vortices at the rate of $D_i U_\infty$ in its wake with the crossflow [72], diffuses to the profile drag because of (mainly numerical) dissipation while the cut plane moves downstream and the control

volume grows [77, 30, 78]. In this analysis, the cut planes are placed varying the position along the flow direction x to examine the influence of the cut plane position. The x-coordinate is normalized by the model's mean aerodynamic chord, which is the reference length for this computation, and the cut plane does not intersect the model downstream from the normalized scale of approximately 10. The x-coordinate image of the CRM is depicted in Fig. 2.12. Then, Fig. 2.13 shows plots of induced drag output versus cut plane position.

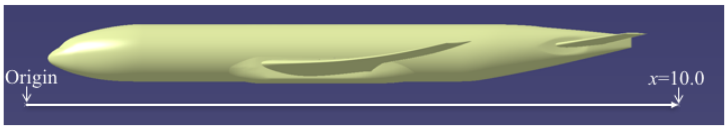

Figure 2.12 x-coordinate of the CRM.

The total drag, involving profile, wave (shock), and induced drags, is almost constant, and an interchange between profile and induced drags is observed at all the grid resolution levels.

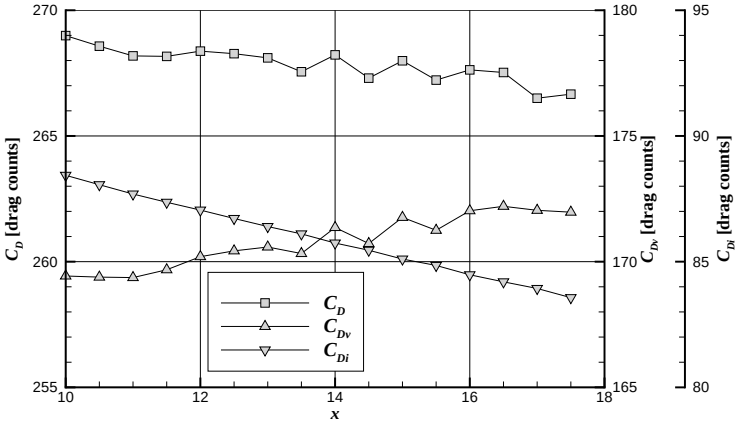

(a) Coarse grid.

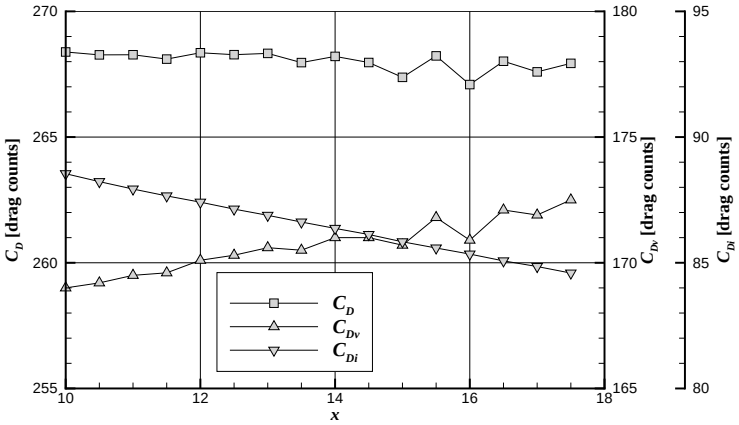

(b) Medium grid.

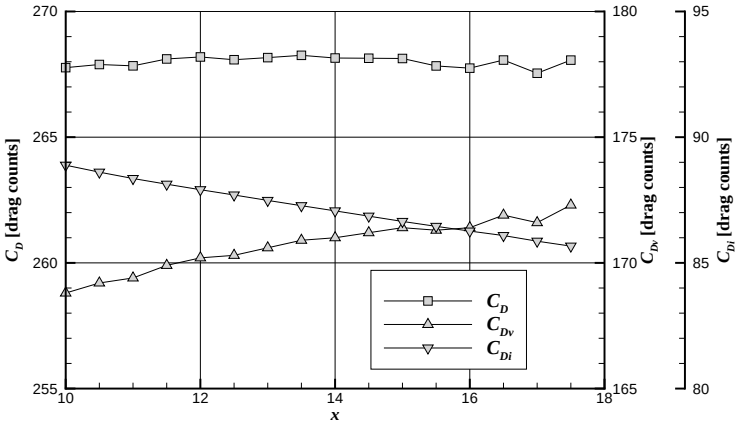

(c) Fine grid.

Figure 2.13 Drag variation versus cut plane location along flow direction x.

2.3 Results and Discussion

2.3.1 Grid Convergence for the Design Point

Fig. 2.14 shows the grid convergence characteristics obtained from the surface integral and the drag decomposition analysis. The total drags are plotted against $N^{-2/3}$, where N is the total number of grid points. The $N^{-2/3}$ is based on the second-order accuracy of the numerical method in 3-D computation. The drag value at $N^{-2/3} = 0$ is the estimated drag with the infinitesimal grid. It was extrapolated using the Richardson extrapolation method [53]. In the figure, the drag acquired using the drag decomposition method and

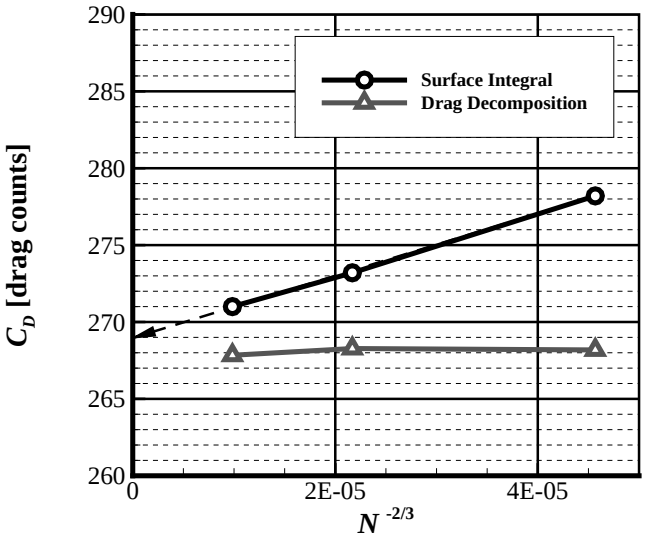

Figure 2.14 Surface integral and drag decomposition ($x = 11.0$) grid convergence.

computed using the computational field cut by the cut plane located at $x = 11.0$ is employed.

The resultant drag is almost constant so that spurious drag seems to be successfully removed from the surface integral, and the drag values calculated using the drag decomposition method for each grid resolution level (the coarse, medium, and fine) agree within almost 1 drag count (Fig 2.14). As this is less than the repeatability error of the JAXA 2 m $\times$ 2 m transonic wind tunnel ($\Delta C_D = 1.5$ drag counts) [79], it is recognized as enough precision in this dissertation. Generally, the repeatability error of wind tunnels is 1–2 drag counts, as stated in Section 2.3.3. This is fairly close to the value extrapolated to zero mesh size in the surface integral convergence study.

Fig. 2.15 shows the grid convergence characteristics of decomposed drag components.

The figure shows that the small inconsistency of the total drag of the fine grid is mainly due to the underestimated wave drag (Fig. 2.15). However, as described in Section 2.2.3, the cutoff values and margin levels are the factors of arbitrariness of the drag decomposition method. Thus, it is difficult to pursue the cause of this level of small inconsistency.

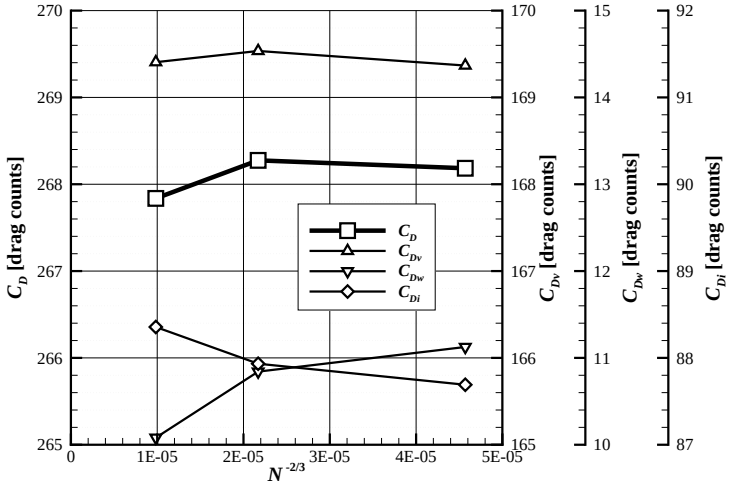

Figure 2.15 Grid convergence characteristics at $C_L = 0.5$.

Even with the coarse grid in this study (2.8×10^6 cells), almost the same value of the estimated converged drag of the grid convergence study is successfully calculated when the drag decomposition method is applied. The difference is within 1.5 drag counts and is sufficiently precise for CFD drag estimation. Thus, attempting drag decomposition study before massive computation could be expected to provide a good insight for cell numbers to be used for a CFD test campaign with a considerable number of computations, such as the optimization process. However, this does not imply that the grid density could be reduced as much as possible even though the drag decomposition method can remove spurious drag. If there are insufficient number of cells that causes the loss of the flow structure which should be reproduced, even the drag decomposition method will not be able to extract the estimated converged value. Therefore, it is important to perform grid convergence study accompanying drag decomposition study to estimate an appropriate cell number to use before massive computations.

2.3.2 Spurious Drag Production

The results of the grid convergence study using the drag decomposition method show that the drag decomposition analysis can remove spurious drag. Fig. 2.16 visualizes the production of local spurious drag. In the figure, the gray and green cells represent boundary layer and wave drag cells, respectively. In addition, the red portions represent the constant surface of entropy drag production ($cd_s = 0.01$) protruding from the boundary layer and wave drag cells. These drag productions correspond to the spurious drag. It is apparent that spurious drag production occurs around the leading edges of the wing, horizontal tail, and nose area of the body.

To examine spurious drag production in detail, the contour images of entropy drag integrand around the wing at a normalized span-wise subsection $\eta = 0.5$ of the CRM are shown in Fig. 2.17 for all the levels of grid density. The figures show the entropy drag productions within the boundary layer and due to the shock on the upper surface of the wing. The color map is deliberately exaggerated to show the drag production more clearly. Fig. 2.18 shows the same images masked with the wave drag cells (green mask) and boundary-layer cells (gray mask) captured using the shock function (Eq. (2.18)) and boundary-layer function (Eq. (2.19)), respectively. A lump of spurious drag production is observed around the leading edge of the wing, and the strength of the spurious drag decreases with increasing grid resolution. Additionally, pressure wave-like drag production emitted from the leading edge to the upper flow field is observed. This represents spurious drag because it decays with increasing grid refinement. For the coarse grid, this pressure wave-like drag production almost reaches the wave drag cells (Fig. 2.18(a)). In the case of a coarser grid, it might affect the shock and contaminate the wave drag integration. Therefore, for the computation regarding NASA CRM in this study, grid density lesser than that of the coarse grid is inappropriate

Around the leading edge of the super-critical wing, the air flow is strongly accelerated, and the velocity gradient from the no-slip wing wall to the accelerated flow and the flow curvature are also very strong. Those strong velocity gradients lead to numerical errors, which in tern cause spurious drag. Even if the density of computational cells around this area is increased, spurious drag will always occur around the leading edge because of excessive entropy production in each cell.

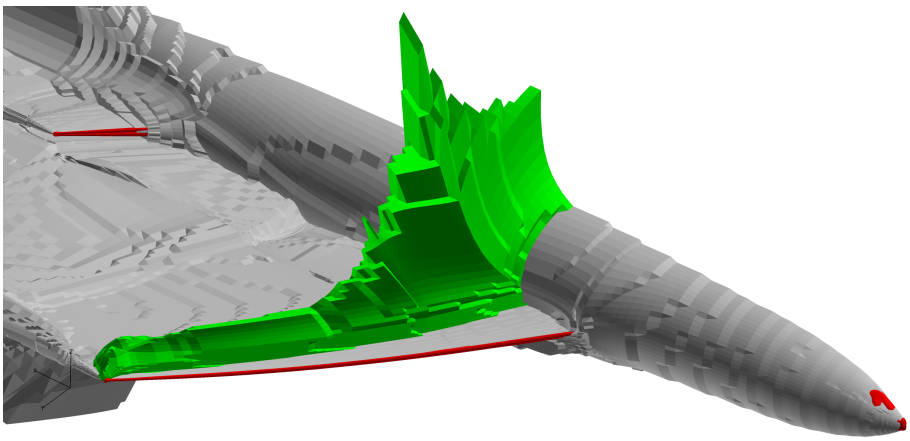

(a) Coarse grid ($\alpha = 2.327°$).

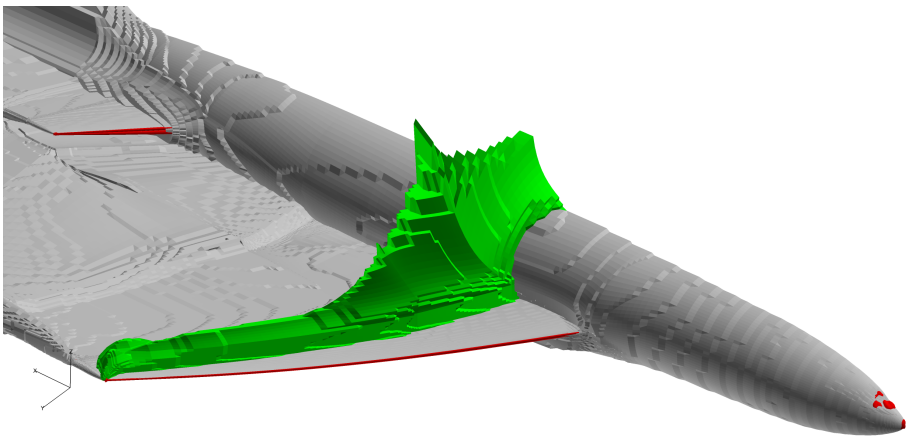

(b) Medium grid ($\alpha = 2.318°$).

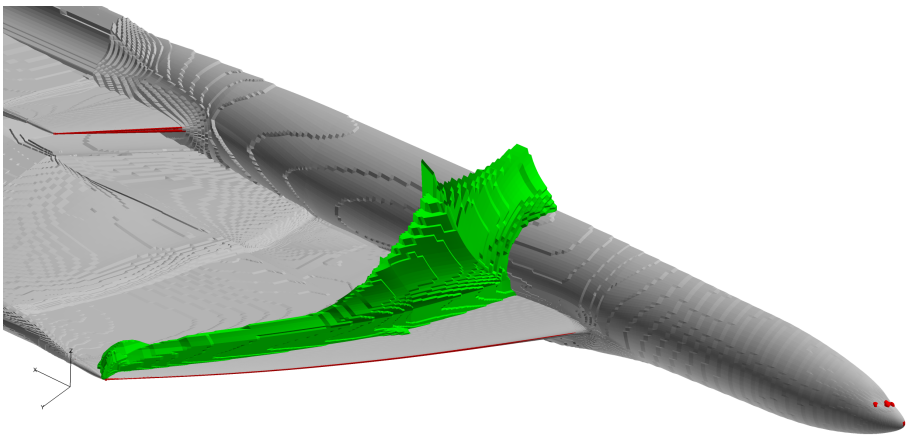

(c) Fine grid ($\alpha = 2.314°$).

Figure 2.16 Selected cells for profile drag (gray cells) and wave drag (green cells), and the protrusion of entropy drag integrand contour (red: $cd_s = 0.01$) from those cells at $C_L = 0.5$.

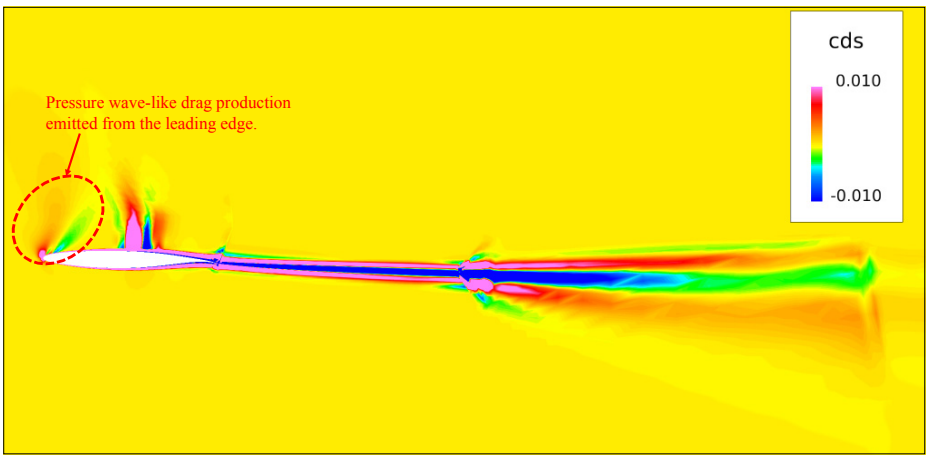

(a) Coarse.

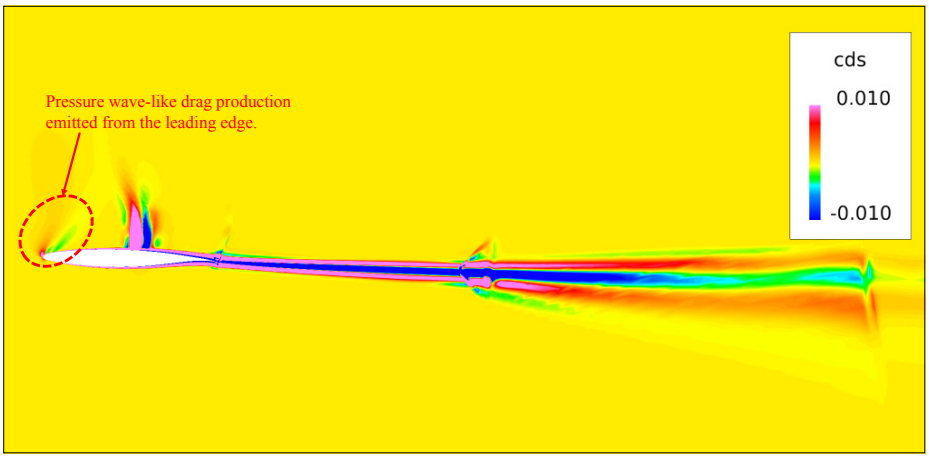

(b) Medium.

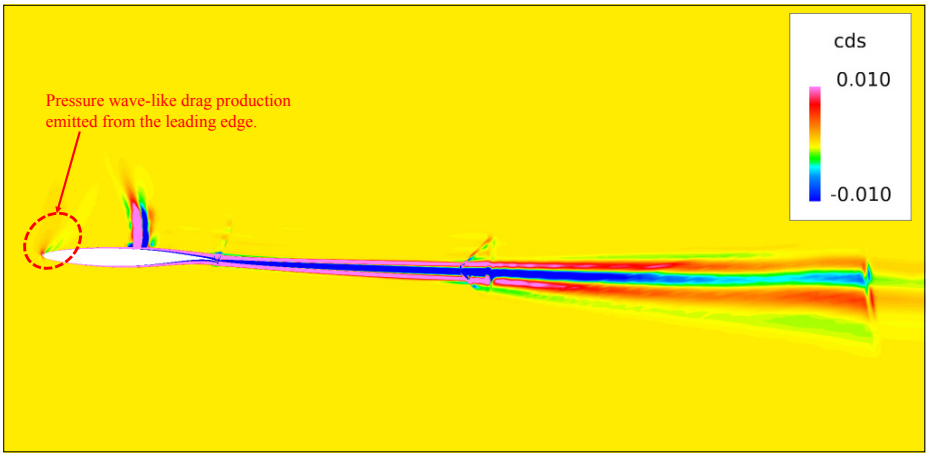

(c) Fine.

Figure 2.17 Entropy drag production contour around the airfoil at $\eta = 0.5$ with various grid resolution levels at $C_L = 0.5$ (white mask is the geometry).

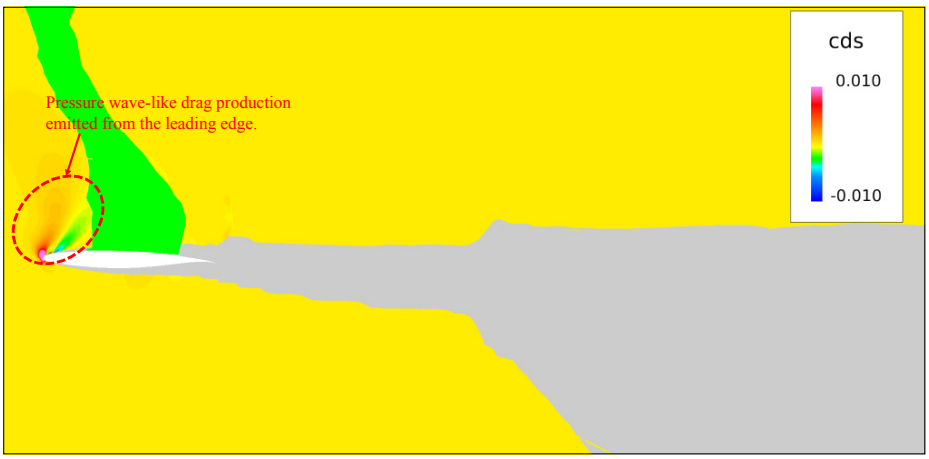

(a) Coarse.

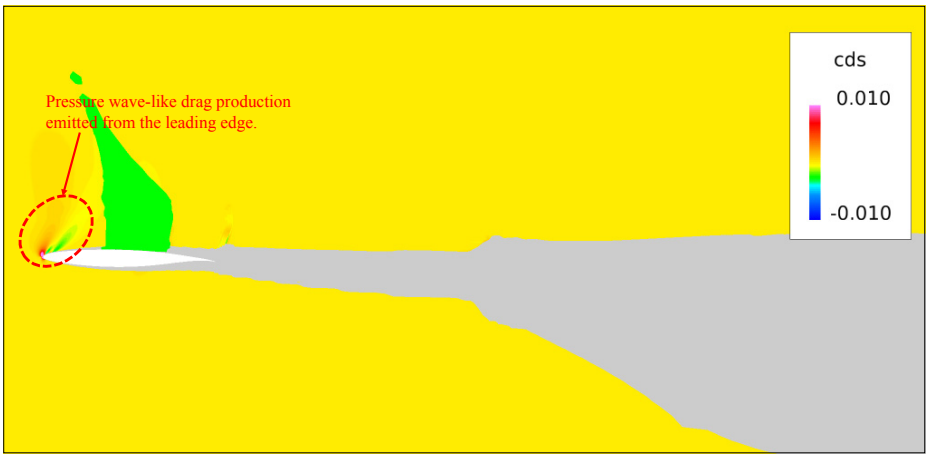

(b) Medium.

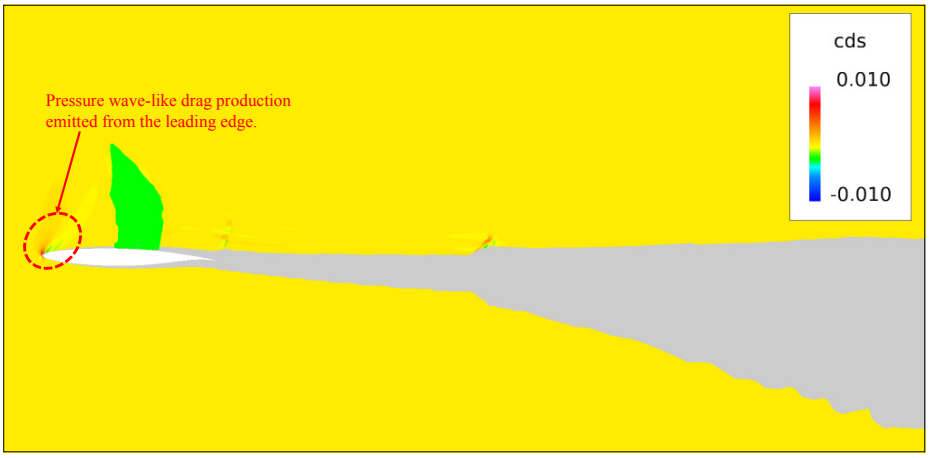

(c) Fine.

Figure 2.18 Spurious drag production contour around the airfoil at $\eta = 0.5$ with various grid resolution levels at $C_L = 0.5$ (white mask: geometry, green mask: wave drag cells, and gray mask: boundary-layer cells).

2.3.3 Uncertainties of Drag Decomposition

Eventually, the drag decomposition analysis consists of the following procedures:

1. Removal of cells adjacent to the outer boundary of the computational space by using an "outer boundary margin" as explained in Section 2.2.3.1
2. Wave drag domain selection by using the shock function F_{shock} in Eq. (2.18) as explained in Section 2.2.3.2.1
3. Profile drag domain selection by using the boundary-layer function F_{bl} in Eq. (2.19) as explained in Section 2.2.3.2.1
4. Capture of oscillation around the wave drag domain by the "shock margin" as explained in Section 2.2.3.2.2
5. Capture of the cells adjacent to the aerodynamic body surface by the "wall margin" as explained in Section 2.2.3.2.3
6. Capture of oscillation around the profile drag domain by using the "boundary-layer margin" as stated in Section 2.2.3.2.2.

The addition of induced drag, as described in Section 2.2.3.3, gives the total drag. The procedure described in Section 2.3.1 produces an almost constant total drag independent on the grid number. The entropy production, not related to the shock wave, boundary layer, and wake, is excluded, as shown in Section 2.3.2.

However, the procedure comprises some arbitrarinesses. First, the cutoff values for the shock and boundary-layer functions are determined empirically. Especially, boundary-layer cutoff value can be selected from a range of values, and the resultant profile drag varies depending on the cutoff value selected. Additionally, the selection of the margins around the domains affects the drag. Generally, for WTT, drag variation less than 1 drag count cannot be discussed because repeatability error of world class wind tunnels is approximately 1–2 drag counts [80, 81, 82]. For example, the repeatability error of the JAXA 2 m $\times$ 2 m transonic wind tunnel is 1.5 drag counts [79].

The shock cutoff variation does not affect the total drag because the spatial drag oscillation around the shock wave cannot be captured only by using the shock function, as shown in Fig. 2.6. It is not feasible to capture the spatial drag oscillation at the edge of

the boundary layer by varying the boundary-layer cutoff because the cutoff value hardly variates at the drag oscillation, as shown in Fig. 2.10. Therefore, the cutoff values are used to roughly capture the wave and profile drag domains.

Those spatial drag oscillations at the domain edge areas which are captured by the shocek function F_{shock} and boundary-layer function F_{bl} are eventually covered by margins. Therefore, the uncertainties of resultant drags are mainly dependent on the margins. The variations brought by the margins are relatively large and are more than several counts of drags at a few margin levels especially for the boundary-layer margin, as shown in Fig. 2.9(b). However, the graph of the drag variations almost flattens when margin numbers are increased, especially for the medium and fine grids (Fig. 2.9). This is because outside the wave and profile drag domains, drag does not appear unless spurious drag is not produced.

In Section 2.2.3.2.2, specific values of margin layers are chosen. For the wave and profile drag margins, 5 and 4 layers are selected, respectively. They are used for all the grid resolution levels because they depend only on characteristics of the employed numerical schemes in the computation. For the wall margin, 5, 8, and 11 layers are selected for the coarse, medium and fine grids, respectively. If the flow structure is the same among the grids, the cells between the domain captured using only the boundary-layer function F_{bl} and the model wall should be constant, and the number of layers depend on the grid density.

It is checked visually that the spatial oscillations to be captured are favorably included by the margins. Thus, the possibility of uncertainties of the wave and profile drags should be discussed depending on the number of margin layers that the margin growth stops.

For the wave drag domain, although the medium and fine grids experience drag variations less than 0.2 drag counts, the drag of the coarse grid varies by almost 1 drag count (Fig. 2.9(a)). As shown in Fig. 2.18(a), with five levels of wave drag margins determined as the appropriate margin for this analysis, the wave drag domain results in a drag very close to the spurious drag emitted from the leading edge. Accordingly, additional wave-drag margin layers for the wave drag domain of the coarse grid will lead to contamination due to the spurious drag production. If the spurious drag production and wave drag domain are independent of each other and the contamination can be avoided through visual inspection, the contamination is immaterial. If the spurious drag production intersects with the wave drag domain, the drag decomposition analysis is invalid. There is an arbitrariness for layer number of the wave drag margin, and the differences between the selected level and

the next level are 0.03, 0.00, and 0.01 drag counts for the coarse, medium, and fine grids, respectively.

For the profile drag domain, the spatial oscillation must be removed only from around the edge of the detected domain by using the boundary-layer function, as shown in Fig. 2.10. Thus, several layers of the boundary-layer margin are enough. Therefore, four layers of boundary-layer domain were set in this analysis (Fig. 2.9(b)). More layers allow the gradual increase of resultant drag, especially for the medium and coarse grids (Fig. 2.9(b)). The number of margin layers is judged mainly by the results of the medium and fine grids because it is difficult for the coarse grid to determine the end of the drag variations due to the spatial oscillation. As stated in Section 2.2.3.2.2, characteristics of the spatial oscillation of drag production depends on the numerical scheme, and the same number of layers should be applied to similar computations by the same solver. Four layers were selected in this analysis because the drag difference for a five-layer case are 0.76, 0.09, and 0.07 for the coarse, medium, and fine grids, and they are adequately less than 1 drag count, with their variations at less margin layers. As the selection of the number of layers is entrusted to a drag decomposition analysis operator, there is possibility of five layers being selected. Errors due to this selection arbitrariness are as described earlier for differences between four and five layers of boundary-layer margins.

For the wall margin, 5, 8, and 11 layers are selected for the coarse, medium, and fine grids, respectively, and the arbitrariness errors between the next level of layers are 0.31, 0.10, and 0.05 drag counts for each grid.

Simple sums of arbitrariness errors are 1.10, 0.19, and 0.13 drag counts for the coarse, medium, and fine grids, respectively. They are almost equal or less than the wind tunnel repeatability error requirement (= 1.0 drag count or so). If the margins were not introduced, these uncertainties would not be attained.

2.3.4 Off-Design Points

For the medium grid, not only the design point ($C_L = 0.5$) but the points at the attack angles of 1.5°, 2.0°, 2.5°, 3.0° and 4.0° are also examined using the drag decomposition method. The sums of the profile and wave drags are compared with the idealized profile drag ($= C_{D\text{surface integral}} - \frac{C_L^2}{\pi A}$) in Fig. 2.19 ($A$ in the definition of the idealized profile drag represents the aspect ratio of the main wing, and that of the NASA CRM is defined as 9.0). The idealized profile drag was used in the DPW-IV [4] to examine drag without influence

of lift. If the airplane's lift distribution is ideal and there is no spurious drag, the idealized profile drag agrees with the entropy drag ($=C_{D_v} + C_{D_w}$).

The difference between the entropy drag and idealized profile drag at $C_L = 0.5$ is close to the difference between the surface integral and drag decomposition of the medium grid in Fig. 2.14. Fig. 2.20 depicts the decomposed drag components and shows that the estimated Maskell's induced drag curve agrees very well with the idealized induced drag ($\frac{C_L^2}{\pi A}$). This implies that the difference beween the entropy drag and idealized profile drag almost corresponds to the spurious drag. Therefore, the entropy drag curve in Fig. 2.19 would be expected to be close to an idealized profile drag with a sufficiently small grid.

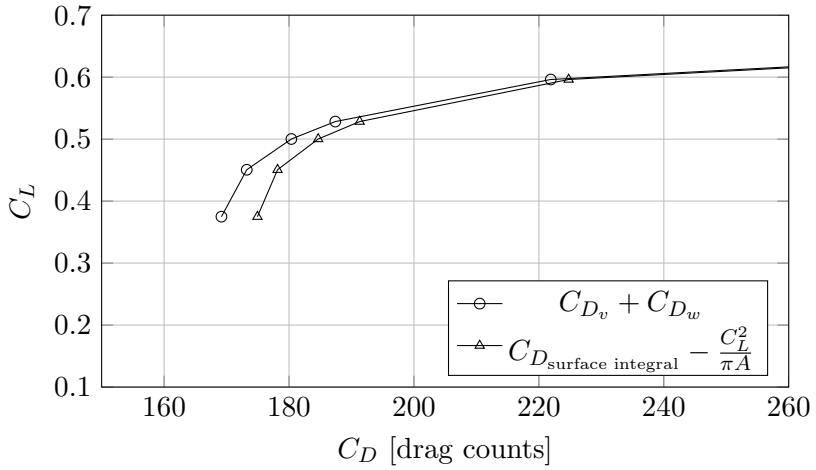

Figure 2.19 Comparison between $C_{D_v} + C_{D_w}$ and idealized profile drag (medium grid).

It is easier to use the decomposed drag components to examine the cause of variations of drag polar instead of the idealized profile drag because it can give physical insights and visual information. For example, it is remarkable that the polar curves are steeply cranked over $C_L = 0.5$ in Fig. 2.19. To determine the cause of this, decomposed drag components of the polar are examined in Fig. 2.20. The wave and profile drag curves increase at a higher C_L. Notably the profile drag curve is cranked at $C_L = 0.6$, this gives the steepness to the drag curve.

Visual inspection of drag integrand distribution is also performed to determine the cause of this crank. In Fig. 2.21, distributions of drag production due to entropy are shown as iso-surfaces of the entropy drag integrand ($cd_s = 0.01$), for $C_L = 0.5$ ($\alpha = 2.318°$) and $C_L = 0.6508$ ($\alpha = 4.0°$) in Figs. 2.21(a) and 2.21(b), respectively. Corresponding to the wave drag

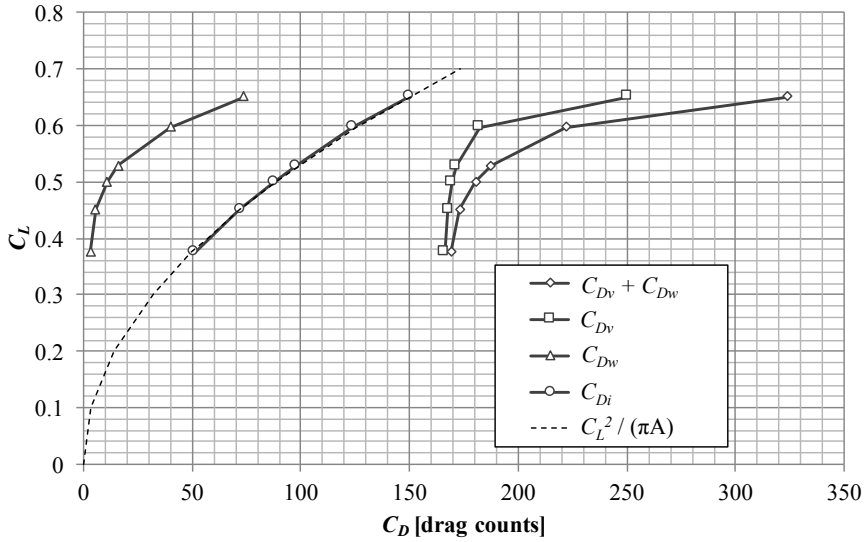

Figure 2.20 Decomposed drag polar (medium grid).

increase with C_L in Fig. 2.20, an expansion of the drag production domain from Fig. 2.21(a) to Fig. 2.21(b) due to the shock wave is observed over the wing. Otherwise, the only distinct difference should be the drag hump emerging from the wing-body juncture. Thus, it could be presumed the difference is caused by the profile drag divergence over $C_L > 0.6$ in Fig. 2.20. It is reported that the solutions at the higher attack angles used in this analysis estimate excess separation around the aft wing-body juncture, and an improvement was brought about by introducing nonlinear turbulence models [53]. Although the predictions for the higher attack angles in the DPW-IV showed large scatter due to this flow separation [4] (the cause is still under discussion in the workshop), the decomposed drag clearly indicates which drag component provides the drag divergence (Fig. 2.20) and where the divergence is caused (Fig. 2.21).

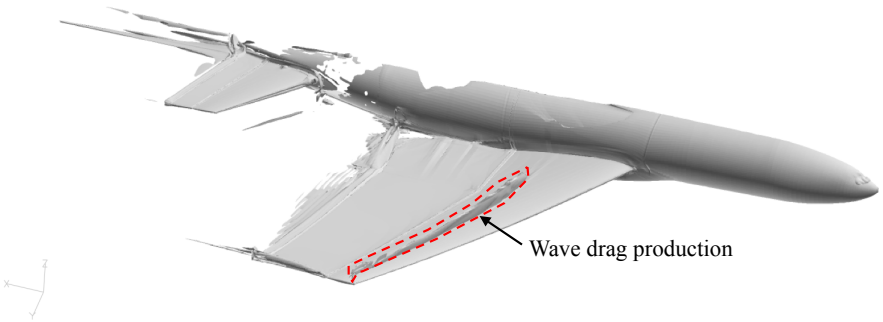

(a) $C_L = 0.5$ and $\alpha = 2.314$ deg

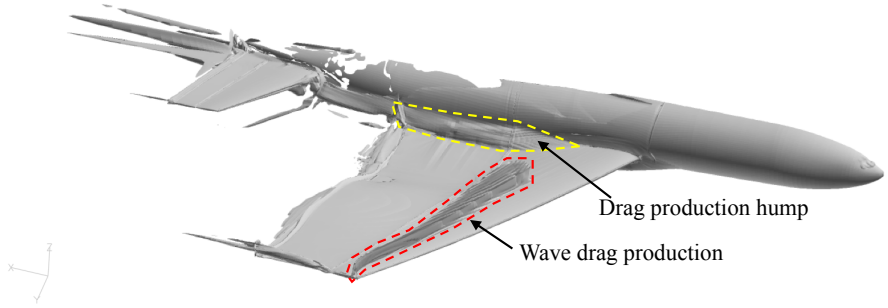

(b) $C_L = 0.6508$ and $\alpha = 4.0$ deg

Figure 2.21 Iso-surface of entropy drag integrand ($cd_s = 0.01$) of moderate and high attack angle cases of the medium grid.

2.4 Conclusions

The influence of spurious drag on a grid convergence characteristics of CFD results of the NASA CRM was revealed with the application of the drag decomposition method, and the following conclusions were drawn:

- Even for a coarse grid with 2.8 millon cells, spurious drag was effectively removed from the computed overall drag, and the resulting values are close to the drag estimated by a grid convergence study using the conventional surface integral. The remaining errors are almost within ± 1.5 drag counts. This indicates that in this case, the excessive drag due to coarser computational grid is not caused by the difference in physical flow structure but by the numerical error.

- It was shown that the coarser grid might cause interference between the spurious drag emitted from the leading edge of the main wings and the wave drag production. Thus, the 2.8 million cells can be estimated as the lowest limit that can keep the flow structure consistent in this case.

- The comparison with the idealized profile drag polar curve shows that spurious drag was satisfactorily removed using the drag decomposition method not only at the design point but also for off-design points.

- Drag components calculated using the drag decomposition analysis can reveal drag production characteristics, such as the cause of the drag divergence, both quantitatively and qualitatively.

- Drag production visualization can provide effective insights into drag production, and the drag divergence was determined to initiate from the wave-drag domain expansion and results in divergence because of the wing-body juncture separations.

- Spurious drag was found in all grid resolution levels, and the drag decomposition method is not perfect but it is, nevertheless, useful. Thus, there is a real need to reduce the generation of spurious drag through the development of better numerical methods for solvers and grid generation.

Thus, drag decomposition analysis is proved to be a useful method for analyzing drag production in CFD flow fields both quantitatively and qualitatively. At present, the drag

production domain-selection methods for wave and profile drags are not perfect, and require cutoff-value detection and geometrical margin expansion. Chapter 3 describes the improvement of profile drag domain selection.

Owing to the increasing availability of computational resources, performing analyses by using high-quality grids of high density is becoming feasible, and spurious drag might be less of a concern in such cases. However, the optimization loops or airplane development campaigns require more than hundreds of flow computations; therefore, coarser grids are favorable in such cases. In addition, an important advantage of the drag decomposition analysis is that the decomposed results provide guidance to the conceptual design process and provide methods for reducing fuel consumption.

Chapter 3

Refinement of Boundary Layer Detection for Drag Decomposition of Computational Subsonic Flow Field

3.1 Introduction

In Chapter 2, the drag decomposition process consists of iterations of volume integrals to capture appropriate cells to be integrated. This chapter introduces new method to reduce iterations for determining profile drag domain to one calculation by employing the concept of determining boundary layer thickness in the Baldwin–Lomax turbulence model.

The drag decomposition, or the far-field method, is an alternative method to the surface integral, or the near-field method, for calculating the aerodynamic drag exerted on a body immersed in fluid from a computational flow field [70, 30, 29, 26]. The drag decomposition separates the drag components into profile (or viscous), wave, induced, and spurious drags. Additionally, it can visualize the drag production distributions. Recently, the method has become not only a theoretical alternative but has been used in some practical applications, as shown in Chapter 2 or in the following literature: aerodynamic analyses of wing-body shapes in European collaboration projects, such as the AIRDATA [29] or the GARTEUR and the EUROSUP [30]; aerodynamic optimization [83]; analysis of a result of the 5th AIAA

Drag Prediction Workshop [55].

The drag decomposition method generally divides a computational domain into profile, wave, and spurious drag-related domains, and performs volume integral in each domain (See Section 2.2.2). Therefore, the decomposed quantities depend on the domain division method. Tognaccini [29] introduced a boundary-layer sensor named "boundary layer function" utilizing eddy viscosity (Eq. (2.19)) for determining profile drag domain, which is robust and easy to implement; it has been used in many applications [30, 83, 55]. A downside of this method is that it requires repetition of volume integral to determine an appropriate value of the sensor. The appropriate value of the sensor is calles as "cutoff" in this dissertation. Additionally, it fails to capture drag production at the edge of the boundary layer, at the domain close to the model surface and around the leading edge because eddy viscosity is weak in these domains. To overcome this, in some studies [74, 2], the detected domain is geometrically extended to capture the missed domains, as described in Chapter 2. However, the procedure is cumbersome and time consuming because it needs repetition of volume integral for drag decomposition to determine not only appropriate values for the sensors but also number of the extension layers.

In this chapter, a new method to determine the profile drag domain (=the boundary layer + the wake) is introduced to reduce the time required to perform drag decomposition study. Specifically, this method employs the concept of determining boundary layer thickness in the Baldwin–Lomax turbulence model to avoid repetition of volume integral. The characteristics of the proposed method and the detected viscous drag are examined using 2-dimensional RANS simulation of compressible subsonic flow around the NACA0012 airfoil without shock waves.

3.2 Method

3.2.1 Drag Decomposition Method

In this chapter, the theory of the drag decomposition method explained in Section 2.2.2 is used. Thus, it is not repeated here. To compute the drag, Eq. (2.13) is mainly used in this chapter, instead of Eq. (2.15) used in Chapter 2. Eq. (2.15) is a 2nd-order approximation of Eq. (2.13) which achieves better precision. In contrast, Eq. (2.15) achieves decomposition of the profile drag into entropy and enthalpy contributions. As heat addition is not included in the analyses in this dissertation, the effective difference is of the order of accuracy.

The results of Eq. (2.13) are compared with the results obtained using Eq. (2.15) in Section 3.3.6.

3.2.2 Method to Compute Flow Field

A flow field computed using the fully turbulent RANS equations is used to examine the proposed boundary-layer-detection method. The data used in this Chapter are newly computed for this purpose. The Unified Platform for Aerospace Computational Simulation (UPACS) [64, 65], which is a standard CFD code for multiblock structured grids developed at JAXA based on a cell-centered finite volume method, is used as the flow solver. The 2nd-order Roe scheme is used for the convective computation, and the Spalart–Allmaras one-equation turbulence model [69] is employed. Computation is conducted for the 2-dimensional flow field around the NACA 0012 airfoil. The computational grid type is a C-grid and four levels of grid density are prepared: 113×33, 225×65, 448×129, and 897×257. The grids located on the airfoil are 65, 129, 257, and 513, respectively. Images of the grid are shown in Fig. 3.1. The origin of the coordinate system is located at the leading edge of the airfoil, and the length scales are nondimensionalized by the chord length of the airfoil. The free-stream Mach number, Reynolds number, and reference static temperature are set at 0.6, 6×10^6, and 300 K, respectively. The attack angle is fixed at 0°.

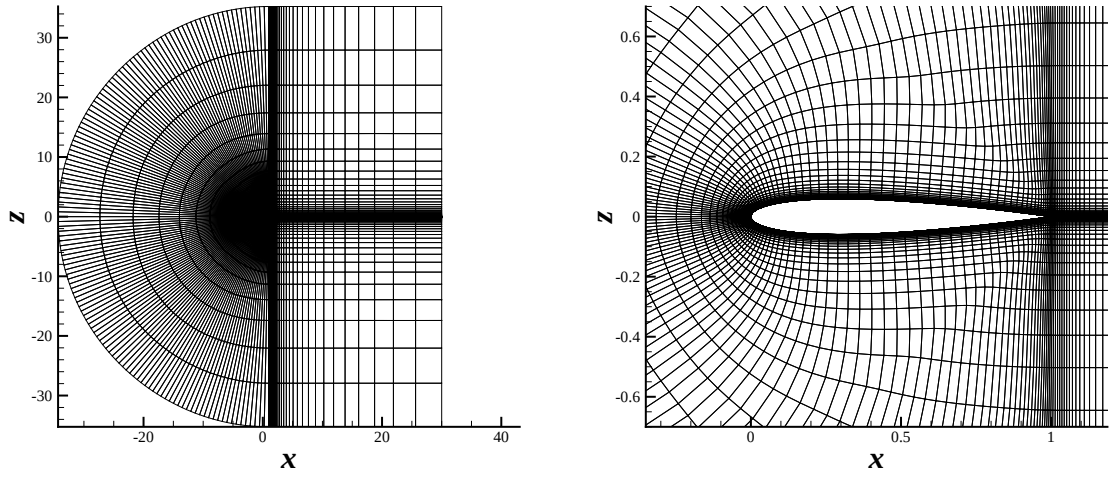

(a) Far view.

(b) Close-up view.

Figure 3.1 Grid images around NACA0012 airfoil (the grid density is 225×65).

3.2.3 Boundary Layer Detection

3.2.3.1 Conventional Method

Tognaccini [29] proposed employing eddy viscosity as a boundary layer sensor for fully turbulent flows; specifically, he adopted Eq. (2.19). The domain in which F_{bl} is greater than an appropriate value can be selected as the boundary layer. This sensor has been used in previous works such as those by Destarac [30], Yamazaki [83], and Gariépy [55]. Chapter 2 describes a procedure to determine an appropriate value of F_{bl}.

As shown in the conservation equation of the entropy [84],

$$T\frac{DS}{Dt} = \frac{1}{\rho}\tau_{jk}\frac{\partial u_j}{\partial x_k} - \frac{1}{\rho}\frac{\partial q_k}{\partial x_k}, \tag{3.1}$$

which is derived from the Navier–Stokes equations, the entropy production is directly related to the viscosity. In a fully-turbulent high Reynolds-number flow simulation employing a turbulence model, viscosity is mainly produced through eddy viscosity inside the boundary layer. This implies that the eddy viscosity itself is dominantly producing the viscous drag. Therefore, it is straight forward to select the domain, in which the eddy viscosity is significantly large, as the profile drag domain. The Tognaccini's boundary layer function F_{bl} (Eq. (2.19)) represents the ratio of molecular and eddy viscosities, and its value exceeds 10.0 around the area close to the airfoil, that is, the boundary layer. However, it requires the repetition of volume integral to determine an appropriate boundary layer function value and number of layers of boundary layer marginal domain, as explained in Section 2.2.3.

3.2.3.2 Boundary-Layer-Detection Method Introduced in This Study

To avoid the repetition of volume integral, a new method is proposed in this chapter for detecting the boundary layer. The primary objective of the new method is to avoid the repetition of the drag decomposition process for determining the boundary layer domain. Therefore, the method employs the boundary-layer-thickness-detection concept of the Baldwin–Lomax turbulence model [56] to determine the domain with one drag decomposition calculation.

The Baldwin–Lomax model was developed to improve the Cebeci–Smith turbulence model [75], which is a two-layer model with ν_T given by separate expression in each layer, and the eddy viscosity of the outer layer ν_{T_o} in terms of the normal distance from the nearest

solid boundary y is

$$\nu_{T_o} = \alpha_{cs} U_e \delta_v^* F_{Kleb}(y;\delta), \tag{3.2}$$

where α_{cs}, U_e, δ_v^*, and $F_{Kleb}(y;\delta) = \left[1 + 5.5\left(\frac{y}{\delta}\right)^6\right]^{-1}$ are closure coefficient, shear-layer edge velocity, boundary layer velocity thickness, and Klebanoff's intermittency function, respectively. This expression of F_{Kleb} appears in [75] and is an approximation of the original approximation of the experimental data by Klebanoff [85]. For this, the boundary layer thickness δ must be known beforehand. The Baldwin–Lomax model is formulated for situations where boundary layer properties, such as the thickness δ, are difficult to determine [76]. In the model, δ in Klebanoff's intermittency function is replaced by y_{max}/C_{kleb}, where y_{max} is the value of the coordinate normal to the solid surface y at which $F(y) = y\,|\omega|\left[1 - e^{(-y^+/A^+)}\right]$ achieves its maximum value. In the equation, $|\omega|$ is the magnitude of the vorticity and $y^+ = \frac{\rho_{\mathrm{wall}} u_\tau y}{\mu_{\mathrm{wall}}} = \frac{\sqrt{\rho_{\mathrm{wall}}\tau_{\mathrm{wall}}}y}{\mu_{\mathrm{wall}}}$, where the subscript *wall* denotes quantities at the wall. The constants appearing in the model are determined by an agreement with the Cebeci [75] formulation for constant pressure boundary layers at transonic speeds. The constants related to this study are determined as $C_{kleb} = 0.3$ and $A^+ = 26$ as written in Wilcox [76].

The new method described in this chapter only employs the concept of the Baldwin–Lomax model to evaluate a boundary layer thickness δ because there is only a slight difference between the predictions of the Baldwin–Lomax and Cebeci–Smith models [76]; this supports the validity of the estimated boundary layer thickness δ in the Baldwin–Lomax model. The thickness δ is used as the edge of the profile drag domain. As the procedure to determine y_{max} does not require repetition of drag integral, this method largely reduces the time needed for drag decomposition analysis.

In the following sections, after presenting the distribution characteristics of the drag integrand around the 2-dimensional airfoil, the domains determined by the conventional and new boundary-layer domain-detection methods are compared.

3.3 Results

3.3.1 Drag Production around an Airfoil

By evaluation Eq. (2.13), viscous drag production around the airfoil is visualized for the 225×65 grid, as shown in Fig. 3.2. Fig. 3.2(a) shows the drag production image around the entire airfoil. Nonphysical (i.e., spurious) drag production is observed around the leading edge, as shown in a close-up image around the leading edge of the airfoil (Fig. 3.2(b)). Rizzi [86] showed that numerical solution of the Euler equations is accompanied by spurious increase of entropy due to numerical viscosity and grid inadequacy; Destarac [30] described that the production of the spurious drag still occurs in the case of the Navier–Stokes equations. This is described in Fig. 3.2(b) and should not be integrated as the drag. To avoid integrating this part, it is necessary to confine the integral domain to the boundary layer.

Fig. 3.2(c) shows the close-up image of drag integrand cd within the boundary layer downstream of the leading edge. Unlike the domain around the leading edge, the cd production is confined inside the domain close to the airfoil surface.

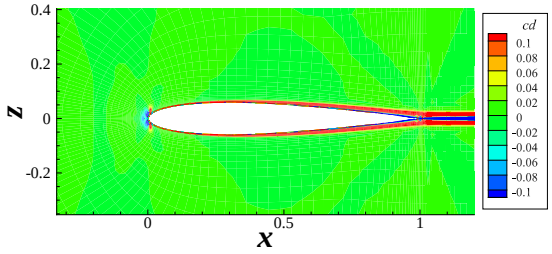

(a) Entire airfoil.

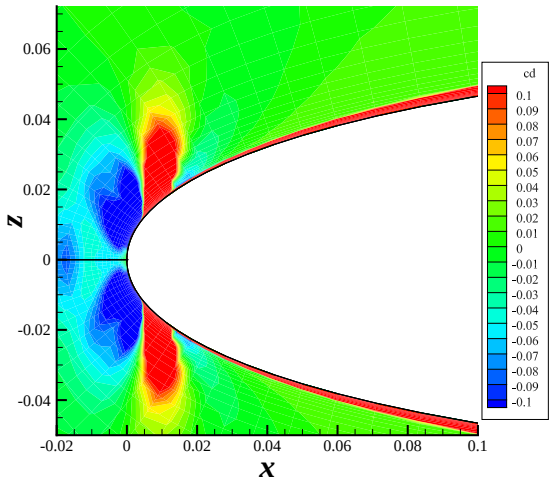

(b) Around the leading edge.

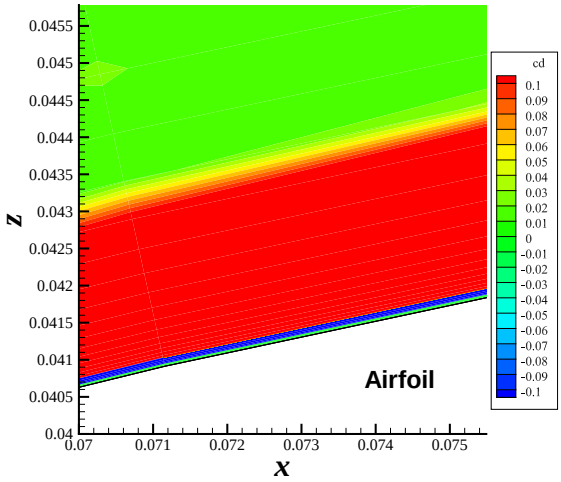

(c) Domain close to the airfoil surface.

Figure 3.2 Entropy drag production contour around the NACA0012 airfoil for the 225×65 grid.

3.3.2 Domain Captured by Conventional Method

As pointed out in Chapter 2, Tognaccini's conventional boundary-layer function requires repetition of integrals to determine an appropriate cutoff value and appropriate numbers of marginal domain layers. Although the appropriate parameters once determined can be applied to similar flow field computed by the same flow solver, the parameter-determining process is the most time consuming part of the drag decomposition analysis. Besides, the determination of such parameters depends on the criteria which the operators of the drag decomposition analysis learned from their experiences.

Moreover, for the flow fields in this chapter, Tognaccini's conventional boundary layer function fails to detect parts of the drag producing domain, such as areas around leading edges (Fig. 3.3(a)), close to the edge of the boundary layer, and close to the solid model surface (Fig. 3.3(b)), because weak eddy viscosity in these domains leads to an extremely low value of the boundary layer function F_{bl}, although the colormap of the drag integrand shown in the background in Fig. 3.3 is excessively emphasized. Boundary layer function cutoff value of 1.4 is employed in Fig. 3.3; Section 3.3.3 states the details for determining the cutoff value. Although drag production in these domains may seem small, integration of values sometimes generates significant amounts. The amount is discussed in Section 3.3.5. Additionally, drag production around the edge of the boundary layer (Fig. 2.10) was not captured. To capture this domain, boundary layer margin is used.

Thus, a new boundary layer sensor that can detect an appropriate domain without parameter surveys is preferred.

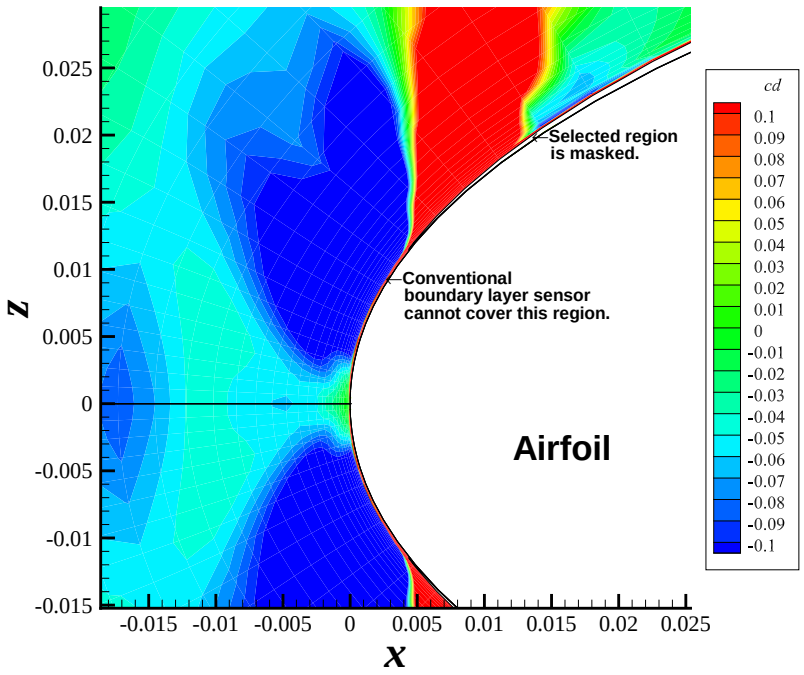

(a) Around the leading edge.

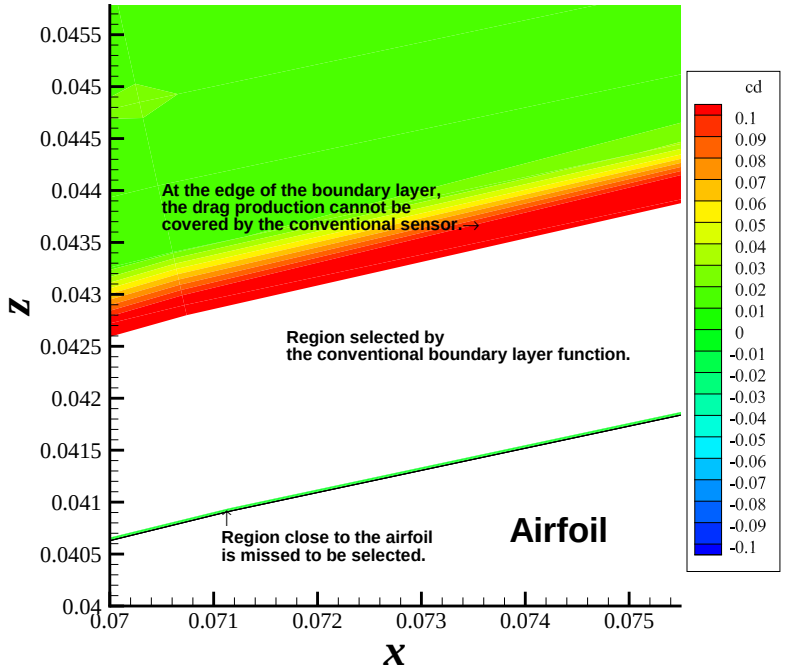

(b) Domain close to the airfoil surface.

Figure 3.3 Boundary layer detected using the conventional Tognaccini's boundary layer function ($F_{\mathrm{bl}} = 1.4$) over entropy drag production contour for 225×65 grid.

3.3.3 Difficulty to Determine Appropriate Boundary Layer Sensor

The boundary layer domain detected using the conventional boundary layer function F_{bl} depends on its selected cutoff value. Empirically, a carefully chosen value can be adequately applied to a number of similar computational cases computed by the same solver.

The dependency of the computed drag coefficient on the cutoff value of the conventional boundary layer function F_{bl} for the present investigation is shown in Fig. 3.4. A value close to 1.0 results in almost the entire domain being detected as the integral domain. However, a very high value gives an inadequately narrow domain for the boundary layer. Therefore, a visual inspection must be conducted to choose an appropriate value.

For the case of grid 225×65 (Fig. 3.4(a)), there is an obvious cliff around 1.2, as shown in the figure, and thus a value slightly greater than 1.2 would seem to be appropriate. In contrast, for the 897×257 grid (Fig. 3.4(b)), it is difficult to determine an appropriate value of F_{bl} because there are small fluctuations around $F_{\mathrm{bl}} = 1.2$ and a gradual decrease of integrated value but no obvious changes. The reason for selecting an appropriate cutoff value is explained in the following paragraph

To examine the detected boundary layer for some particular values, images of the detected domains are presented as white-masked domains superimposed onto the drag integrand images in Figs. 3.5 and 3.6 for the 225×65 grid and in Figs. 3.7 and 3.8 for the 897×257 grid. For both these grids, differences between the detected domains are obvious and similar. When the cutoff value of F_{bl} is set at 1.2, almost the entire domain except for areas just above the top and beneath the bottom of the airfoil is selected as the boundary layer. Spikes can be observed in both plots in Fig. 3.4 around $F_{\mathrm{bl}} = 1.2$, and the shape and size of the selected domains vary greatly around this value. When the cutoff value is increased to 1.3, the detected boundary layers are almost reasonable but there are circular artificial domains close to the leading edges (Figs. 3.6(a) and 3.8(a)). Eventually, at $F_{\mathrm{bl}} = 1.4$, the detected boundary layer domain appears reasonable (Figs. 3.5(c) and 3.7(c)); however, even in this case it lacks the domains close to the airfoil surface, boundary-layer edge, and leading edge, as shown in Fig. 3.3. To include those missed domains, the detected domain must be extended, for example geometrically as described in Section 2.2.3.2.2; however, this introduces another arbitrariness and requires parametric studies (= repetition of drag decomposition procedure to determine an appropriate value of marginal layers). To avoid complication, such domain extensions are not applied on the results in this chapter.

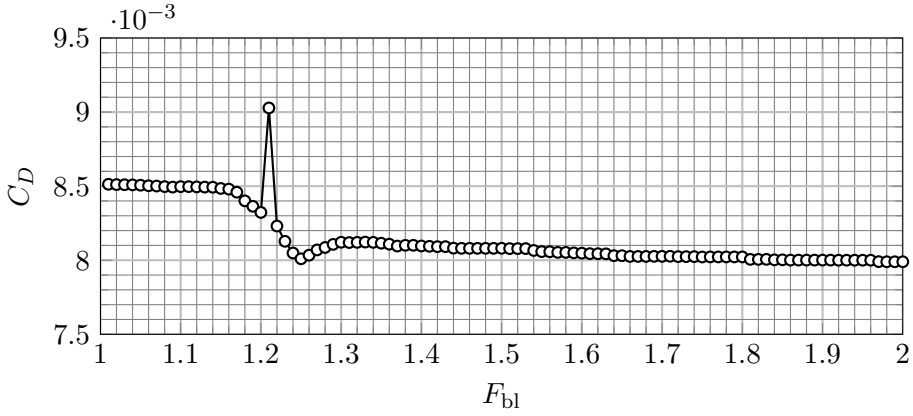

(a) 225×65 grid.

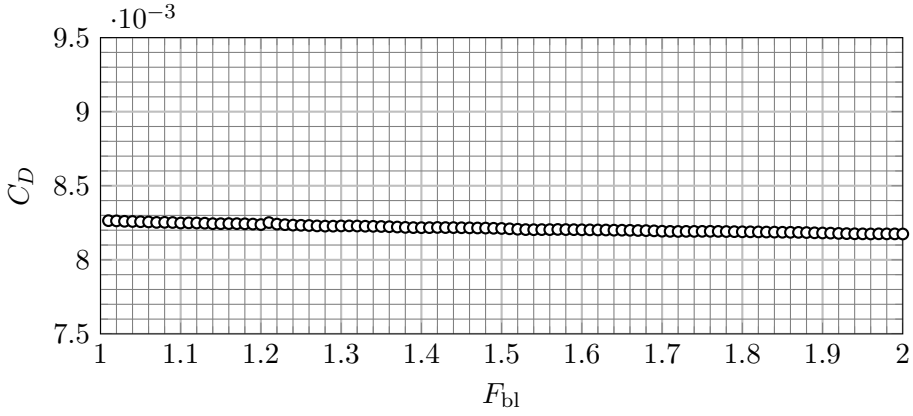

(b) 897×257 grid.

Figure 3.4 Drag coefficient versus conventional Tognaccini's boundary layer function.

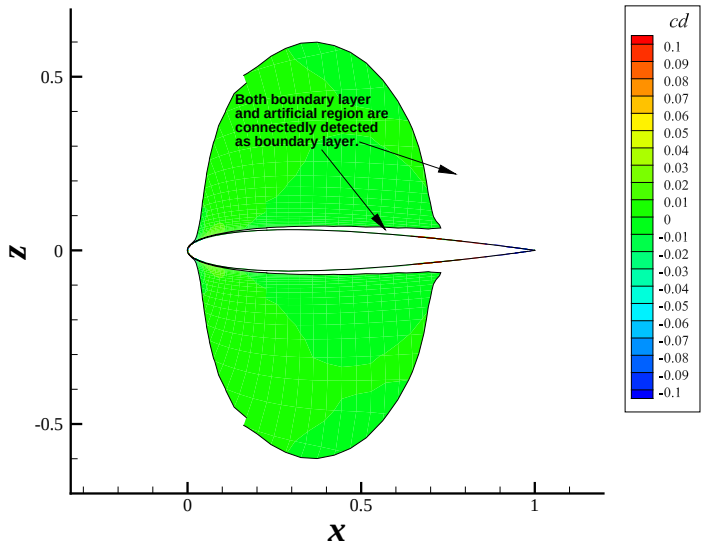

(a) $F_{\mathrm{bl}} = 1.2$.

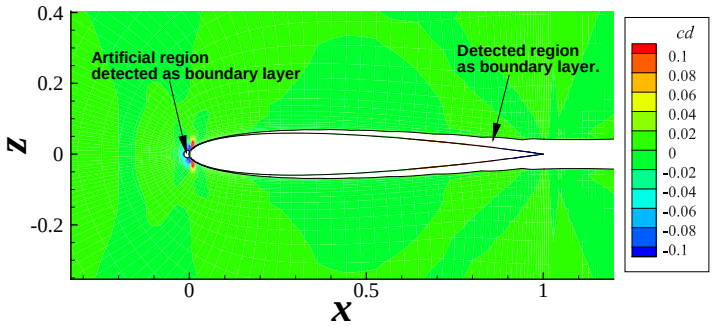

(b) $F_{\mathrm{bl}} = 1.3$.

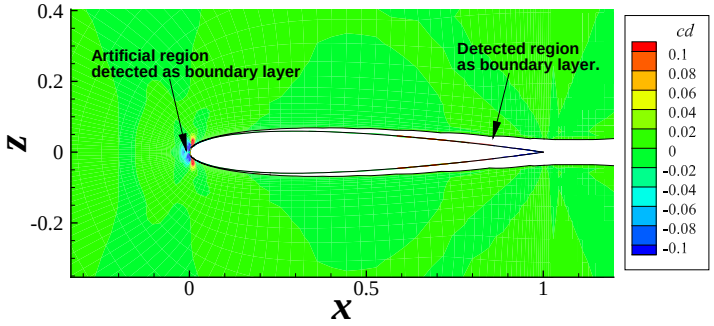

(c) $F_{\mathrm{bl}} = 1.4$.

Figure 3.5 Detected boundary layer cells masked using the conventional Tognaccini's boundary layer function over entropy drag production contour for 225×65 grid.

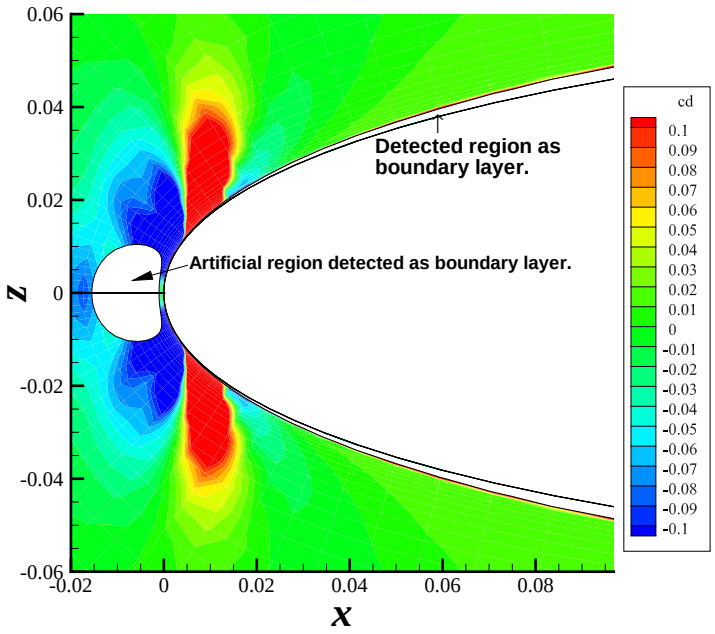

(a) $F_{\mathrm{bl}} = 1.3$.

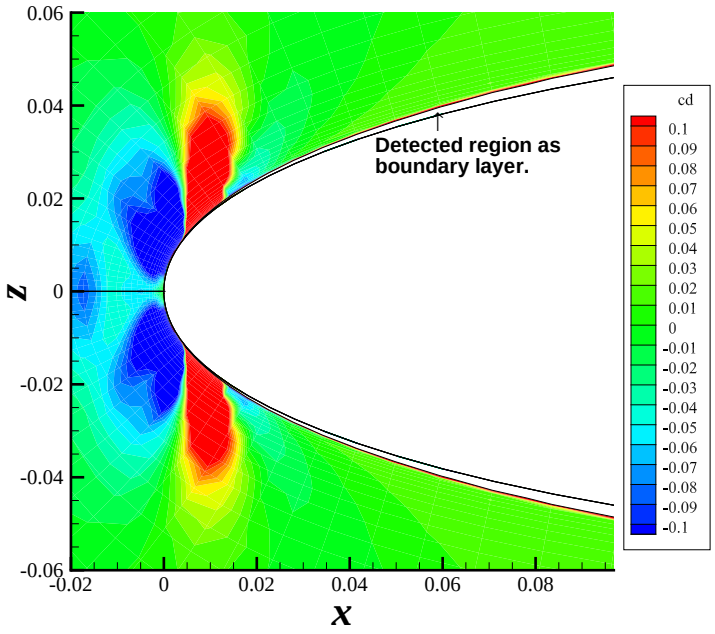

(b) $F_{\mathrm{bl}} = 1.4$.

Figure 3.6 Close-up images of detected boundary layer cells masked using the conventional Tognaccini's boundary layer function over entropy drag production for 225×65 grid.

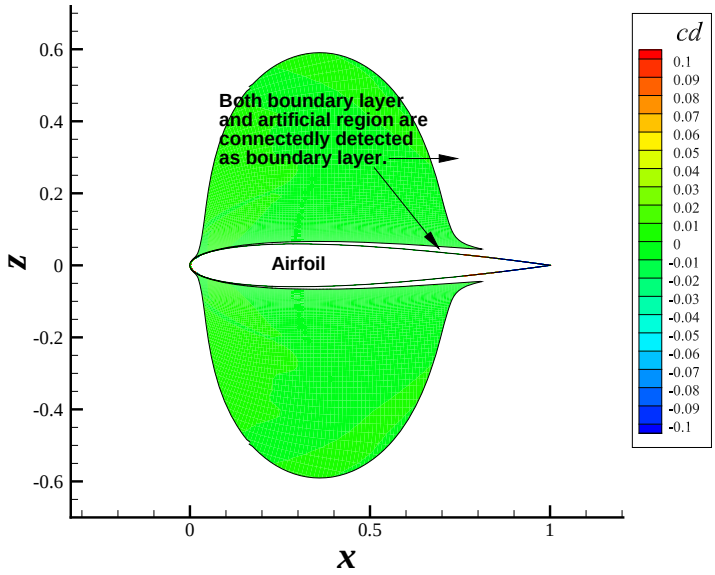

(a) $F_{\mathrm{bl}} = 1.2$.

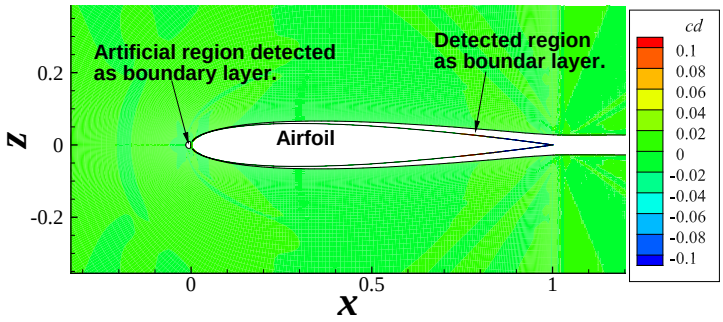

(b) $F_{\mathrm{bl}} = 1.3$.

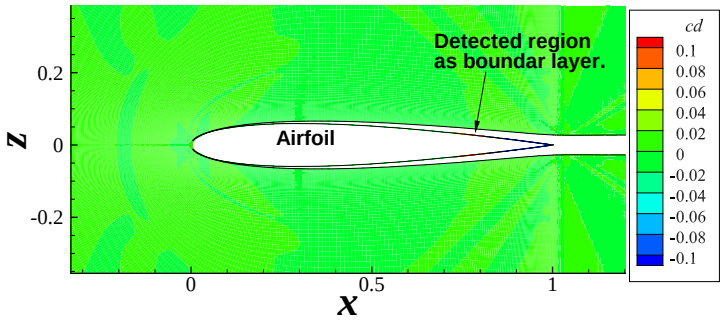

(c) $F_{\mathrm{bl}} = 1.4$.

Figure 3.7 Detected boundary layer cells masked using the conventional Tognaccini's boundary layer function over entropy drag production contour for 897×257 grid.

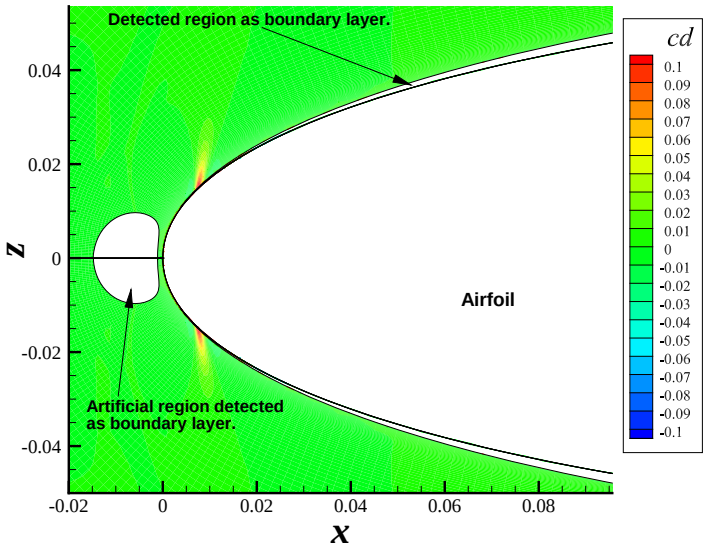

(a) $F_{\mathrm{bl}} = 1.3$.

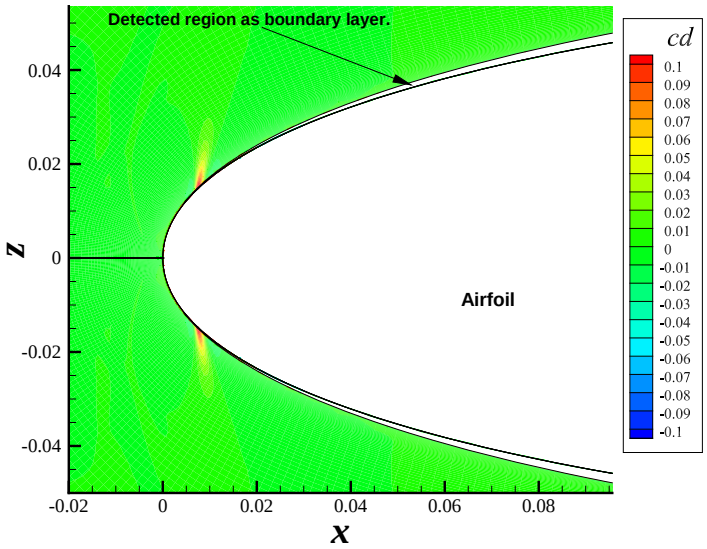

(b) $F_{\mathrm{bl}} = 1.4$.

Figure 3.8 Close-up images of detected boundary layer cells masked by evaluating the value of the conventional Tognaccini's boundary layer function for 897×257 grid.

3.3.4 Domain Captured Using New Method

As stated in Section 3.2.3.2, the new method proposed in this chapter does not require the repetition of volume integral because it determine the boundary layer and wake domain boundary as the boundary layer thickness δ estimated in the concept of the Baldwin–Lomax turbulence model. On the other hand, the conventional method needs the iterative calculation for determining the value of F_{bl} or the numbers of the layers of the boundary layer margin and the wall margin as shown in Section 3.3.3. Then, any parameter determining process is not described when the domain detection is done by the new method.

The domain detected as the boundary layer using the method proposed in this chapter is shown in Fig. 3.9 as a white masked domain. It successfully captures all the domain covered by the conventional sensor and the missed domain pointed out in Fig 3.3, excluding the spurious drag production domain in Fig. 3.2. The unnatural drag productions around the leading edge (Fig. 3.2(b)) are obviously excluded. The resultant estimated drag is quantitatively examined in Section 3.3.5.

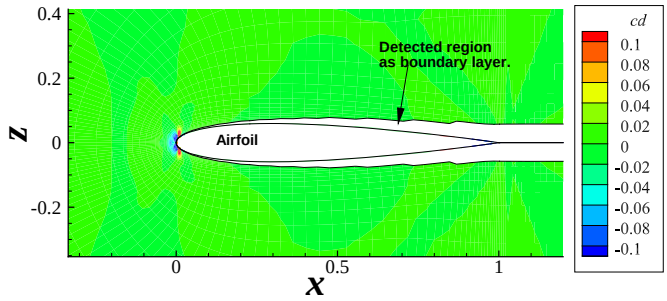

(a) Entire airfoil.

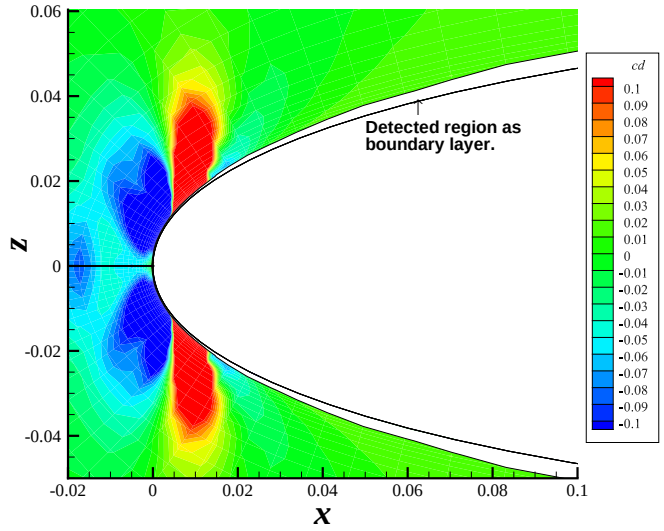

(b) Around the leading edge.

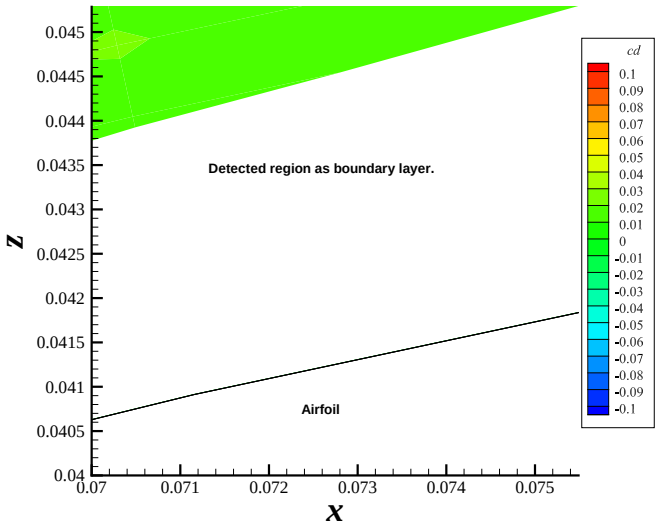

(c) Region close to wall.

Figure 3.9 Detected boundary layer by evaluating the value of the new sensor with Baldwin–Lomax turbulence model's concept for 225×65 grid.

3.3.5 Integrated Drag with the New Boundary Layer Sensor

The drag productions inside the detected boundary layer estimated both by the conventional and proposed boundary-layer-detection method are compared with the near field drag obtained by integrating properties over the airfoil surface. The adequacy of the grid fineness is determined by comparing results at different grid densities. The comparison of drag coefficients is shown in Fig. 3.10. The abscissa of the figure is the inverse of the number of grid points.

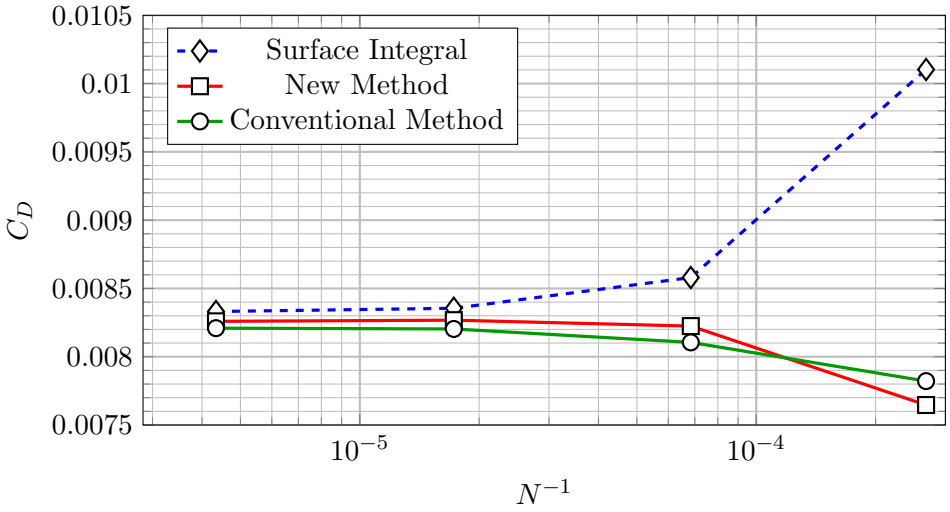

Figure 3.10 Comparison of grid convergence dependency between surface integral and drag decomposition (new and conventional method).

The integral domain should be confined to a volume close to that of the airfoil to avoid including additional spurious drag into the integration. It is generally defined as the integral domain upstream a plane perpendicular to the free stream. This plane is called the "cut-plane" in this dissertation. The effect of the cut-plane's position is discussed later. For the comparison of the boundary layer sensors, the cut-plane is fixed at $x = 1.3$ (0.3 chord downstream from the trailing edge of the airfoil) because the drag variation due to the change of the cut-plane location is stable and less than 1 drag count in the region well downstream (Fig. 3.11). One drag count of drag variation is not significant for WTT; thus, the criterion is applied here.

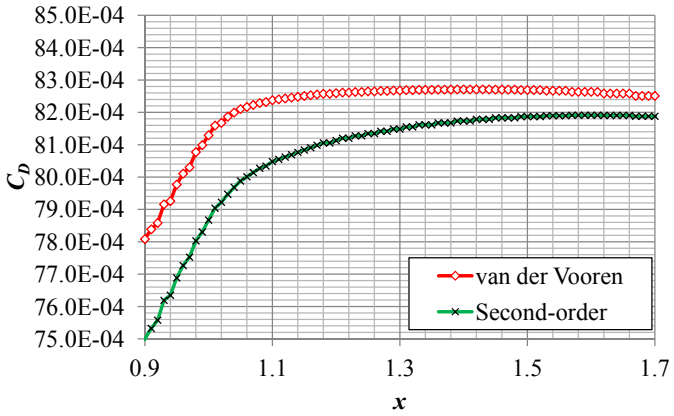

Figure 3.11 Drag coefficient versus cut-plane position for a 448 × 129 grid.

The cost required to obtain the data by using the conventional method should be discussed first. As shown in Fig. 3.4, 200 repeats of the drag decomposition process are used to determine an appropriate F_{bl} value, whereas just one analysis is required to acquire the integral domain by using the newly developed method.

The surface integral shows a fair dependency on grid density. An expected converged value estimated using Richardson extrapolation [87, 88] using the surface integral results is 83.00 drag counts. One drag count is 0.0001 of C_D. The values calculated using the drag decomposition method employing the conventional and proposed boundary-layer detection methods give an almost constant drag value close to the expected convergence value except for the coarsest grid. Further, the new method employing the Baldwin–Lomax turbulence model's method to determine the boundary layer thickness successfully acquires fairly constant values within 1 drag count of the converged value.

The drag coefficient integral calculated using the Baldwin–Lomax boundary layer thickness value is 82.59 drag counts for the 897 × 257 grid. This agrees well with the value of 83.31 drag counts obtained using the conventional surface integral. The grid is determined to be sufficiently fine and the surface integral value is almost the same as the grid converged value.

Finally, the amount of missed drag by the conventional boundary layer function should be discussed. As the new boundary layer sensor catches a larger area than the domain selected using the conventional boundary layer function, the drag value calculated using the new sensor is typically larger. Most of the results excluding those of the coarsest grid follow this assumption. The difference is almost 1.2 drag counts with the 225 × 65 grid.

Although it is still a small value, it is clear that the difference accomplishes more grid dependency to the output employing the conventional boundary layer sensor.

3.3.6 Integral Domain Dependency and Approximation Order

The integral domain determined through the cut-plane position affects the calculated drag value, implying that the wake domain also produces the drag. The dependency on cut-plane position is stronger when a 2nd-order approximation (Eq. (2.15)) by Tognaccini [29] is used instead of Eq. (2.13) by van der Vooren and Destarac [70], while it converges to a closer value as the cut-plane moves downstream (Fig. 3.11).

At the model downstream, the grid is usually rougher and the numerical error can increase. Therefore, the cut-plane should be placed as upstream as possible. Equation (2.13) by van der Vooren and Destarac [70] is thus preferred.

3.4 Conclusions

A new boundary layer sensor based on the Baldwin–Lomax turbulence model's concept of determining boundary layer thickness was introduced to determine the integral domain for the profile drag in the drag decomposition method for a subsonic flow field computed using the RANS simulation. The boundary layer of the simulation is fully turbulent. The new method successfully detects the boundary-layer-related drag production, and has the following advantages over the conventional Tognaccini's boundary layer function, which has been widely used for the drag decomposition method.

1. No parametric survey is required
2. Drag productions around the leading edge and the domains close to the wall are detected properly
3. Drag production around the boundary layer edge is well detected

Practically, by using the conventional method employed in Chapter 2, 200 repetitions of the drag decomposition process were required to determine an appropriate boundary layer function value in the example in this dissertation, whereas by using the newly developed method, only one analysis was required to acquire the integral domain.

Moreover, the effects of the cut-plane position, which determines the stream-wise end of the integral domain, on drag results and of the approximation order on the drag equation were examined. It was shown that the approximation up to the second order requires a longer integral domain to obtain reasonable drag values. Therefore, in a case in which the contribution to drag from the addition of heat can be ignored, Eq. (2.13) by van der Vooren and Destarac [70] would be preferred to a 2nd-order approximation (Eq. (2.15)) by Tognaccini [29] because the cut-plane would be placed as upstream as possible to avoid the numerical error due to the coarser grid downstream.

Chapter 4

Model Deformation Correction Method for Wind Tunnel Test

4.1 Introduction

This chapter shows the correction of the main wing deformation errors mainly on lift force due to dynamic pressure in WTT by using only the experimental data.

To ensure the reliability of CFD drag predictions, the validation of WTT results is crucial. However, inconsistencies among test results might arise because of different wind tunnels and their characteristics; these may be due to several issues, as explained in Chapter 1. Additionally, deformation characteristics due to dynamic pressure differ among wind tunnel models because of differences in their internal structures.

For the common use of CFD predictions and WTT results, a method is required for making a fair comparison between several sources, such as other wind tunnels and CFD codes. If the wind tunnel model is deformed by dynamic pressure, the output acquired in WTT is for the deformed shape, indicating that the data set is inappropriate for comparison not only with CFD but also with data from other wind tunnels. This chapter introduces a method for correcting the data from some WTTs to the data at the design condition. The focus is on model deformation corrections to obtain the aerodynamic data without model deformation from wind tunnel data. The correction is performed on the results of the WTTs of the NASA CRM, which was developed [1] to serve as a reference shape for drag prediction activities of transonic transport airplanes. The details of the NASA CRM are described in Appendix A.1. Specifically, the correction method is applied to correct the

NASA CRM's WTT data of JAXA at the Reynolds number based on the reference chord length c_{ref} (Re_c) of 2.27×10^6 and the WTT data from the National Transonic Facility (NTF) [18, 19] ($Re_c = 5.00 \times 10^6$). Then, the uncorrected and corrected WTT data are compared with the CFD results without deformation at Re_c of 5.00×10^6.

4.2 Facilities and Equipment of JAXA's Wind Tunnel Test

4.2.1 Wind Tunnel

The data and WTT campaign from the NTF were explained in detail by Rivers [18, 19]. In the present dissertation, technical details of only the WTT in JAXA are explained All data used in this dissertation are based on the public data available in [58]. The test campaign is conducted using the JAXA 2 m × 2 m transonic wind tunnel (JTWT). A bird's eye view of the wind tunnel is shown in Fig. 4.1. The JTWT has four interchangeable rectangular test sections, each with the reference height and width of 2 m. A test section with porous walls is used for this test campaign. The perforation holes are perpendicular to the wall surfaces and the opening ratio of the walls is 20%. Total pressure can be maintained between 50 and 120 kPa, and the Mach number can be controlled between 0.1 and 1.4 (The total pressure limit was augmented to 150 kPa after the wind tunnel test campaign for this study). The wind tunnel has a 22,500 kW main blower, and supersonic operation is achieved using a 8,000 kW auxiliary blower. The Mach number is controlled by the total pressure (p_0) and static pressure of the plenum chamber (p_{pc}). The Mach number calculated from p_0 and p_{pc} is called the plenum chamber Mach number (M_{pc}).

4.2.2 Wind Tunnel Model

Details of the NASA CRM itself is explained in Section A.1 of the Appendix. The wind tunnel model used in the JAXA's WTT campaign is explained in this section. The wind tunnel model is a copy of the NASA CRM model tested at the NTF [19], and was scaled by 80% to fit into the smaller JTWT test section. Cross-section images of the NTF and JTWT test sections containing the corresponding models are shown in Fig. 4.2. As seen in the figure, the relative blockage ratios of the models are the same. The geometries of the models are tabulated in Table 4.1.

The CRM represents a typical twin-engined jet airliner configuration with a fuselage,

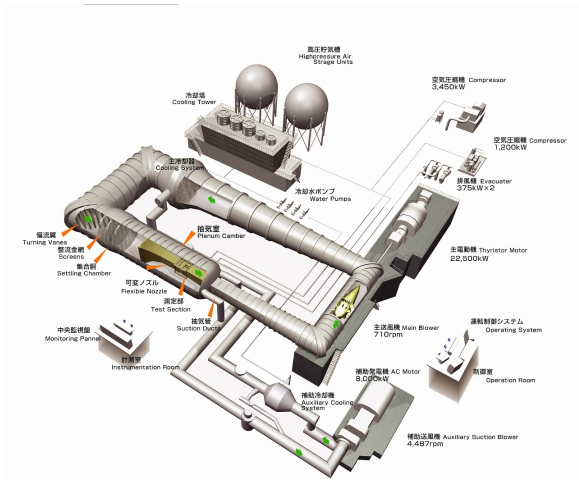

Figure 4.1 Bird's eye view of the JAXA 2 m × 2 m transonic wind tunnel [3].

Table 4.1 Wind tunnel model reference characteristics.

	NTF	JAXA
Reference Area (S_{ref})	0.2797 m^2	0.1790 m^2
Reference Chord (c_{ref})	0.1891 m	0.1513 m
Reference Span (b)	1.587 m	1.269 m

wings, horizontal tailplanes, and flow-through engine nacelles and pylons. Three sets of horizontal tailplanes with deflection angles of $-2°$, $0°$ and $2°$ were prepared. A test without horizontal tailplanes is available, and blanking covers are attached to the holes for the tailplanes in such cases. Similarly, the underwing engine nacelles and pylons are also removable. All the data analyzed in this dissertation are for the configuration without the engine nacelles and pylons. The shape of the model support sting close to the model surface is a scale copy of the sting used in the NTF test; however, as the JTWT test section is shorter than that of the NTF, the aft-end of the sting shape is truncated to locate the model at the proper location in the test section (Fig. 4.3).

A photograph showing the wind tunnel test model installed in the JTWT test section is shown in Fig. 4.4.

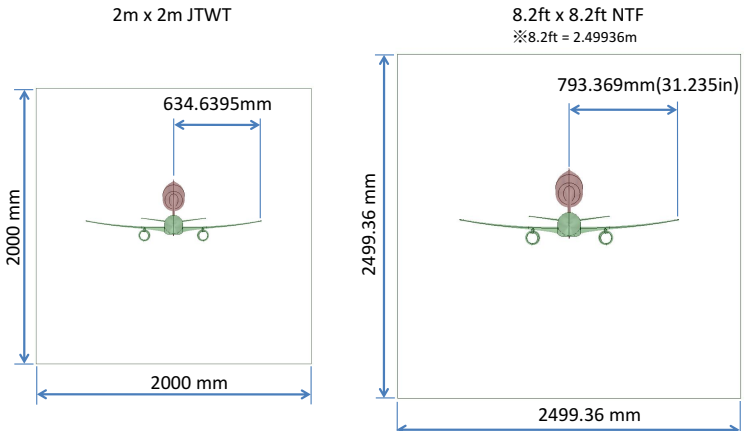

Figure 4.2 Cross-section images of test sections with wind tunnel models.

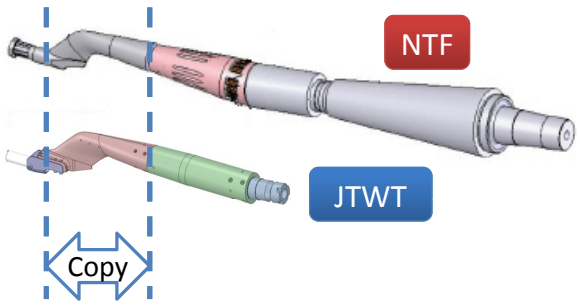

Figure 4.3 Part of the JAXA sting copied from the NTF's support sting.

4.2.3 Measuring Equipment

4.2.3.1 Force and Pressure Measurement

Fig. 4.5 shows the block diagram of the measurement system. Sensor cables are routed through the support sting, but the diameter of the sting limits the number of cables, and hence sensors, that can be used at any given time. Thus, static and unsteady measurements cannot be performed simultaneously. The unsteady data are not used in this dissertation.

Table 4.2 lists the measurement sensors. The arrangement of most of the sensors follows the NTF's model [19]. The model has 370 pressure taps: 325 on the wings, 12 on the fuselage, and 33 on the horizontal tails. Wing pressure taps are located at nine spanwise wing sections. Table 4.3 tabulates the location, the same stations as the NTF's model, with upper surface taps installed in the left wing and lower surface taps installed in the right wing. The η in Table 4.3 represents the spanwise section location normalized by half-span

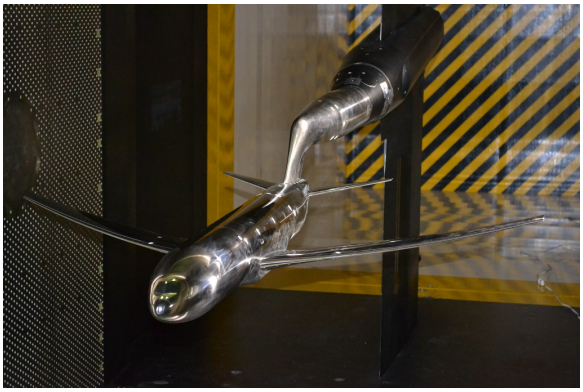

Figure 4.4 Wind tunnel model installed in the JTWT test section.

length $b/2$. The pressure taps are connected to electronically scanned pressure sensor (ESP) modules installed in the model's fuselage by using stainless tubes with an inner diameter of 0.8 mm. The ESP system used is the Pressure Systems Inc. System 8400. The trenches in which the pressure tubes are installed in the wings are curved symmetrically to give the left and right wings the same bending characteristics.

Table 4.2 Measurement sensors on the JAXA's copy of the Common Research Model.

Measurement objectives	Equipment
Aerodynamic force	Six-component balance (internal)
Static pressures	325 taps on the wings
	33 taps on the horizontal tail
	12 taps on the fuselage
	5 taps on the support sting surface
	10 taps on the left nacelle surface
	5 total pressure through the left nacelle
Unsteady pressure	3 taps on the upper surface of the left wing
	1 tap on the lower surface of the right wing
Strain gauges	2 for each wing's bending
	2 for each wing's torsion
Model shape deformation	30 markers on the model surface

The model is installed in the test section supported by the sting through a six-component force balance built into the model. The balance specifications are listed in Table 4.4.

In summary, static measurements consist of aerodynamic force, surface pressure distribution, and wing deformation measurements. Surface pressure distribution measurements include wind-tunnel wall surface pressure measurements for wall interference correction.

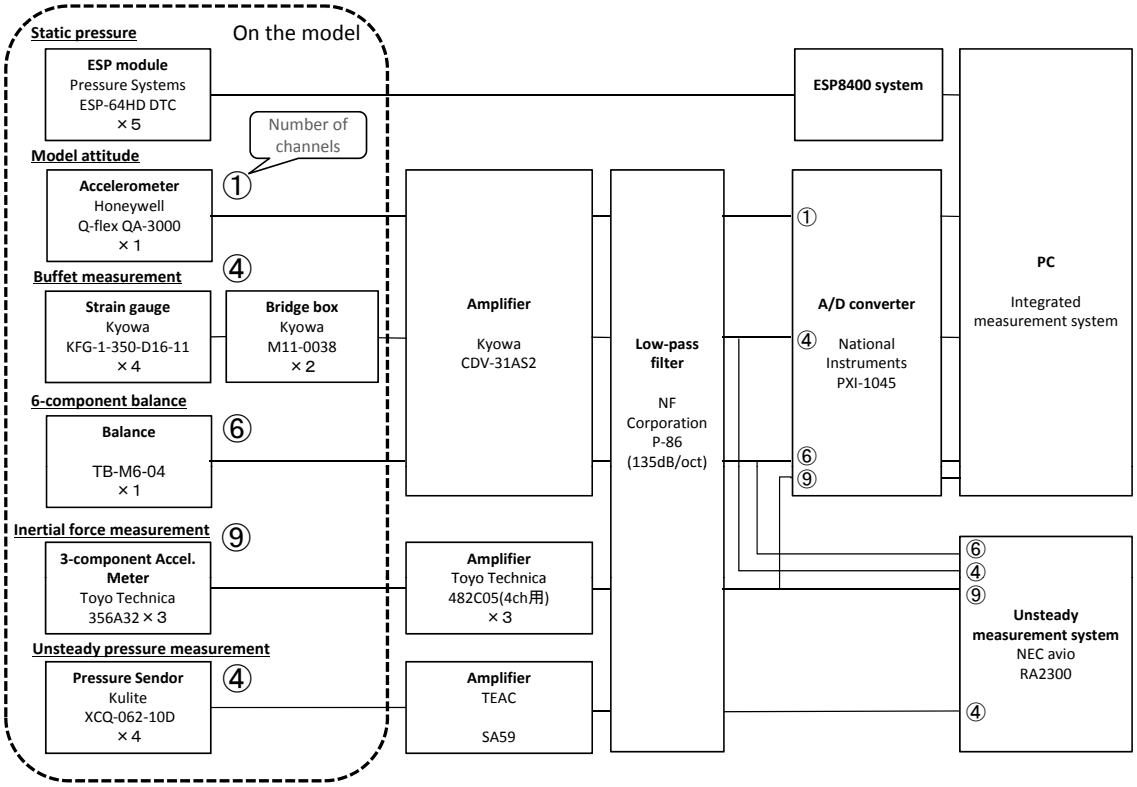

Figure 4.5 Measurement system block diagram

Aerodynamic force measurement is performed using a six-component force balance built into the wind tunnel model.

4.2.3.2 Model Deformation

Wind tunnel models are deformed because of dynamic pressure. The model deformation is measured using an optical method employing markers placed on the model's surface. To avoid any influence of the markers on the force balance output, model deformation measurement is conducted separately. Model deformation is considered to mainly affect the wings, which are fabricated to be as symmetrical as possible so that their deformations are also symmetric; only the deformation of the left main wing is measured. The measurement system consists of two cameras manufactured by Allied Vision Technologies. One camera (29 megapixel Prosilica GX6600) is points downward from the test-section ceiling and another camera (16 megapixel GE4900) points through window in a left side wall (Fig. 4.6). Fig. 4.7

Table 4.3 Locations of pressure measurement sections on the main wing.

Section name	Normalized spanwise location (η)
Section A	0.131
Section B	0.201
Section C	0.283
Section D	0.397
Section E	0.502
Section F	0.603
Section G	0.727
Section H	0.846
Section I	0.950

Table 4.4 Measurement ranges of balance TB-M6-04.

	F_x	F_y	F_z	M_x	M_y	M_z
Full Scale	670 N	4000 N	8000 N	226 N-m	565 N-m	226 N-m
Uncertainty [% F.S.]	0.06	0.11	0.03	0.12	0.05	0.13

illustrates an image captured by the ceiling camera.

Deformation is measured from the 3-D positions of markers on the model surface. Fifteen markers are placed both on the upper and lower surfaces of the main wings, located at 15%, 55% and 95% chord length of five sections at η = 0.16575, 0.33995, 0.5526, 0.7862, and 0.975. Then, the total number of the markers on the main wings are 60. Further, 30 markers are located on the fuselage upper surface.

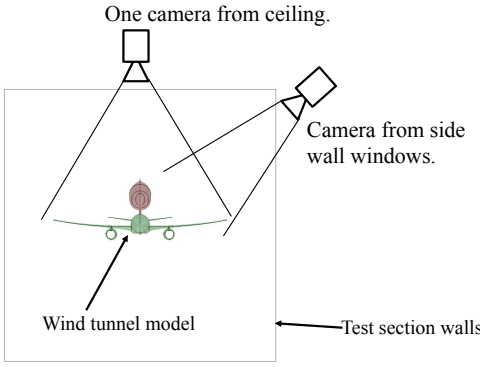

Figure 4.6 Arrangement of model deformation measurement cameras.

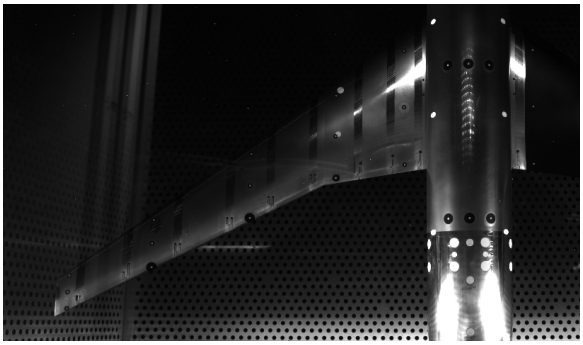

Figure 4.7 Image captured by a model-deformation measurement camera.

4.2.4 CFD Simulations

Pretest CFD simulations are performed prior to the WTT campaign to be compared directly with the wind tunnel data.

The TAS code [89], based on a cell-vertex finite volume method, is used as the flow solver. RANS equations are solved through numerical flux computations employing the Harten–Lax–van Leer–Einfeldt–Wada (HLLEW) scheme [90]. For time integration, the lower/upper symmetric Gauss–Seidel (LU-SGS) implicit method [91] is used. The accuracy of time integration is of the first order. The Spalart–Allmaras one-equation model [69] without the trip term for transition is used as the turbulence model. Spalart's model is employed to estimate the anisotropic Reynolds stress tensor [92].

The computational grid is created over the model geometry with zero tailplane deflection (wing/body/tail = 0°) and includes the sting shape close to the model shape (Fig. 4.8). The number of nodes is approximately 16.2 million, and the number of cells is 45.9 million. The wind tunnel walls and model support strut are not simulated. The computation is performed at a freestream Mach number of 0.85, and the Reynolds number based on the reference chord length c_{ref} is set at $Re_c = 5.00 \times 10^6$. The attack angles are set at 0°, 1°, 2°, 2.558° ($C_L = 0.5$), 3°, 4° and 5°.

4.3 Test Conditions

4.3.1 Wind Tunnel Test of JAXA

The static measurement parameters are aerodynamic force and moment, pressure distribution on the model surface, model deformation, and wind-tunnel wall pressure distribution.

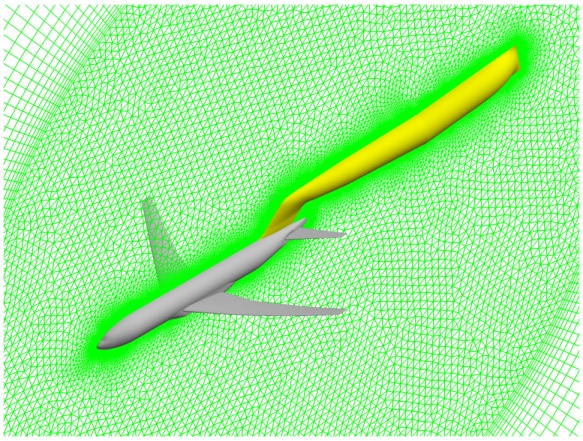

Figure 4.8 Symmetric plane cut-out image of the computational grid of a pretest CFD.

The total pressure p_0 is set at 120 kPa and the total temperature T_0 is controlled around 50°C to achieve the prescribed Reynolds number of 2.27×10^6. This Reynolds number is selected considering the total pressure limit of the wind tunnel. To force the boundary layer around the wind tunnel model to be turbulent, trip dots are adhered on the wings, horizontal tailplanes, and fuselage nose. The trip dots, with a diameter of 1.27 mm and spaced 2.54 mm apart, are located at 10% chord of the wings and 1.5% station of the fuselage. Table 4.5 lists the heights of the trip dots.

Table 4.5 Trip dot heights for the wind tunnel test.

Part	Height [mm]
From the side of body to the Yehudi break	0.099
From the Yehudi break to the mid-wing	0.089
From the mid-wing to the wing tip	0.079
horizontal tailplanes	0.079
Nose	0.079

The horizontal tailplanes are attached to the fuselage at a deflection angle of 0°, and the nacelles and pylons are removed. This configuration is named as WBT0. The sideslip angle is fixed at 0°. The Mach number calculated using plenum chamber static pressure is set at $M_{\mathrm{pc}} = 0.7$, 0.83, 0.85, 0.86, and 0.87. However, in this dissertation, only the results at $M_{\mathrm{pc}} = 0.85$ are discussed. The pitch angle of the model support system is varied between −2° and 4.25°. Specifically they are set at −2.00° to −1.00° by 0.50°, −0.75°, −0.50° to 1.00°, and 1.25° to 4.25° by 0.25°. The actual attack angles are calculated considering the

support sting bending and the wind tunnel wall interferences.

4.3.2 Wind Tunnel Test of NTF

The data obtained from the WTT campaign of NTF to be compared with that of JAXA are at the Mach number of 0.85 and Reynolds number of 5.0×10^6 [19]. Similar to the test campaign in JAXA, the WBT0 configuration is used. Pressure tap locations on the main wings are almost common for both WTT models, and the main wing deformations are measured in the NTF as well. The pitch angle of the model support sytem are specifically set at $-3.00°$; $-2.00°$, $-1.50°$ to $1.50°$ by $0.50°$, $1.75°$ to $5.00°$ by $0.25°$, and $5.50°$ to $12.00°$ by $0.50°$. The wall interferences are corrected using Ulbrich's method [34].

4.3.3 Used Data

The data used in this dissertation are tabulated as follows:

Table 4.6 Wind Tunnel Data.

Parameter	NTF	JTWT
Reynolds Number (Re)	5×10^6	2.27×10^6
Mach Number (M_{pc})	0.85	0.85
Attack angle (α) [deg]	-1.9 – 5.0	-2.8 – 10.25
Wall Interference Correction	Ulbrich [34]	Mokry [32]
Model Deformation Measurement	Stereo Cameras	Stereo Cameras

4.4 Data Reduction and Correction

4.4.1 Classical Wind Tunnel Corrections

The flow angle is corrected using inverted pitch run data in which the wind tunnel model is set upside down. The flow deflection angle in pitch is calculated from the C_L difference between the inverted run and the case with the upright wind tunnel model. Next, the Mach number correction based on the difference between the test section static pressure, which is measured using a static pressure probe located in the empty wind tunnel, and the plenum chamber pressure is applied. Additionally, buoyancy correction using the longitudinal static pressure distribution along the centerline of the empty test section measured by a long static pressure probe is applied. Next, the wall-interference correction method by Mokry [32] is

performed utilizing the pressure distributions measured on the centerline of the wind-tunnel wall surfaces. Details of the wall-interference corrections are explained by Kohzai *et al.* [11].

4.4.2 Reynolds Number Corrections

The Reynolds number of the JTWT test is set at a lower value (2.27×10^6) than that of the NTF and CFD tests (5.0×10^6). To compare the results, Reynolds number correction method using the skin friction coefficient of a flat plate is applied. The correction is computed as the difference between the estimated parasite drag at the Reynolds number of the JTWT test and those of the NTF and CFD tests. By considering the study by Raymer [5], parasite drag is built up using the following equation as the sum of friction drags of each component:

$$C_{D0} = \frac{\Sigma \left(C_f \cdot FF \cdot Q \cdot S_{\text{wet}} \right)}{S_{\text{ref}}}, \tag{4.1}$$

where C_f is the friction drag of each component, FF is the "form factor," which estimates the pressure drag due to viscous separation, Q is the interference effect factor and S_{wet} is the wetted area of the component. Raymer [5] stated that the fuselage has a negligible interference factor ($Q = 1.0$) in most cases and the interference will be negligible for a well-filleted low wing. Therefore, in this study, Q was set to 1.0 for all cases.The skin friction coefficient of a flat plate in fully-turbulent flow is computed by [5]

$$C_f = \frac{0.455}{\left(\log_{10} Re \right)^{2.58} \left(1 + 0.144 M^2 \right)^{0.65}}, \tag{4.2}$$

and the form factors of the wings and tailplane were computed as follows:

$$FF = \left\{ 1 + \frac{0.6}{(x/c)_m} \left(\frac{t}{c} \right)^4 \right\} \left\{ 1.34 M^{0.18} \left(\cos \Lambda_m \right)^{0.28} \right\}, \tag{4.3}$$

where the term "$(x/c)_m$" is the chord-wise location of the airfoil maximum thickness point, t_{wing} is the thickness of the wing, c is the chord length, and Λ_m refers to the sweep of the maximum-thickness line. The fuselage form factor is computed as

$$FF = \left(1 + \frac{60}{f^3} + \frac{f}{400} \right), \tag{4.4}$$

where

$$f = \frac{l}{d} = \frac{l}{\sqrt{(4/\pi)A_{\max}}}.$$

In addition, l is length of the body, d is a reference diameter of the body, and $A_{\max}$ is the maximum cross-sectional area of the body.

Next, the correction for the Reynolds number difference is calculated as

$$\Delta C_{D0} = C_{D0}|_{Re=5\times10^6} - C_{D0}|_{Re=2.27\times10^6}\,. \tag{4.5}$$

4.4.3 Model Deformation Corrections

To allow fair comparison among various data sources, the data should be aligned to that of the design shape at the designated free-air conditions. Flow conditions of WTT results are corrected through conventional wind tunnel corrections. However, the wind tunnel model is deformed by dynamic pressure during the period the wind blows and these deformation effects, which affect pressure distributions mainly on the main wings, should be elucidated.

The force/moment balance output is also affected by model deformations because the change in wing twist distribution alters the pressure distribution so that the net force differs from that of the design shape. Therefore, corrections for net aerodynamic forces are desirable to compare data from different sources. Moreover, the wing deformation effects of both the NTF and JTWT test results are corrected to those of the "as-built" geometry used in the CFD analysis. Although the main wings are deformed in the bending and twisting directions, it is reported that only twisting has significant effect on the aerodynamic characteristics [39]. Thus, only the twist effect is considered in this dissertation.

The twist angle increment due to dynamic pressure differs at each wing section. In this dissertation, the model deformation correction is applied to the pressure distribution at nine pressure-measurement wing sections. Then, the pressure distributions are integrated to aerodynamic forces. The difference between the aerodynamic forces calculated from deformed-wing pressure distribution and corrected pressure distribution is the required correction for net aerodynamic forces.

4.4.3.1 Pressure Distribution Correction

The pressure distribution at each pressure-measurement wing section is replaced with that at the body-angle-of-attack, which is subtracted by the twist increment due to model deformation. Thus, the wing pressure data are mostly replaced by data acquired at higher body-angles-of-attack as described in Fig 4.9. The pressure distribution without increment is calculated through the interpolation of pressure distributions at the existing attack angles. The interpolation is performed using Akima spline [93] to mitigate degeneracy of pressure jumps related to shock waves. As wing deformation data were acquired at a limited number of wing sections, the data are interpolated using cubic splines to reflect the continuous change of twist along the wing to obtain a twist increment at each pressure measurement section. Although the twist increment of the data to be replaced and that of the replacing data could be different, such a secondary error is ignored in this dissertation.

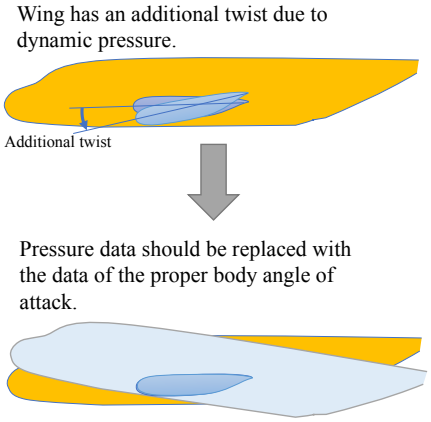

Figure 4.9 Schematic diagram of pressure distribution correction for model deformation.

4.4.3.2 Section Force Distribution Correction

To accomplish aerodynamic force corrections due to wind-tunnel model deformation, surface pressure data are again used. Numerical integration of the surface pressures at each wing section allows pressure contribution on two-dimensional lift (c_l) and drag (c_d) to be

approximated as follows:

$$c_n = \sum_{i=1}^{N-1} (x(i+1) - x(i)) \frac{c_p(i+1) + c_p(i)}{2} + (x(1) - x(N)) \frac{c_p(1) + c_p(N)}{2}, \tag{4.6}$$

$$c_a = -\sum_{i=1}^{N-1} (z(i+1) - z(i)) \frac{c_p(i+1) + c_p(i)}{2} - (z(1) - z(N)) \frac{c_p(1) + c_p(N)}{2}, \tag{4.7}$$

$$c_l = c_n \cos\alpha - c_a \sin\alpha, \tag{4.8}$$

$$c_d = c_a \cos\alpha + c_n \sin\alpha. \tag{4.9}$$

The basic concept of these equations was described by Barlow *et al.* [31]. In these equations, i is the index of each pressure port in a wing section, numbered sequentially from the trailing edge of the upper surface to the trailing edge of the lower surface through the leading edge (Fig. 4.10). These can be replaced by data at the proper attack angles acquired by subtracting the change in the wing twist angle interpolated at each wing section, similar to that in the correction of section pressure distributions.

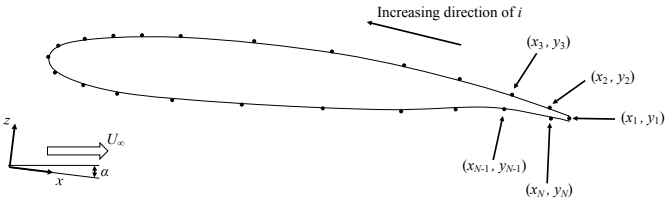

Figure 4.10 Image of pressure integral around an airfoil.

4.4.3.3 Force Coefficient Corrections

The spanwise integration of section force coefficients replaced by data at the proper attack angles produces forces that would be exerted if the shape of the wind-tunnel model is not deformed by dynamic pressure.

$$C_{L\text{wing}} = \sum_{j=1}^{M} (c_l(j)\Delta b)\,, \tag{4.10}$$

$$C_{D\text{wing}} = \sum_{j=1}^{M} (c_d(j)\Delta b)\,, \tag{4.11}$$

where Δb is the spanwise width of a wing section. Without pressure replacement, the integral calculates the force actually exerted under the conditions of deformation by dynamic pressure. The difference between these two integrals can be expected to yield corrections for force coefficients.

$$\Delta C_{L\text{wing deformation}} = C_{L\text{wing}}\big|_{\text{corrected}} - C_{L\text{wing}}\big|_{\text{deformed}}\,, \tag{4.12}$$

$$\Delta C_{D\text{wing deformation}} = C_{D\text{wing}}\big|_{\text{corrected}} - C_{D\text{wing}}\big|_{\text{deformed}}\,. \tag{4.13}$$

Finally, C_L and C_D are corrected as follows:

$$C_{L\text{corrected}} = C_L + \Delta C_{L\text{wing deformation}}, \tag{4.14}$$

$$C_{D\text{corrected}} = C_D + \Delta C_{D0} + \Delta C_{D\text{wing deformation}}, \tag{4.15}$$

where ΔC_{D0} is given by Eq. (4.5).

4.5 Results

4.5.1 Model Deformation Data

Fig. 4.11 shows model deformation measurement results for the wing twist of the CRM in the JTWT at $M_{\mathrm{pc}} = 0.85$. Although wing-bending deformation exists, it can be ignored for aerodynamic characteristics corrections, as stated in Section 4.4.3. This shows that the "real" attack angle at the wing tip is almost 1° less than the model body's attack angle when the body-angle-of-attack is 3°, due to twisting of the wing. The wing of the NTF model will also twist although in a slightly different manner because of differences in the material, model construction, and wind-tunnel conditions. This implies that fair comparisons between wind tunnels cannot be achieved without model deformation corrections as well as comparison with CFD. The attack angles at each wing section must be corrected.

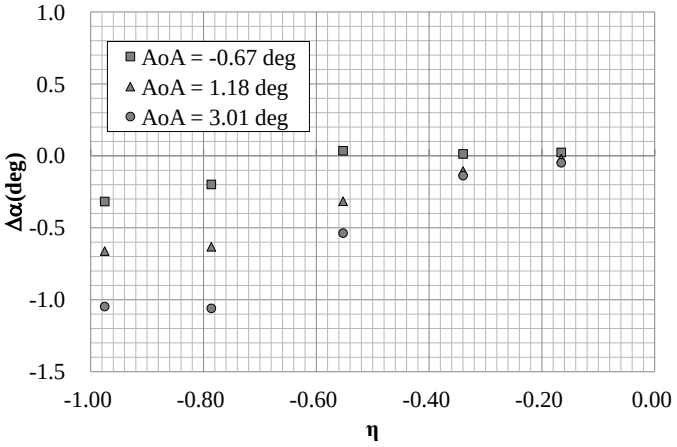

Figure 4.11 Model deformation in twist of the CRM left wing.

4.5.1.1 Pressure Distribution

The apparent effect of model deformation corrections on the pressure distribution is seen at the wing tip. Both the uncorrected and corrected pressure distributions at Section I ($\eta = 0.950$) are shown in Figs. 4.12–4.15. The pressure distributions from JAXA's WTT at Reynolds number of 2.27×10^6, JAXA's CFD test at Reynolds number of 5×10^6, and NASA NTF's WTT at Reynolds number of 5×10^6 are shown. Data interpolated at four

attack angles, 1°, 2°, 3° and 4°, are compared. Dynamic pressure generally twists a swept-back wing from its original shape, resulting in the reduction of attack angle at each wing section. Thus, the uncorrected negative pressure distributions on upper surface of the wing section appear to be of lower magnitude than those predicted by CFD of the design shape. However, when wing deformation corrections are applied, both wind tunnel data sets move closer to the CFD predictions while the shock location is different, especially at higher attack angles.

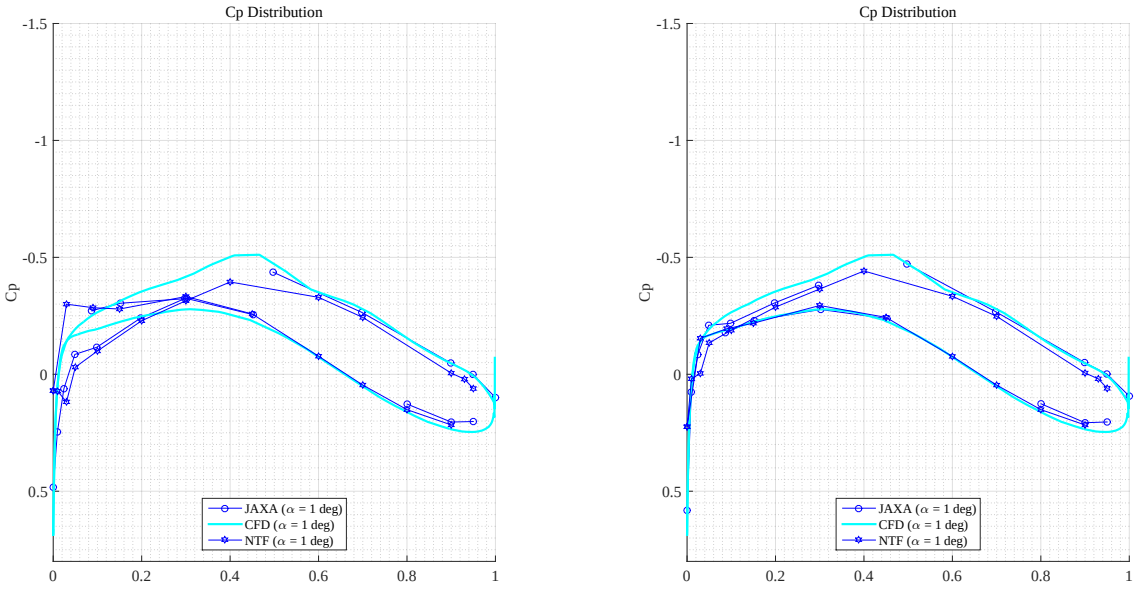

(a) Without wing deformation correction.

(b) With wing deformation correction.

Figure 4.12 Pressure distributions of Section I ($\eta = 0.950$) at $\alpha = 1.0°$.

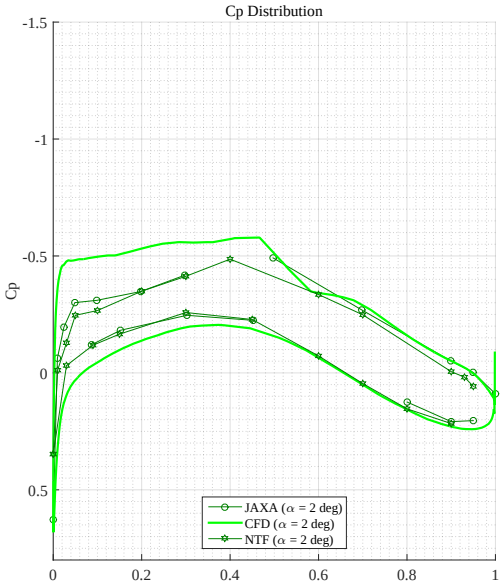

(a) Without wing deformation correction.

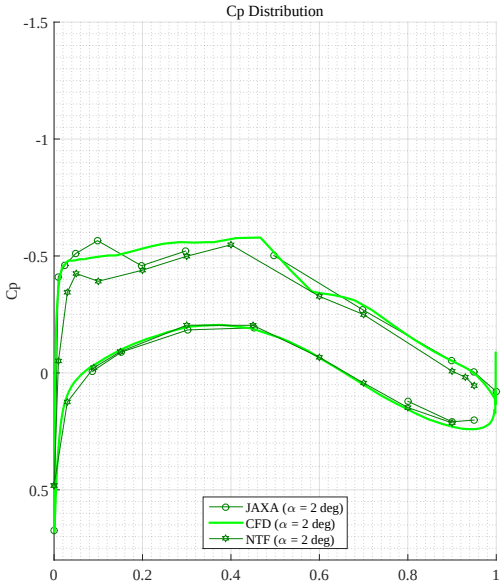

(b) With wing deformation correction.

Figure 4.13 Pressure distributions of Section I ($\eta = 0.950$) at $\alpha = 2.0°$.

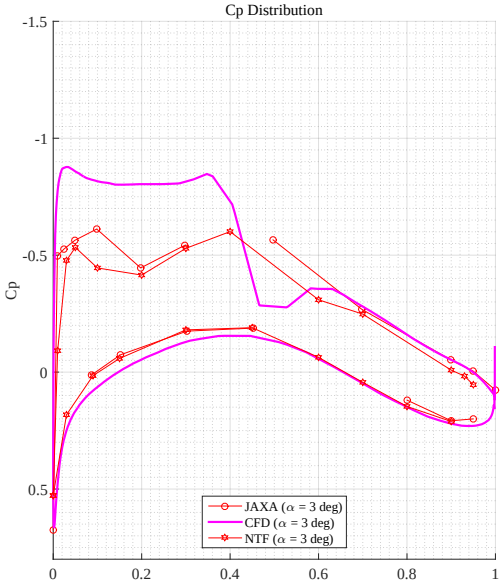

(a) Without wing deformation correction.

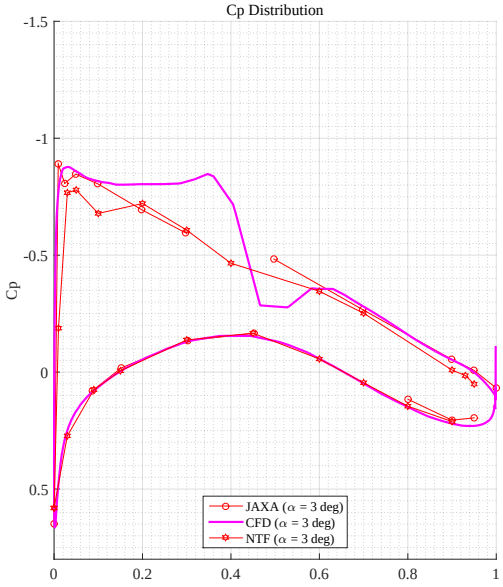

(b) With wing deformation correction.

Figure 4.14 Pressure distributions of Section I ($\eta = 0.950$) at $\alpha = 3.0°$.

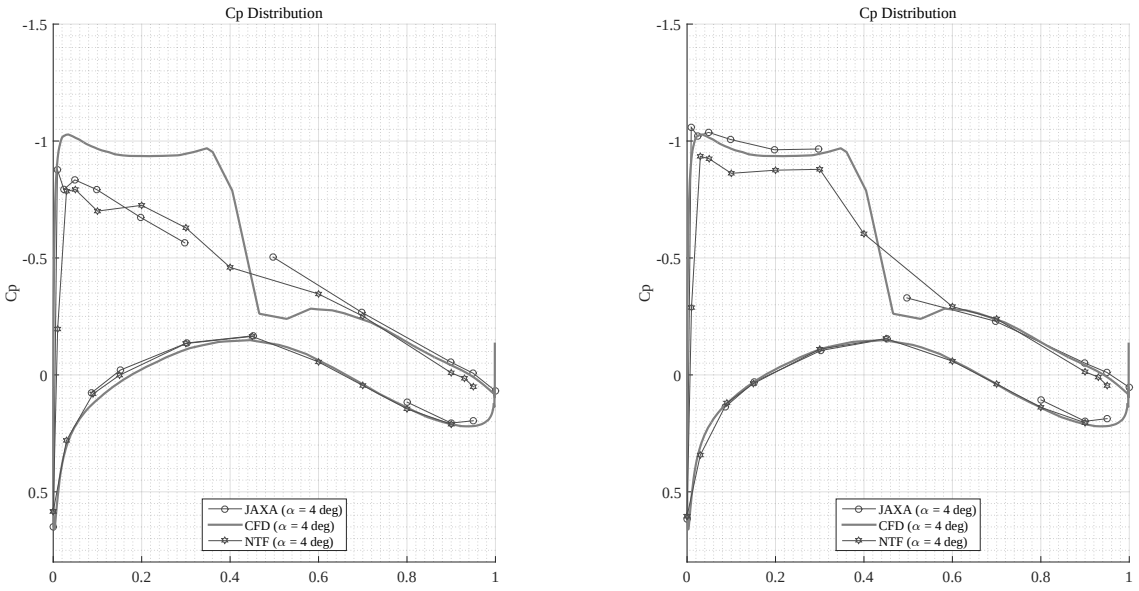

(a) Without wing deformation correction.

(b) With wing deformation correction.

Figure 4.15 Pressure distributions of Section I ($\eta = 0.950$) at $\alpha = 4.0°$.

4.5.1.2 Section Force Distribution

The lift distributions acquired using Eq. (4.8) are plotted in Figs. 4.16–4.19. The CFD lift distributions are calculated using the data at the same discrete wing sections of the WTTs. With deformation correction, the experimental lift distributions at attack angles of 1° and 2° move closer to the CFD results, while the lift distributions of the middle portion of the wing at the higher attack angles fail to agree and the NTF lift distributions are generally smaller than those of the JTWT. The pressure distribution at Section F ($\eta = 0.603$) in Figs. 4.20–4.23 shows that the wing deformation correction in this case succeeds to adjust the top roof of the negative pressure profile on the upper surface; however, the shock locations are not changed at attack angles of 3° and 4°. This generates discrepancies at higher attack angles.

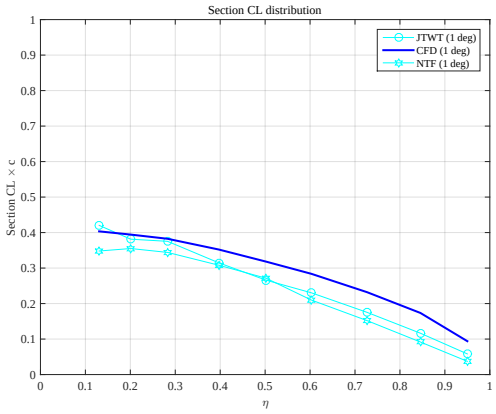

(a) Without wing deformation correction.

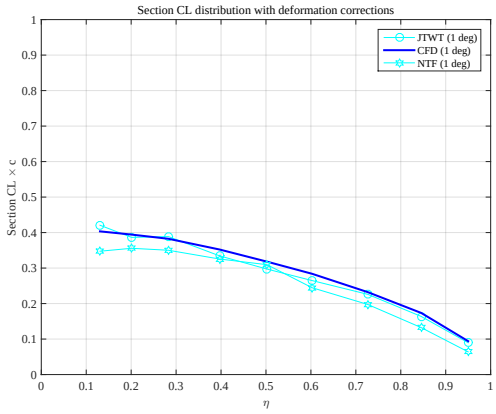

(b) With wing deformation correction.

Figure 4.16 Lift distributions on the wing: JTWT, CFD, and NTF data at $\alpha = 1.0°$.

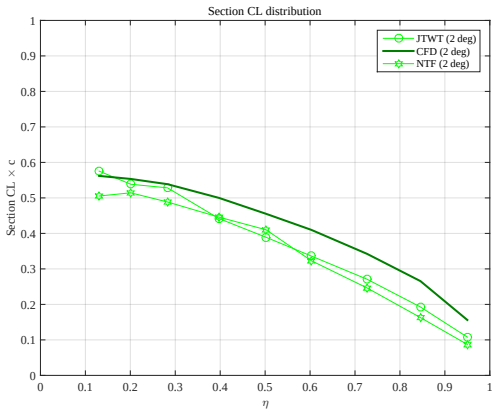

(a) Without wing deformation correction.

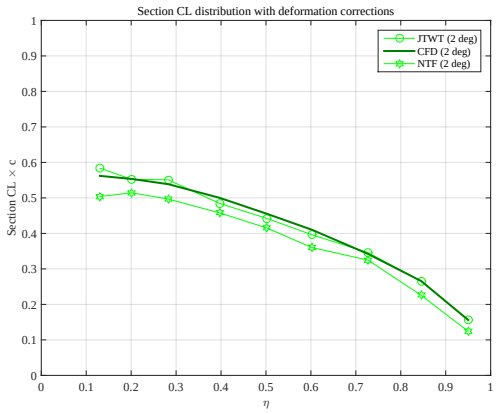

(b) With wing deformation correction.

Figure 4.17 Lift distributions on the wing: JTWT, CFD, and NTF data at $\alpha = 2.0°$.

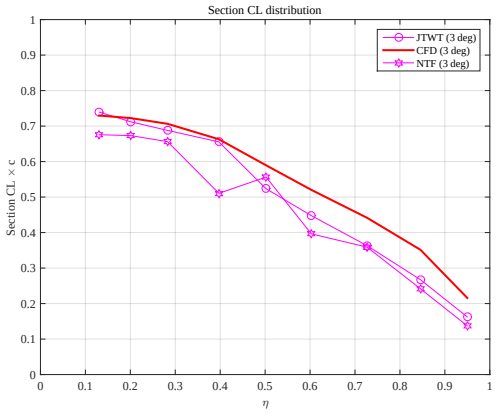

(a) Without wing deformation correction.

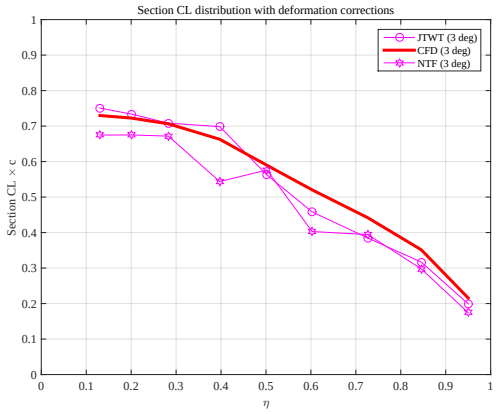

(b) With wing deformation correction.

Figure 4.18 Lift distributions on the wing: JTWT, CFD, and NTF data at $\alpha = 3.0°$.

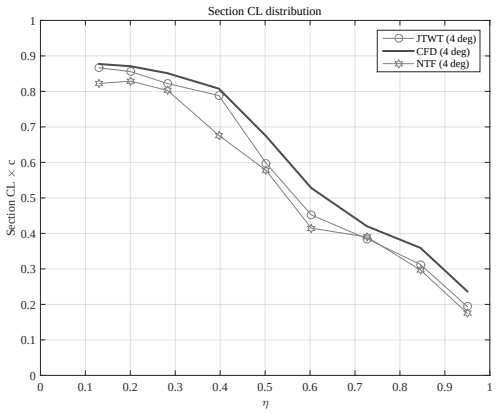

(a) Without wing deformation correction.

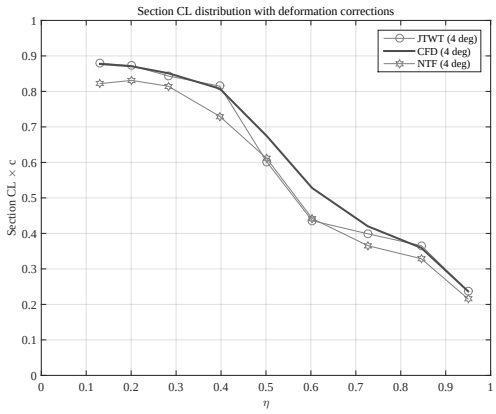

(b) With wing deformation correction.

Figure 4.19 Lift distributions on the wing: JTWT, CFD, and NTF data at $\alpha = 4.0°$.

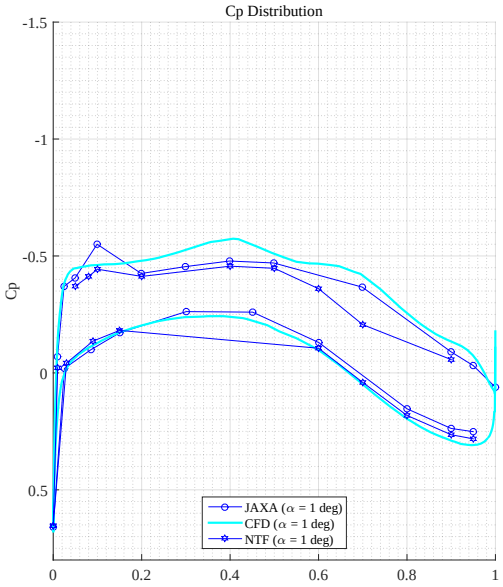

(a) Without wing deformation correction.

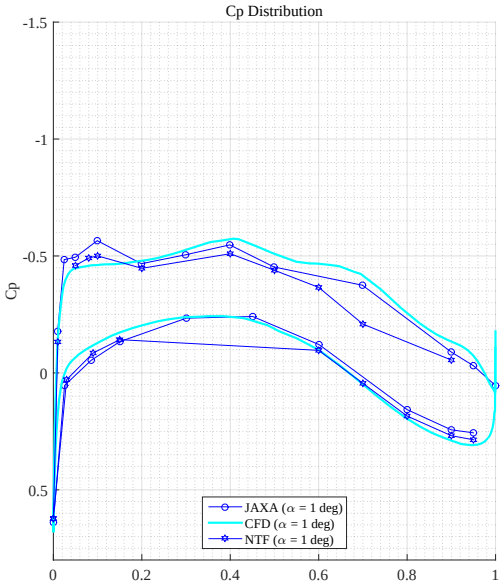

(b) With wing deformation correction.

Figure 4.20 Pressure distributions of Section F ($\eta = 0.603$) at $\alpha = 1.0°$.

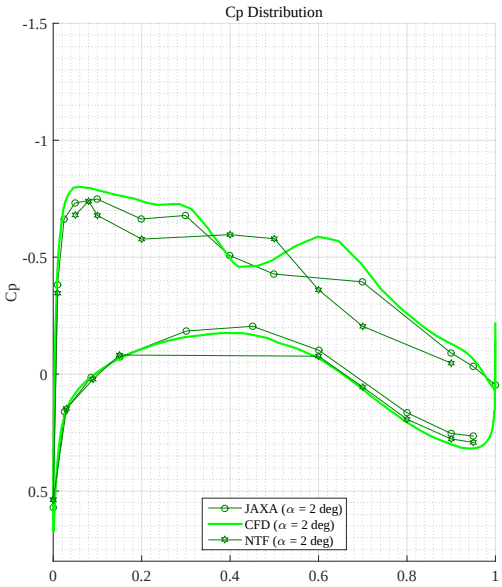

(a) Without wing deformation correction.

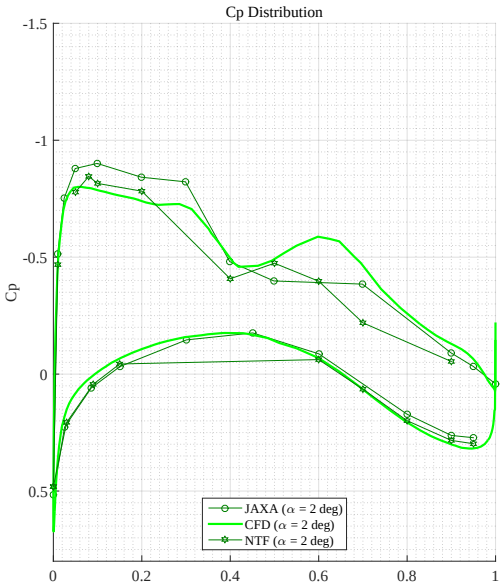

(b) With wing deformation correction.

Figure 4.21 Pressure distributions of Section F ($\eta = 0.603$) at $\alpha = 2.0°$.

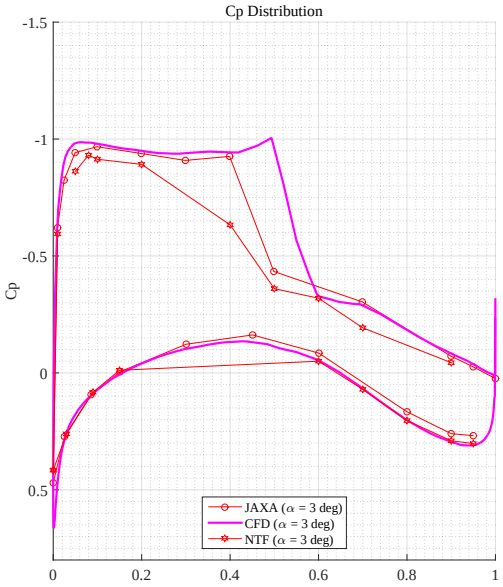

(a) Without wing deformation correction.

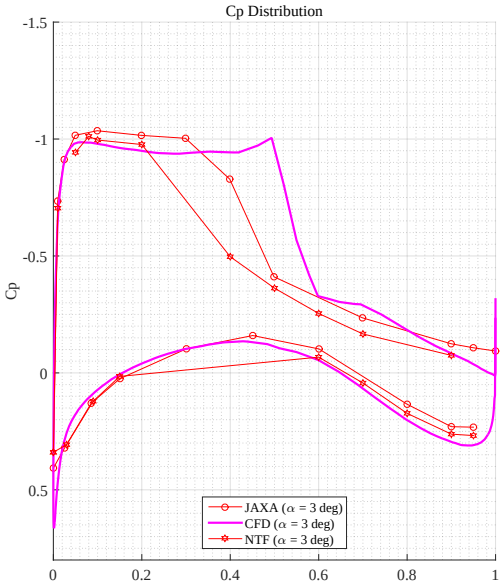

(b) With wing deformation correction.

Figure 4.22 Pressure distributions of Section F ($\eta = 0.603$) at $\alpha = 3.0°$.

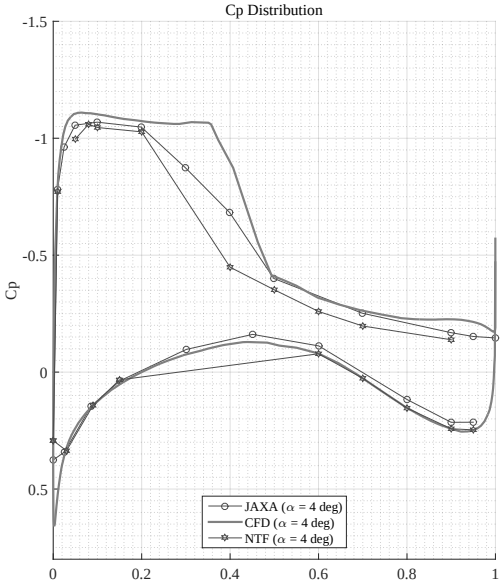

(a) Without wing deformation correction.

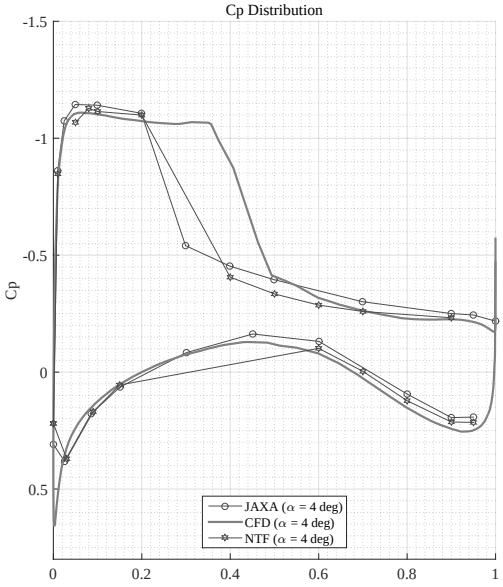

(b) With wing deformation correction.

Figure 4.23 Pressure distributions of Section F ($\eta = 0.603$) at $\alpha = 4.0°$.

For the differences between the JTWT and the NTF lift distributions, a negative pressure peak is found at the leading edge of the pressure distributions on the lower surface of some wing sections of the NTF, such as Section A shown in Fig. 4.24. This peak is not usual and generates significant lift loss when it is computed through integrated pressure distribution. Additional discrepancies are observed between the NTF and JTWT cases at Section D ($\eta = 0.397$). Fig. 4.25 shows that at Section D, several pressure ports of the NTF test are missing on the upper surface. This considerably affects the calculated lift distribution and explains the existence of discrepancies larger than 0.15 at around $\eta = 0.4$.

Thus, pressure distribution corrections by using model deformation information are validated to be feasible, and the lift distribution integration is possible unless there are no significant anomalies included in the pressure distribution data.

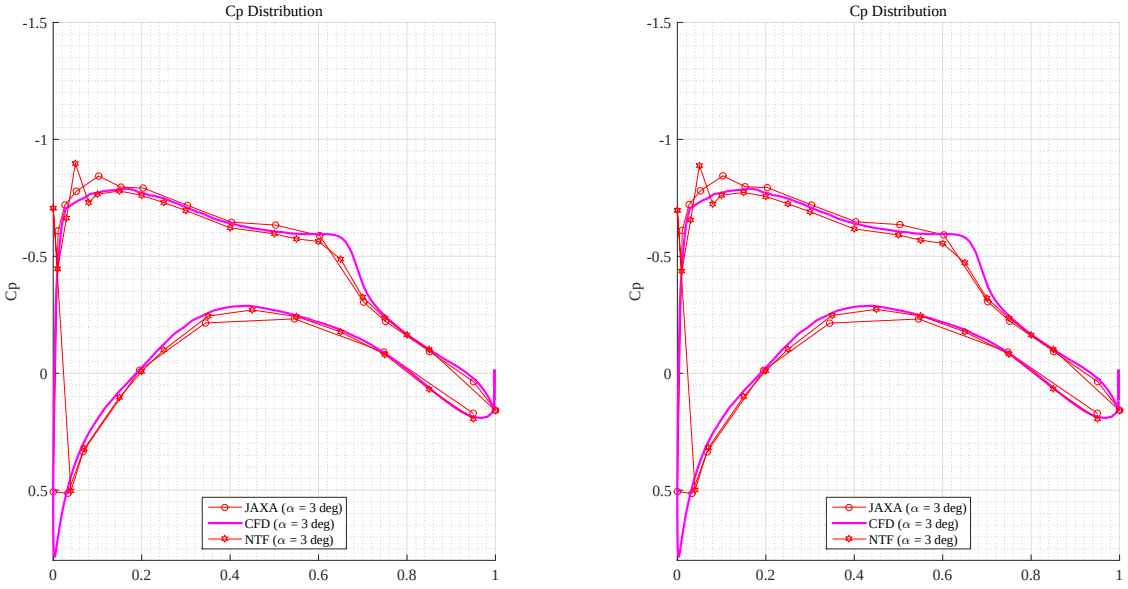

(a) Without wing deformation correction.

(b) With wing deformation correction.

Figure 4.24 Pressure distributions of section A ($\eta = 0.131$) at $\alpha = 3.0°$.

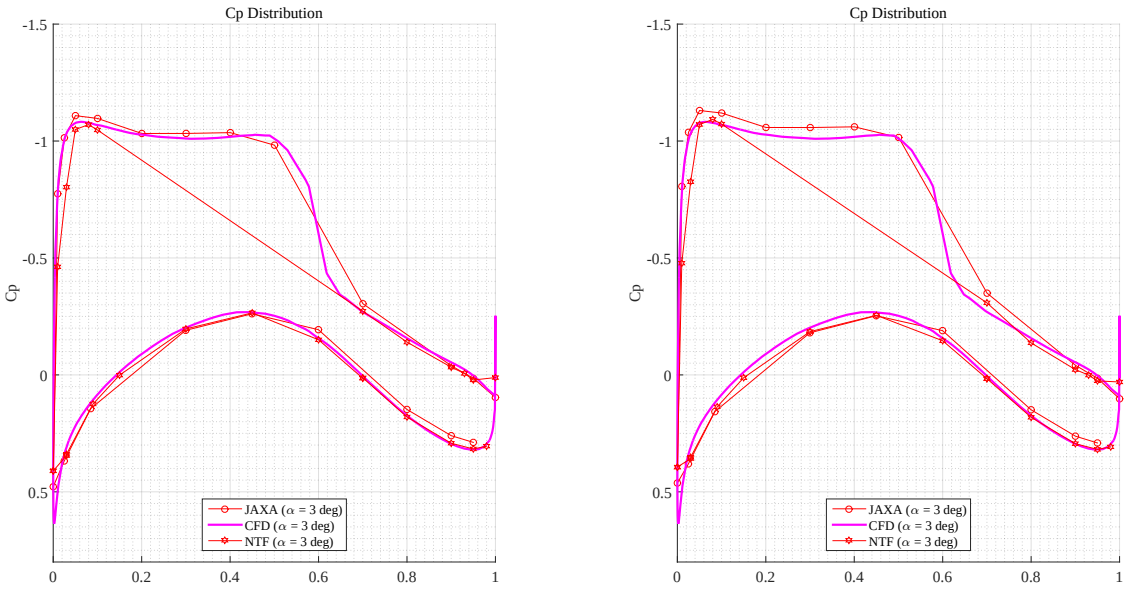

(a) Without wing deformation correction.

(b) With wing deformation correction.

Figure 4.25 Pressure distributions of section D ($\eta = 0.397$) at $\alpha = 3.0°$.

The comparison of oil-flow images on the upper surface of the wing between the CFD (Fig. 4.26) and JTWT wind tunnel data (Fig. 4.27) reveals that the shock location of the WTT is further upstream than in the CFD prediction, and the separation behind the shock in the WTT is narrower than in the CFD prediction, in which it reaches the outer part of the wing. Although the outer part of the wing is twisted in the direction of reducing local attack angles through dynamic pressure, the separation in the WTT does not reach the outside portion of the wings as predicted by CFD, even at an attack angle approximately 5° (Fig 4.26(d) and 4.27(c)). For this type of comparison, the CFD must be run using the same shape as that of the wind tunnel model.

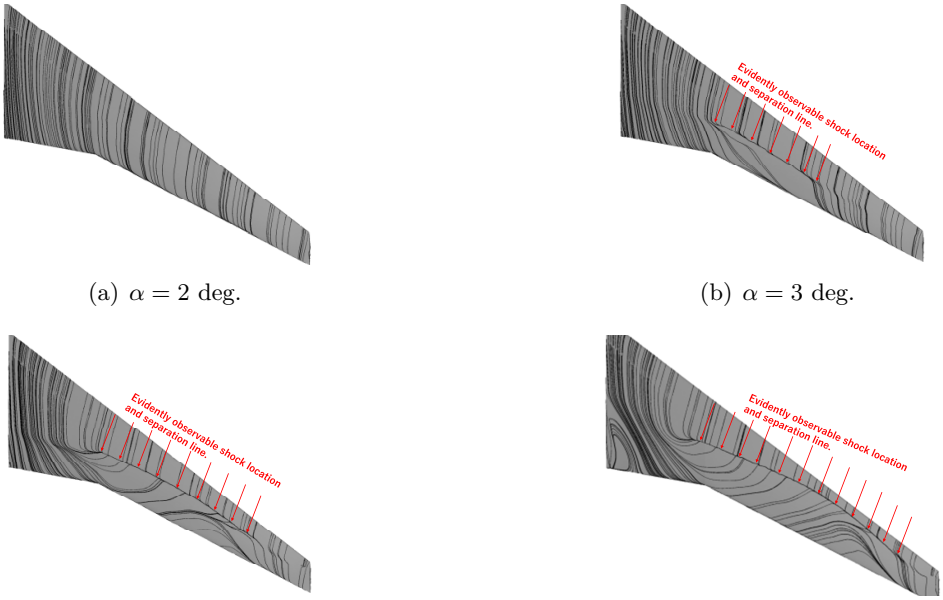

(a) $\alpha = 2$ deg.

(b) $\alpha = 3$ deg.

(c) $\alpha = 4$ deg.

(d) $\alpha = 5$ deg.

Figure 4.26 Oil-flow images on the wing upper surface of CFD.

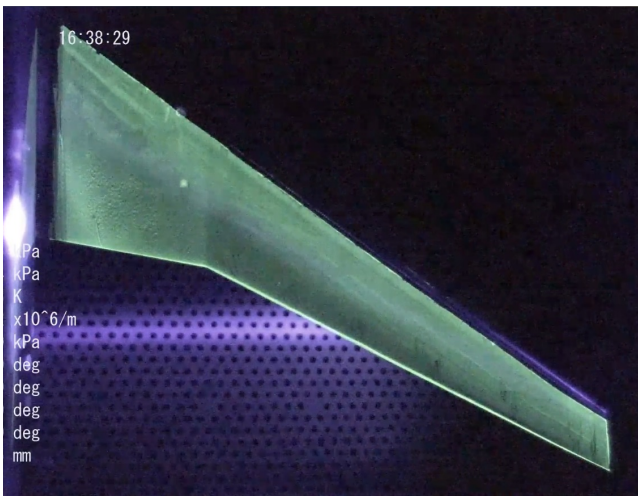

(a) $\alpha = 1.93$ deg (Oil-flow at JTWT).

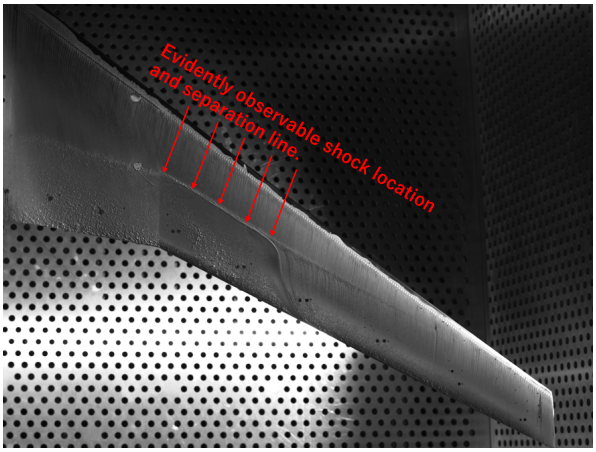

(b) $\alpha = 3.1$ deg (Oil-flow at JTWT [59]).

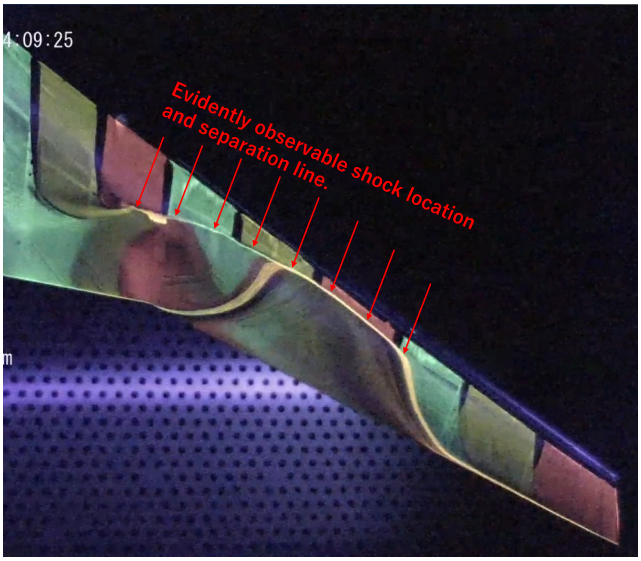

(c) $\alpha = 4.73$ deg (Oil-flow at JTWT ; 3-colors are painted in tern to clarify the stream lines only in this case).

Figure 4.27 Oil-flow images on the wing upper surface acquired in the JTWT.

4.5.1.3 Quantitative Evaluation of Pressure Distribution Improvement

To quantitatively evaluate the improvement of pressure distribution through model deformation correction, the root mean squares (RMSs) of the differences between the pressure coefficient of WTT and CFD results at the pressure ports of the wind-tunnel model are calculated (Figs. 4.28 and 4.29). The figures plot RMSs of the pressure coefficient difference of each wing section against the normalized spanwise section location (η). If the effective attack angle of each wing section is corrected, the difference between the WTT and CFD is expected to be closer, because the CFD is computed using the designed shape, while still including numerical error.

All the figures show that the use of wing deformation correction generates smaller RMS at the wing root (η is minimum as expected). The effective attack angle at each wing section is corrected as closer to the CFD's, which is computed with the designed shape. However, around the mid-wing at $\eta = 0.6$, there are some sections for which the correction increases the differences. This leads to the lift distribution discrepancies illustrated in Figs. 4.16–4.19. In such cases, the roof of the negative pressure distribution on the upper surface of the wing section seems to be corrected but the shock location of the corrected wind-tunnel pressure distribution and that of the CFD are different.

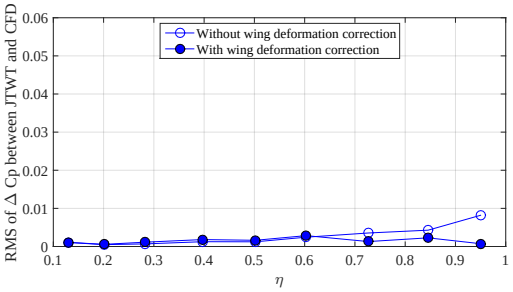

(a) $\alpha = 1°$

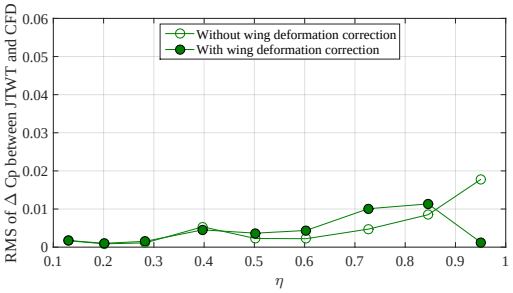

(b) $\alpha = 2°$

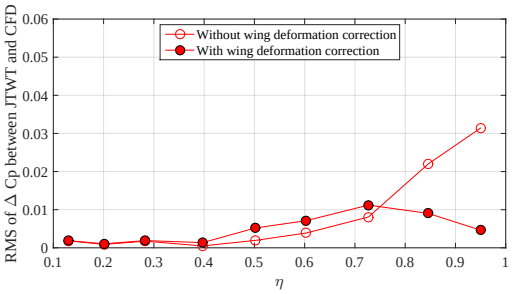

(c) $\alpha = 3°$

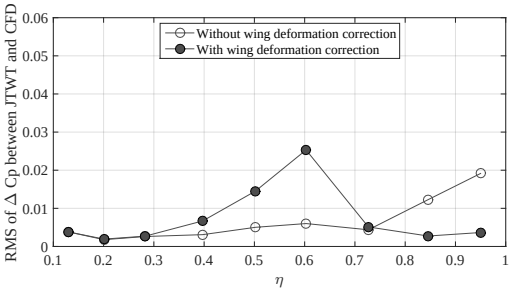

(d) $\alpha = 4°$

Figure 4.28 RMS of pressure difference between JTWT and CFD.

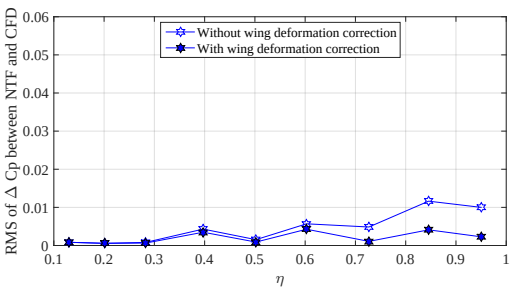

(a) $\alpha = 1°$

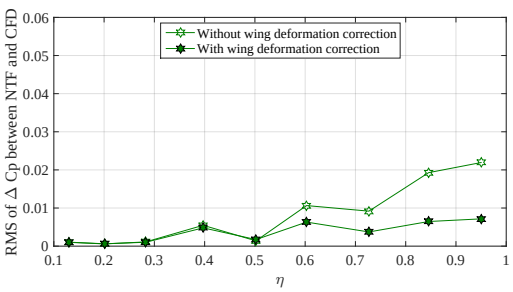

(b) $\alpha = 2°$

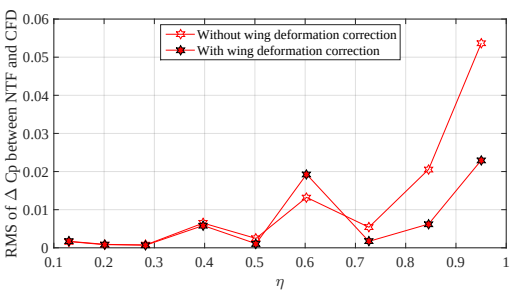

(c) $\alpha = 3°$

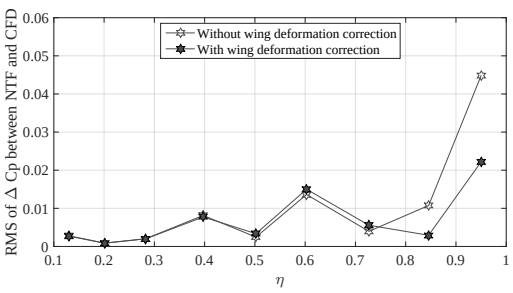

(d) $\alpha = 4°$

Figure 4.29 RMS of pressure difference between NTF and CFD.

4.5.2 Force Coefficient

Here, the effect of force coefficient corrections for wing deformation explained in Section 4.4.3.3 is examined.

4.5.2.1 C_L vs α

Wing deformation correction is substantially effective on the lift characteristics (Fig. 4.30). Without deformation correction, the value of the lift coefficients obtained through WTTs are consistently lower than the CFD predicted values (Fig. 4.30(a)). However, with deformation correction, the WTT lift curves move closer to the CFD results (Fig. 4.30(b)), while the improvement of the NTF data is not enough because of the pressure anomalies explained in Section 4.5.1.2. Although the CFD results undergo numerical errors, the shape of the model in CFD is the design shape, and its lift is not sensitive to the numerical errors as drag. The maximum difference between the CFD and JTWT in the linear region ($C_L \leq 0.5$) is improved from $\Delta C_L \approx 0.060$ to $\Delta C_L \approx 0.019$. This improvement is consistent with the result stated by Rivers *et al.* [39]: a CFD estimation performed with a computational grid of deformed wings at WTT conditions.

4.5.2.2 C_D vs α

The correction of drag coefficients is examined in Fig. 4.31. The classical Reynolds number correction (Section 4.4.2) works well, and the corrected drag curve of the JTWT test moves very close to the curve of the NTF. In addition, the differences are less than 3 drag counts, excluding the edges of the curves ($\alpha \leq 1.5^\circ$ and $\alpha \geq 4.5^\circ$), as shown in Fig. 4.31(b). The difference at the edges are less than 10 drag counts. Although wing deformation correction works well for lift characteristics, correction of the drag characteristics increased the discrepancy between the results of the JTWT and the NTF, while their averages move closer to the CFD curve at higher angles of attack (Fig. 4.31(c)). The cause of the discrepancy has not been clear, but it can be assumed that lack of chord-wise spatial interval of the pressure measurement brought the deterioration because the drag component is more sensitive to the surface slope between pressure ports than the lift force.

4.5.2.3 Drag Polar

The impact of the corrections on the drag polars is also shown in Fig. 4.32. Similarly to the drag coefficients, agreement among the JTWT, NTF and CFD data improves with the Reynolds number corrections of the JTWT results as shown in Fig. 4.32(b), but applying deformation corrections to the wind tunnel test data increased discrepancy (Fig. 4.32(c)).

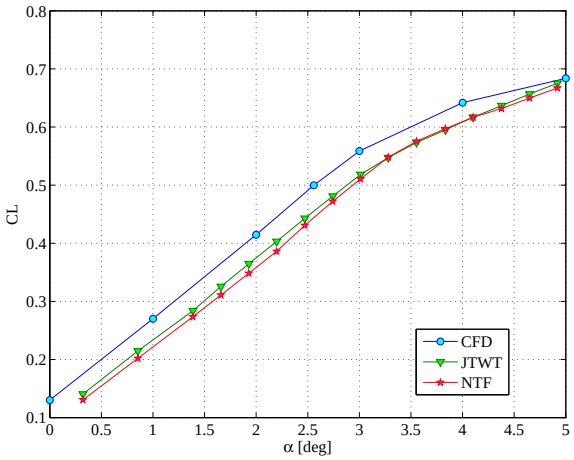

(a) Without wing deformation correction.

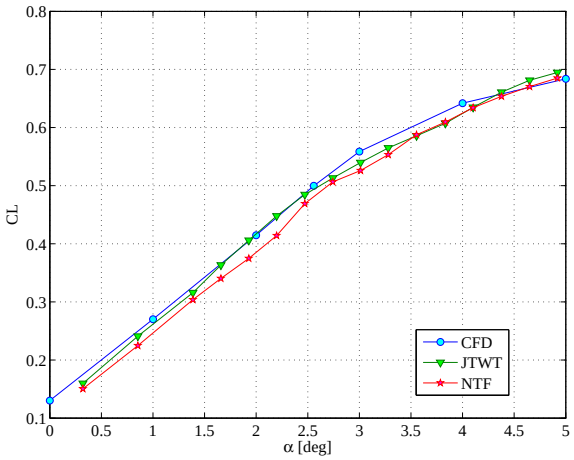

(b) With wing deformation correction.

Figure 4.30 C_L versus α of the CRM acquired in the JTWT.

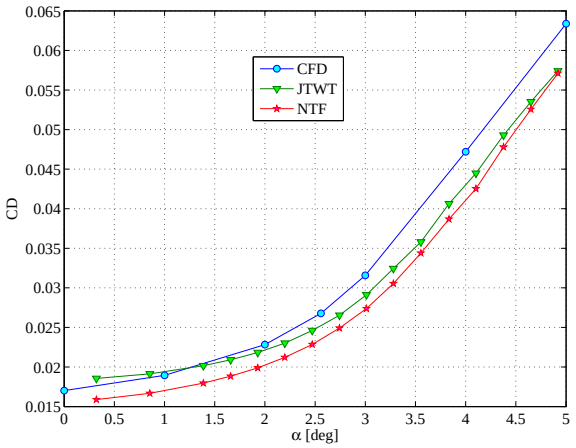

(a) Without Reynolds number and wing deformation corrections.

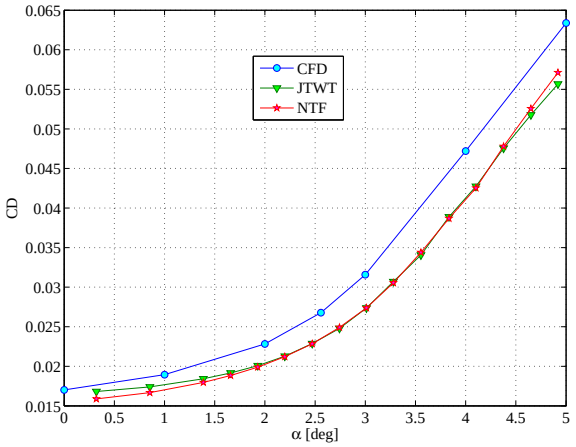

(b) With Reynolds number correction but without wing deformation correction.

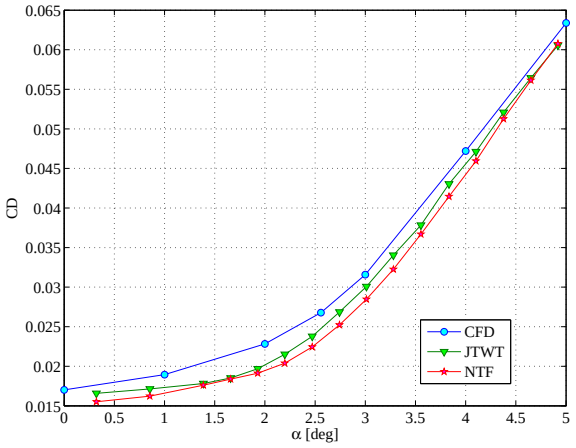

(c) With Reynolds number and wing deformation corrections.

Figure 4.31 C_D versus α of the CRM acquired in the JTWT.

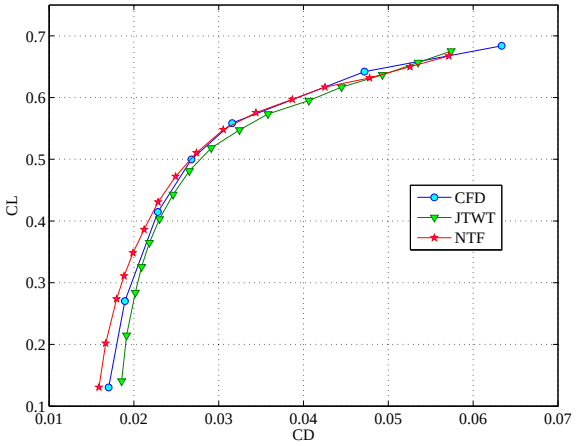

(a) Without Reynolds number and wing deformation corrections.

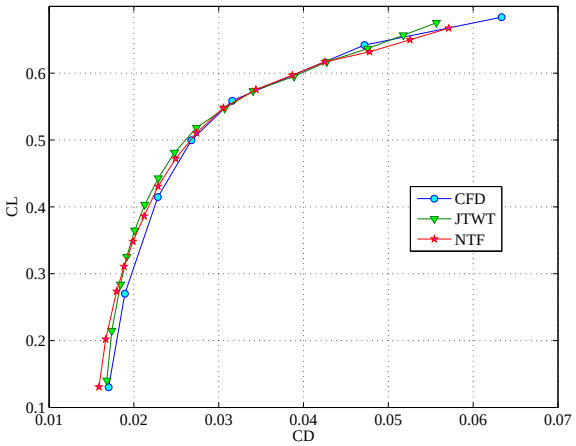

(b) With Reynolds number correction but without wing deformation correction.

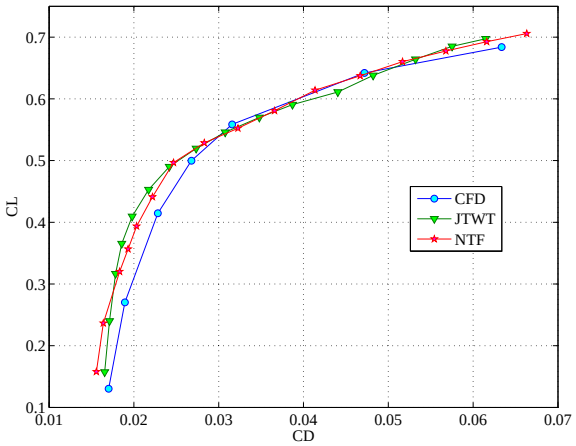

(c) With Reynolds number and wing deformation corrections.

Figure 4.32 C_L versus C_D of the CRM acquired in the JTWT.

4.6 Conclusions

The application of deformation corrections on the transonic WTT data of the NASA CRM improves the agreement between the CFD and WTT. The correction method introduced in this study uses only experimental data contrary to the previous correction methods [47, 39].

Finally, the following conclusions were drawn regarding the overall aerodynamic lift and drag:

- The wing deformation correction is extremely effective for lift coefficient characteristics such that the difference between the CFD and JTWT in the linear region ($C_L \leq 0.5$) is improved from $\Delta C_L \approx 0.060$ to $\Delta C_L \approx 0.019$, provided that integrated pressure distribution does not include significant anomalies.

- The correction is achieved by integrating pressure distribution corrections for the main wings by using optically measured model deformation data. The model deformation correction effectively reduces the difference between the pressure distributions of the WTT data of the deformed main wings and the CFD of the designed shape.

- Reynolds number correction based on turbulent friction estimation successfully achieves good agreement between the drag coefficients of the JTWT and NTF data, in which the Reynolds numbers are 2.27×10^6 and 5×10^6, respectively.

- The wing deformation correction increases the discrepancy in the drag coefficient between the JTWT and NTF data. Drag calculation through pressure integration is extremely difficult and correction methods based on the same method for the lift force correction are probably not practical.

- Although the twist increment of the data to be replaced and that of the replacing data could be different, such a secondary error was ignored in this study.

- The applied corrections discussed in this Chapter are significantly effective for studies of pressure distribution and lift but are insufficient for examining drag. Nevertheless, correction methods are crucial for aligning the data at the design conditions to allow fair comparisons between the data from various sources. Therefore, further improvement of such methods is necessary.

Chapter 5

Conclusions

This study aims to improve methods of estimating aerodynamic characteristics of transport airplanes by both saving the cost in CFD and keeping errors in WTT reasonably small.

First, the extrapolated true value of the drag-coefficient C_D of the NASA CRM was validated by applying the drag-decomposition method on the CFD-acquired flow fields. The grid dependence has been a repetitive theme in the AIAA DPW; however, the cause of the drag increments cannot be clarified using the conventional surface integral. This study showed that the drag dependence on grid density in the DPW-IV is brought only by the spurious drag, and the flow structure reproduced by every level of grid density is consistent. As a result, the difference between the C_D values estimated using the present method, with every single CFD simulation, and using the conventional extrapolation (Richardson extrapolation using simulations for three grid sizes) was found to be less than 1.5 drag counts. In addition, it was shown that the coarsest grid with 2.8 million cells used in the study is almost the lowest limit of spurious drag removal because of interference between the spurious and wave drags. These results are important because the NASA CRM is one of the most widely used transonic transport shape to validate CFD results, and the displayng of the lower limit of the grid density provides a good standard to choose the appropriate grid size to use in airplane development.

Second, a new technique, which employs the concept of the determination of the boundary layer thickness of the Baldwin–Lomax turbulence model, is introduced to determine the domain that should be integrated for the profile drag of the drag decomposition method. It can estimate the profile-drag domain more efficiently without iteration than the conventional method, which requires iterative computations to determine the domain. The

iterative computations are required to determine the values of the sensors to detect the profile-drag and wave-drag domains and the extensions of the detected domains described in Sections 2.2.3.2.2 and 2.2.3.2.3.

The new method successfully detects the boundary-layer-related drag production domain, and has the following advantages over the conventional Tognaccini's boundary layer function, which has been widely used for the drag decomposition method:

- No multiple drag decomposition calculations are required to determine the proper domain to be integrated.
- Drag productions around the leading edge and the domains close to the wall are detected automatically.
- Drag production around the boundary layer edge is well detected.

Practically, by using the conventional method, 200 repetitions of the drag decomposition process were required for determining an appropriate boundary layer domain in the example in this dissertation, whereas by using the newly developed method, only one analysis is required to acquire the integral domain. Thus, the efficiency is improved and a part of the arbitrariness of the conventional drag decomposition method is solved.

Finally, this paper presents the data correction in WTT. A method that corrects the model deformation only by using the data from WTT without CFD support was introduced; conventional approaches [47, 39] have been using CFD to correct the model deformation. Thus, the corrected results were not affected by the numerical errors inherent in CFD. First, the correction method corrects the pressure distribution by using optically measured model deformation data. Then, the net aerodynamic forces are calculated by numerically integrating the corrected pressure. The new method reduces the error in the lift coefficient, ΔC_L from 0.060 to 0.019 by modifying the pressure distribution by using the measured model deformation. The deformation corrections are significantly effective for studying the pressure distribution and lift; however, they are insufficient for examining the drag. Nevertheless, the correction techniques used to align the data at the design conditions are crucial for allowing a fair comparisons among the data from various sources. Therefore, further improvement of such techniques is necessary.

The results of this dissertation contribute to the reduction of both the cost in CFD and error unavoidable in WTT for the estimation of aerodynamic characteristics of transonic

transport airplanes. These include the more accurate and efficient estimations of aerodynamic drag at a lower cost by using CFD with the drag decomposition method than with the conventional surface integral, and the estimation of the aerodynamic characteristics of the designed shape in WTT by correcting the model deformation.

Bibliography

[1] Vassberg, J. C., DeHaan, M. A., Rivers, S. M., and Wahls, R. A., "Development of a Common Reesearch Model for Applied CFD Validation Studies," AIAA Paper 2008–6919, 26th AIAA Applied Aerodynamics Conference, Aug. 2008.

[2] Ueno, M. and Tognaccini, R., "Practical Aspects of Drag Decomposition Analysis on Computational Fluid Dynamics Data (in Japanese)," *Proceedings of the 41st JSASS Annual Meeting*, Japan Society for Aeronautical and Space Sciences, Tokyo, April 2010.

[3] Wind Tunnel Technology Center, "2m × 2m Transonic Wind Tunnel," Brochure of Japan Aerospace Exploration Agency.

[4] Vassberg, J. C., Tinoco, E. N., Mani, M., Rider, B., Zickuhr, T., Levy, D. W., Brodersen, O. P., Eisfeld, B., Crippa, S., Wahls, R. A., Morrison, J. H., Mavriplis, D. J., and Murayama, M., "Summary of the Fourth AIAA Computational Fluid Dynamics Drag Prediction Workshop," *Journal of Aircraft*, Vol. 51, No. 4, 2014, pp. 070–1089.

[5] Raymer, D. P., *Aircraft design: A conceptual approach*, AIAA education series, American Institute of Aeronautics and Astronautics, Reston, Va., 3rd ed., 1999.

[6] John D. Anderson, J., *A History of Aerodynamics: And Its Impact on Flying Machines*, Cambridge Aerospace Series, Cambridge University Press, Cambridge, UK, new ed., Jan. 1999.

[7] Garretson, D., Mair, H., Martin, C., Sullivan, K., and Teichman, J., "Review of CFD Capabilities," IDA Document D–3145, Institute for Defense Analyses, Alexandria, VA, Sept. 2005.

[8] Forrester T. Johnson, Edward N. Tinoco, N. J. Y., "Thirty years of development and application of CFD at Boeing Commercial Airplanes, Seattle," *Computers & Fluids*, Vol. 34, No. 10, Dec. 2005, pp. 1115–1151.

[9] Seedhouse, E., *Virgin Galactic: The First Ten Years*, Springer, 2015.

[10] Morisaki, Y., Hase, S., Takenaka, K., Sugiura, T., and Murayama, M., "Wind Tunnel Testing for Thrust Reverser (in Japanese)," Tech. rep., The Japan Society for Aeronautical and Space Sciences, 49th Aircraft Symposium, 2011.

[11] Kohzai, M., Ueno, M., Koga, S., and Sudani, N., "Wall Interference Corrections of a NASA Common Research Model in JAXA Wind Tunnel Tests," AIAA Paper 2013–0963, 51st AIAA Aerospace Sciences Meeting Including the New Horizons Forum and Aerospace Exposition, Jan. 2013.

[12] Yokokawa, Y., Murayama, M., Ito, T., and Yamamoto, K., "Experiment and CFD of a High-lift Configuration Civil Transport Aircraft Model," AIAA Paper 2006–3452, 25th AIAA Aerodynamic Measurement Technology and Ground Testing Conference, San Francisco, CA, June 2006.

[13] Slotnick, J., Khodadoust, A., Alonso, J., Darmofal, D., Gropp, W., Lurie, E., and Mavriplis, D., "CFD Vision 2030 Study: A Path to Revolutionary Computational Aerosciences," NASA Contractor Report NASA/CR-2014-218178, NASA, Langley Research Center, Hampton, Virginia, March 2014.

[14] Levy, D. W., Zickuhr, T., Vassberg, J., Agrawal, S., Wahls, R. A., Pirzadeh, S., and Hemsch, M. J., "Data Summary from the First AIAA Computational Fluid Dynamics Drag Prediction Workshop," *Journal of Aircraft*, Vol. 40, No. 5, Sept.–Oct. 2003, pp. 875–882.

[15] Laflin, K. R., Klausmeyer, S. M., Zickuhr, T., Vassberg, J. C., Wahls, R. A., Morrison, J. H., Brodersen, O. P., Rakowitz, M. E., Tinoco, E. N., and Godard, J.-L., "Data Summary from Second AIAA Computational Fluid Dynamics Drag Prediction Workshop," *Journal of Aircraft*, Vol. 42, No. 5, Sept.–Oct. 2005, pp. 1165–1178.

[16] Vassberg, J. C., Tinoco, E. N., Mani, M., Brodersen, O. P., Eisfeld, B., Wahls, R. A., Morrison, J. H., Zickuhr, T., Laflin, K. R., and Mavriplis, D. J., "Abridged Sumary of

the Third AIAA Computational Fluid Dynamics Drag Prediction Workshop," *Journal of Aircraft*, Vol. 45, No. 3, May–June 2008, pp. 781–798.

[17] Levy, D. W., Laflin, K. R., Tinoco, E. N., Vassberg, J. C., Mani, M., an Christopher L. Rumsey, B. R., Wahls, R. A., Morrison, J. H., Brodersen, O. P., Crippa, S., Mavriplis, D. J., and Murayama, M., "Summary of Data from the Fifth Computational Fluid Dynamics Drag Prediction Workshop," *Journal of Aircraft*, Vol. 51, No. 4, July–Aug. 2014, pp. 1194–1213.

[18] Rivers, M. B. and Dittberner, A., "Experimental Investigation of the NASA Common Research Model," AIAA Paper 2010–4258, 28th AIAA Applied Aerodynamics Conference, Chicago, Illinois, July 2010.

[19] Rivers, M. B. and Dittberner, A., "Experimental Investigations of the NASA Common Research Model in the NASA Langley National Transonic Facility and NASA Ames 11-Ft Transonic Wind Tunnel," AIAA Paper 2011–1126, 49th AIAA Aerospace Sciences Meeting Including the New Horizons Forum and Aerospace Exposition, Jan. 2011.

[20] Blakrishna, S. and Acheson, M. J., "Analysis of NASA Common Research Model Dynamic Data," AIAA Paper 2011–1127, 49th AIAA Aerospace Sciences Meeting including the New Horizons Forum and Aerospace Exposition, Orlando, FL, Jan. 2011.

[21] Bell, J. H., "Pressure-Sensitive Paint Measurements on the NASA Common Research Model in the NASA 11-ft Transonic Wind Tunnel," AIAA Paper 2011–1128, 49th AIAA Aerospace Sciences Meeting including the New Horizons Forum and Aerospace Exposition, Orlando, FL, Jan. 2011.

[22] Zilliac, G. G., Pulliam, T. H., Rivers, M. B., Zerr, J., Delgado, M., Halcomb, N., and Lee, H., "A Comparison of the Measured and Computed Skin Friction Distribution on the Common Research Model," AIAA Paper 2011–1129, 49th AIAA Aerospace Sciences Meeting including the New Horizons Forum and Aerospace Exposition, Orlando, FL, Jan. 2011.

[23] Rivers, M. B., Rudnik, R., and Quest, J., "Comparison of the NASA Common Research Model European Transonic Wind Tunnel Test Data to NASA Test Data," AIAA Paper 2015–1093, 53rd AIAA Aerospace Sciences Meeting, Kissimmee, Florida, 2015.

[24] Taylor, N. J., Gammon, M., and Vassberg, J. C., "The NASA Common Research Model: a Geometry-Handling Perspective," AIAA Paper 2016–3486, 46th AIAA Fluid Dynamics Conference, Washington, D.C., June 2016.

[25] Mavriplis, D. J., Vassberg, J. C., Tinoco, E. N., Mani, M., Brodersen, O. P., Eisfeld, B., Wahls, R. A., Morrison, J. H., Zickuhr, T., Levy, D., and Murayama, M., "Grid Quality and Resolution Issues from the Drag Prediction Workshop Series," *Journal of Aircraft*, Vol. 46, No. 3, 2009, pp. 935–950.

[26] Paparone, L. and Tognaccini, R., "Computational Fluid Dynamics-Based Drag Prediction and Decomposition," *AIAA Journal*, Vol. 41, No. 9, Sept. 2003, pp. 1647–1657.

[27] Sclafani, A. J., DeHaan, M. A., Vassberg, J. C., Rumsey, C. L., and Pulliam, T. H., "Drag Prediction for the Common Research Model Using CFL3D and OVERFLOW," *Journal of Aircraft*, Vol. 51, No. 4, July–Aug. 2014, pp. 1101–1117.

[28] Slooff, J., "Computational Drag Analysis and Minimization: Mission Impossible?" *Aircraft Drag Prediction and Reduction*, AGARD-R-723, Addendum 1, AGARD, 1986.

[29] Tognaccini, R., "Methods for Drag Decomposition, Thrust-Drag Bookkeeping from CFD Calculations," *CFD-Based Aircraft Drag Prediction and Reduction*, VKI Lecture Series 2003-02, von Karman Institute for Fluid Dynamics, Belgium, Nov. 2003.

[30] Destarac, D., "Far-field / Near-field Drag Balance and Applications of Drag Extraction in CFD," *CFD-Based Aircraft Drag Prediction and Reduction*, VKI Lecture Series 2003-02, von Karman Institute for Fluid Dynamics, Belgium, Nov. 2003.

[31] Barlow, J. B., William H. Rae, J., and Pope, A., *Low-Speed Wind Tunnel Testing*, John Wiley & Sons, Inc., 3rd ed., 1999.

[32] Mokry, M., "Evaluation of Three-Dimensional Wall Interference Corrections from Boundary Pressure Measurements," NRC-LTR-HA 51, National Research Council Canada / Conseil national de recherches Canada, Nov. 1980.

[33] Keller, J. D. and Wright, R. H., "A Numerical Method of Calculating the Boundary-Induced Interference in Slotted or Perforated Wind Tunnels of Rectangular Cross Section," NASA TR R–379, NASA, Nov. 1971.

[34] Ulbrich, N., "The Application of Panel Method Code ANTARES to Wind Tunnel Wall Interference Problems," AIAA Paper 2002–0307, 40th AIAA Aerospace Sciences Meeting & Exhibit, 2002.

[35] Tuttle, M. H. and Gloss, B. B., "Support Interference of Wind Tunnel Models - A Selective Annotated Bibliography," NASA Technical Memorandum 81909, NASA, 1981.

[36] Ericsson, L. E. and Reding, J. P., "Review of Support Interference in Dynamic Tests," *AIAA Journal*, Vol. 21, No. 12, 1983, pp. 1652–1666.

[37] Ueno, M., Yamamoto, Y., Yanagihara, M., Leplat, M., and Oswald, J., "Assessment of Experimental and Computational Transonic Base Pressure Using Flight Data," *Journal of Spacecraft and Rockets*, Vol. 44, No. 6, Nov.–Dec. 2007, pp. 1241–1249.

[38] Hammond, D. G. and C. Wilkerson, J., "An Evaluation of Single and Multiple Sting Support Methods to Obtain Unmodified Interference-free Wind Tunnel Data," AIAA Paper 71–267, AIAA 6th Aerodynamic Testing Conference, Albuquerque, NM, March 1971.

[39] Rivers, M. B., Hunter, C. A., and Campbell, R. L., "Further Investigation of the Support System Effects and Wing Twist on the NASA Common Research Model," AIAA Paper 2012–3209, 30th AIAA Applied Aerodynamics Conference, New Orleans, LO, June 2012.

[40] Kohzai, M., Sudani, N., Yamamoto, K., Ueno, M., and Hashimoto, A., "Experimental and Numerical Studies of Support Interference in the JAXA 2m $\times$ 2m Transonic Wind Tunnel," AIAA Paper 2010–4200, 27th AIAA Aerodynamic Measurement Technology and Ground Testing Conference, Chicago, Illinois, June–July 2010.

[41] Wahls, R. A., "The National Transonic Facility: A Research Retrospective," Aiaa paper 2001–0754, 39th AIAA Aerospace Sciences Meeting and Exhibit, Reno, NV, Jan. 2001.

[42] Green, J. and Quest, J., "A short history of the European Transonic Wind Tunnel ETW," *Progress in Aerospace Sciences*, Vol. 47, No. 5, July 2011, pp. 319–368.

[43] Sighard, F. H., *Fluid-Dynamic Drag*, Hoerner Fluid Dynamics, second edition ed., June 1965.

[44] AGARD Fluid Dynamics Panel Working Group, "Boundary Layer Simulation and Control in Wind Tunnels," AGARD-AR 224, AGARD, April 1988.

[45] Elsenaar, A., T.W., Jr., B., and Stanewsky, E., "Reynolds Number Effects in Transonic Flow," AGARD-AG 303, AGARD, Dec. 1988.

[46] Haines, A. B., "Scale Effects on Aircraft and Weapon Aerodynamics," AGARD-AG 323, AGARD, July 1994.

[47] Yasue, K. and Sawada, K., "Static Aeroelasticity Analysis of Wind Tunnel Model Using Discontinuous Galerkin CFD Solver," AIAA Paper 2009–604, 47th AIAA Aerospace Sciences Meeting Including The New Horizons Forum and Aerospace Exposition, Orlando, FL, Jan. 2009.

[48] Hue, D., "CFD Investigations on the DPW-5 Configuration with Measured Experimental Wing Twist using the elsA Solver and the Far-Field Approach," AIAA Paper 2013–2508, 31st AIAA Applied Aerodynamics Conference, San Diego, CA, June 2013.

[49] Eberhardt, S., Benedict, K., Hedges, L., Robinson, A., and Tinoco, E. N., "Inclusion of Aeroelastic Twist into the CFD Analysis of the Twin-Engine NASA Common Research Model," AIAA Paper 2014–0251, 52nd Aerospace Sciences Meeting, National Harbor, MD, Jan. 2014.

[50] Keye, S., Brodersen, O., and Rivers, M. B., "Investigation of Aeroelastic Effects on the NASA Common Research Model," *Journal of Aircraft*, Vol. 51, No. 4, July–Aug. 2014, pp. 1323–1330.

[51] Yasue, K., Ueno, M., Koga, S., and Kohzai, M., "CFD-Aided Model Deformation Corrections of NASA Common Research Model Wind Tunnel Data," AIAA Paper 2015–0620, 53rd AIAA Aerospace Sciences Meeting, Kissimmee, Florida, Jan. 2015.

[52] Watanabe, S., Kuchi-ishi, S., Murakami, K., Hashimoto, A., Kato, H., Yamashita, T., Yasue, K., and Imagawa, K., "Towards EFD/CFD Integration: Development of DAHWIN - Digital/Analog-Hybrid Wind Tunnel," AIAA Paper 2014–0982, 52nd Aerospace Sciences Meeting, AIAA SciTech Forum, National Harbor, MD, Jan. 2014.

[53] Yamamoto, K., Tanaka, K., and Murayama, M., "Comparison Study of Drag Prediction for the 4th CFD Drag Prediction Workshop using Structured and Unstructured Mesh

Methods," AIAA Paper 2010–4222, 28th AIAA Applied Aerodynamics Conference, June 2010.

[54] Ueno, M., Yamamoto, K., Kentaro, T., Mitsuhiro, M., and Tognaccini, R., "Far-Field Drag Analysis of NASA Common Research Model Simulation," *Journal of Aircraft*, Vol. 50, No. 2, March 2013, pp. 388–397.

[55] Gariépy, M., Malouin, B., Trepanier, J.-Y., and Laurendeau, E., "Far-Field Drag Decomposition Method Applied to the Drag Prediction Workshop 5 Test Cases," *Journal of Aircraft*, Vol. 50, No. 6, Nov.–Dec. 2013, pp. 1822–1831.

[56] Baldwin, B. and Lomax, H., "Thin-layer Approximation and Algebraic Model for Separated Turbulent Flows," AIAA Paper 1978–257, 16th Aerospace Sciences Meeting, 1978.

[57] Rivers, M. B. and Hunter, C. A., "Support System Effects on the NASA Common Research Model," AIAA Paper 2012–0707, 50th AIAA Aerospace Sciences Meeting including the New Horizons Forum and Aerospace Exposition, Nashville, TN, Jan. 2012.

[58] Ueno, M., Kohzai, M., and Koga, S., "JAXA Transonic Wind Tunnel Test of the NASA CRM (Volume 1)," JAXA Research Memorandum JAXA-RM-13-017E, Japan Aerospace Exploration Agency, 2014.

[59] Koga, S., Kohzai, M., Ueno, M., Nakakita, K., and Sudani, N., "Analysis of NASA Common Research Model Dynamic Data in JAXA Wind Tunnel Tests," AIAA Paper 2013–0495, 51st AIAA Aerospace Sciences Meeting Including the New Horizons Forum and Aerospace Exposition, Jan. 2013.

[60] Lutz, T., Gansel, P. P., Waldmann, A., Zimmermann, D.-M., and am Hülse, S. S., "Time-Resolved Prediction and Measurement of the Wake Past the CRM at High Reynolds Number Stall Conditions," AIAA Paper 2015–1094, 53rd AIAA Aerospace Sciences Meeting, Kissimmee, Florida, Jan. 2015.

[61] Maskell, E., "Progress Towards a Method for the Measurement of the Components of the Drag of a Wing of Finite Span," Tech. Rep. Technical Report 72232, RAE, 1972.

[62] Kusunose, K., *A Wake Integration Method for Airplane Drag Prediction*, Vol. 3 of *The 21st Century COE Program International COE of Flow Dynamics Lecure Series*, Tohoku University Press, Sendai, 2005.

[63] Katz, J. and Plotkin, A., *Low-Speed Aerodynamics*, Cambridge Aerospace Series, Cambridge University Press, Cambridge, UK, 2nd ed., 2001.

[64] Takaki, R., Yamamoto, K., Yamane, T., Enomoto, S., and Mukai, J., "The Development of the UPACS CFD Environment," *Proceedings of ISHPC 2003*, High Performance Computing, Springer, 2003, pp. 307–319.

[65] Yamamoto, K., Ochi, A., Shima, E., and Takaki, R., "CFD Sensitivity of Drag Prediction on DLR-F6 Configuration by Structured Method and Unstructured Method," AIAA Paper AIAA–2004–398, 42nd AIAA Aerospace Sciences Meeting and Exhibit, Jan. 2004.

[66] Roe, P., "Approximate Riemann Solvers, Parameter Vectors, and Difference Schemes," *Journal of Computationl Physics*, Vol. 43, 1981, pp. 57–372.

[67] van Albada, G., van Leer, B., and Jr., W. R., "A Comparative Study of Computational Methods in Cosmic Gas Dynamics," *Astronomy and Astrophysics*, Vol. 108, 1982, pp. 76–84.

[68] Shima, E., "A Simple Implicit Scheme for Structured/Unstructured CFD,," *Proceedings of 29th Fluid Dynamics symposium*, Hokkaido, Japan, 1997, pp. 325–328.

[69] Spalart, P. and Allmaras, S., "A One-Equation Turbulence Model for Aerodynamic Flows," Tech. Rep. AIAA 92–0439, 30th Aerospace Sciences Meeting and Exhibit, Reno, NV, Jan. 1992.

[70] van der Vooren, J. and Destarac, D., "Drag/thrust analysis of jet-propelled transonic transport aircraft: Definition of physical drag components," *Aerospace Science and Technology*, Vol. 8, No. 6, Sept. 2004, pp. 545–556.

[71] van der Vooren, J. and Slooff, J., "CFD-Based Drag Prediction; State of the Art, Theory, Prospects," AIAA Professional Studies Series, Course on Drag-Prediction and Measurement TP 90247, NLR, 1990.

[72] Giles, M. B. and Cummings, R. M., "Wake Integration for Three-Dimensional Flowfield Computations: Theoretical Development," *Journal of Aircraft*, Vol. 36, No. 2, March–April 1999, pp. 357–365.

[73] Hunt, D. L., Cummings, R. M., and Giles, M. B., "Wake Integration for Three-Dimensional Flowfield Computations: Applications," *Journal of Aircraft*, Vol. 36, No. 2, Mar.-Apr. 1999, pp. 366–373.

[74] Petrosino, F., *Analisi numerica delle forze aerodinamiche su configuratizoni aeronautiche*, Ph.D. thesis, Università degli Studi di Napoli "Federico II", 2008, *(in Italian language)*.

[75] Cebeci, T., Smith, A., and Mosinskis, G., "Calculation of Compressible Adiabatic Turbulent Boundary Layers," AIAA Paper AIAA 69–687, AIAA Fluid and Plasma Dynamics Conference, June 1969.

[76] Wilcox, D. C., *Turbulence Modeling for CFD*, DCW Industries, Inc., a La Cañada, 3rd ed., 2006.

[77] van Dam, C. P., Nikfetrat, K., Wong, K., and Vijgen, P. M. H. W., "Drag Prediction at Subsonic and Transonic Speeds Using Euler Methods," *Journal of Aircraft*, Vol. 32, No. 4, July–Aug. 1995, pp. 839–845.

[78] Yamazaki, W., *Study of Advanced Aerodynamic Analysis & Shape Optimization Using Drag Decomposition Method*, Ph.D. thesis, Tohoku University, Jan. 2007.

[79] Kohzai, M., Ueno, M., Sudani, N., Hashimoto, A., Aoyama, T., Yamamoto, K., Utaka, Y., Tanaka, K., and Hirai, T., "Improvement to drag measurement and correction in JTWT (in Japanese)," *Proceedings of the 47th Aircraft Symposium*, Japan Society for Aeronautical and Space Sciences, Gifu, Japan, Nov. 2009.

[80] Belter, D. L. and Mejia, K. M., "A Review of Standards Model Testing in The Boeing Transonic Wind Tunnel," AIAA Paper 2002–2789, 22nd AIAA Aerodynamic Measurement Technology and Ground Testing Conference, St. Louis, Missouri, June 2002.

[81] Krynytzky, A. J. and Hergert, D. W., "Boeing Transonic Wind Tunnel Upgrade Assessment," AIAA Paper 2002–2782, 22nd AIAA Aerodynamic Measurement Technology and Ground Testing Conference, St. Louis, Missouri, June 2002.

[82] Sauders, T., "The European Transonic Wind Tunnel – Testing at flight Reynolds numbers," AIAA Paper 96–0227, AIAA 34th Aerospace Sciences Meeting and Exhibit, Reno, NV, Jan. 1996.

[83] Yamazaki, W., Matsushima, K., and Kazuhiro, N., "Aerodynamic Design Optimization using the Drag-Decomposition Method," *AIAA Journal*, Vol. 46, No. 5, May 2008, pp. 1096–1106.

[84] Liepmann, H. W. and Roshko, A., *Elements of Gasdynamics*, Dover Publications, Inc., New York, 2001.

[85] Klebanoff, P. S., "Characteristics of Turbulence in a Boundary Layer with Zero Pressure Gradient," NACA Technocal Note NACA TN 3178, National Advisory Committee for Aeronautics, Washington 25, D. C., July 1954.

[86] Rizzi, A., "Spurious Entropy Production and Very Accurate Solutions to the Euler Equations," *Aeronautical Journal*, Vol. 31, Feb. 1985, pp. 59–71.

[87] Baker, T. J., "Mesh generation: Art or science?" *Progress in Aerospace Sciences*, Vol. 41, No. 1, Jan. 2005, pp. 29 – 63.

[88] Vassberg, J. C. and Jameson, A., "In Pursuit of Grid Convergence for Two-Dimensional Euler Solutions," *Journal of Aircraft*, Vol. 47, No. 4, July–Aug. 2010, pp. 1152 – 1166.

[89] Nakahashi, K., Ito, Y., and Togashi, F., "Some Challenges of Realistic Flow Simulations by Unstructured Grid CFD," *International Journal for Numerical Methods in Fluids*, Vol. 43, No. 6–7, Oct. 2003, pp. 769–783.

[90] Obayashi, S. and Guruswamy, G., "Convergence Acceleration of an Aeroelastic Navier-Stokes Solver," *AIAA Journal*, Vol. 33, No. 6, 1995, pp. 1134–1141.

[91] Sharov, D. and Nakahashi, K., "Reordering of Hybrid Unstructured Grids for Lower-Upper Symmetric Gauss-Seidel Computations," *AIAA Journal*, Vol. 36, No. 3, 1998, pp. 484–486.

[92] Spalart, P., "Strategies for turbulence modelling and simulations," *International Journal of Heat and Fluid Flow*, Vol. 21, 2000, pp. 252–263.

[93] Akima, H., "A New Method of Interpolation and Smooth Curve Fitting Based on Local Procedures," *Journal of the ACM*, Vol. 17, No. 4, Oct. 1970, pp. 589–602.

[94] Redeker, G., "DLR-F4 Wing-Body Configuration," AGARD Report AR–303, AGARD, Aug. 1994.

[95] Redeker, G., Schmidt, N., and Müller, R., "Design and Experimental Verification of a Transonic Wing for Transport Aircraft," *Proceedings of the FDP Symposium on Subsonic/Transonic Configuration Aerodynamics*, No. CP–285, 1980, pp. 13.1–13.7.

[96] Keye, S. and Gammon, M., "Development of Deformed CAD Geometries of NASA's Common Research Model for the Sixth AIAA CFD Drag Prediction Workshop," AIAA Paper 2016–3431, 34th AIAA Applied Aerodynamis Conference, Washington, D.C., 2016.

[97] Atinault, O. and Hue, D., "Design of a Vertical Tail for the CRM Configuration," Technical Report RT 1/21960 GMT/DAAP, ONERA, June 2014.

List of Publications

1. Ueno, M., Yamamoto, K., Tanaka, K., Murayama, M., and Tognaccini, R., "Far-Field Drag Analysis of NASA Common Research Model Simulation," Journal of Aircraft, Vol.50, No.2, pp.388–397, 2013.

2. Ueno, M, and Nakamura, Y., "Refinement of Boundary-Layer Detection for Drag Decomposition of Computational Subsonic Flow Field," Transactions of the Japan Society for Aeronautical and Space Sciences, Aerospace Technology Japan, Vol. 12, pp. 61–69, 2014.

3. Ueno, M., Kohzai, M., Koga, S., Kato, H., Nakakita, K., Sudani, N., and Nakamura, Y., "Normalization of Wind-Tunnel Data for NASA Common Research Model," Journal of Aircraft, Vol.52, No.5, pp.1535–1549, 2015.

Appendix A

A.1 AIAA CFD Drag Prediction Workshop and NASA Common Research Model

The main target of the analyses in this dissertation is, the NASA Common Research Model (CRM), which is produced in relation with the AIAA CFD Drag Prediction Workshop series. First, the series of workshops is introduced. Then, the NASA CRM is explained.

A.1.1 AIAA CFD Drag Prediction Workshops

Drag prediction is one of the most important aspects of aerodynamics in commercial airplane development. For taking over a part of the WTT to be analyzed by the CFD, it is required that CFD and wind tunnel results should be seamlessly combined with each other. To realize this, numerically certified validation of precisions achievable by the CFD is required.

Recently, efforts has been made to utilize the CFD to estimate drag. Since 2001, AIAA CFD Drag Prediction Workshop (DPW) series [14, 15, 16, 4, 17] have been held by the the American Institute of Aeronautics and Astronautics (AIAA) DPW Organizing Committee sponsored by the Applied Aerodynamics Technical Committee of the AIAA to promote and assist such efforts. The DPWs have been functioning as good benchmarks for contemporary industrial CFD techniques to predict drag of transonic transport aircraft in cruising conditions. The details of the workshops are well documented in the literature. In this section, the general outline of the DPWs is briefly described by referring and stating the descriptions of the summarized literature [14, 15, 16, 4, 17].

A.1.1.1 1st AIAA CFD Drag Prediction Workshop

The 1st AIAA CFD Drag Prediction Workshop (DPW-I) was held preceding the 19th AIAA Applied Aerodynamics Conference in 2001. Details of the workshop are summarized in [14]. The objectives of the workshop are as follows [14]:

- To assess the state-of-the-art computational methods as practical aerodynamic tools for aircraft force and moment prediction.
- To provide an impartial forum for evaluating the effectiveness of existing computer codes and modeling techniques using Navier–Stokes solvers.
- To identify areas requiring additional research and development.

The focus of this workshop is on drag prediction accuracy and the DLR German Aerospace Research Center DLR-F4 wing-body configuration test cases [94] have been chosen; they address subsonic wing/body transport configuration flying at subsonic through transonic speeds. In addition, a statistical framework is used to asses the comparisons within the computational results and with the wind tunnel test results.

Eighteen international participants using fourteen codes submitted data to the workshop. The conclusions of the survey are summarized as follows [14]:

- In general, the CFD lift and minimum drag levels are higher than the wind-tunnel results.
- Nonparabolic drag is slightly lower than that obtained through an experiment at higher Mach number/α combinations, that is, postbuffet conditions, where separation is present.
- Although the comparisons with experiments were reasonable, the large amount of scatter does not promote a high level of satisfaction in the results. However, much of the scatter was due to outlier solutions generally agreed to be in error.
- The data show no clear advantage of any specific grid type or turbulence model.

A.1.1.2 2nd AIAA CFD Drag Prediction Workshop

The 2nd AIAA CFD DPW (DPW-II) was held preceding the 21st AIAA Applied Aerodynamics Conference in 2003. Details of the workshop are summarized in [15]. The objectives

of the DPW-I are maintained in the DPW-II, and incremental drag as well as total drag were discussed in the workshop because it was also hypothesized that CFD is better in predicting configuration delta drag than absolute drag [15]. The DLR-F6 model was chosen to compare a transport configuration of a more complex model with nacelles on and off to examine configuration differences. The DLR-F6 configuration was designed by DLR and is derived from the DLR-F4 configuration [95]. In addition, the wing-body (WB) and wing-body-nacelle-pylon (WBNP) configurations are chosen to focus on absolute drag and component drag increment prediction accuracy in the DPW-II. Additionally, influence of tripped boundary-layer transition and fully turbulent boundary-layer was examined.

Data from 22 Navier–Stokes codes were submitted by 25 participants. Although the DPW-II organizing committee envisioned a grid-convergence study as part of the workshop, the various series of coarse, medium, and fine grids used by participants were of insufficient density to obtain asymptotic solution convergence. The comparisons between the DLR-F6 WB and WBNP configurations show that their variations are more extreme than usually considered in CFD delta drag studies. Nevertheless, the results indicate that difference between tripped transition of boundary layer and fully turbulent computations is not critical to estimate drag increment through configuration differences.

A.1.1.3 3rd AIAA CFD Drag Prediction Workshop

The 3rd AIAA CFD DPW (DPW-III) was held preceding the 25th AIAA Applied Aerodynamics Conference in 2006. In addition to the objectives of the 1st and the 2nd DPWs, the objectives of the DPW-III include the identification of areas needing additional research and development [16]. The distinguished feature of this workshop is that it is a "blind" drag prediction by CFD. A priori experimental data was not available for comparison. To suppress the boundary-layer separation around the trailing edge region of the main-wing-body juncture, FX2B fairing is prepared and a new WTT was performed. In addition to the DLR-F6 wing-body with FX2B fairing transport mode, wing-only models, DPW-W1 and -W2, are included to encourage academic participation and allow more exhaustive grid convergence studies.

Fifteen participants submitted multiple data sets for the DLR-F6 WB cases and ten participants submitted data sets for the wing-alone cases.

In the workshop, there still remain several problematic issues [16]:

- Especially for unstructured meshes, generating a consistent set of grids for grid-convergence studies is difficult.
- The separation bubble at the aft-corner of the wing/body juncture continues to be a source of difficulty.

A.1.1.4 4th AIAA CFD Drag Prediction Workshop

The 4th AIAA CFD DPW (DPW-IV) was held preceding the 27th AIAA Applied Aerodynamics Conference in 2009. After three workshops, spatial discretization errors were determined as a dominant error source in absolute and incremental drag predictions [25]. The target model was the NASA CRM, which is a newly designed representative shape of transonic transport aircraft [1]. The specifications of the NASA CRM are briefly summarized in Section A.1.2. A particular aspect of the DPW-IV against the first three workshops is that any WTT result of the NASA CRM including similar shapes was not available before the workshop. Hence, the workshop was completely a blind test. The workshop focused on the prediction of both absolute and differential drag levels for wing-body and wing-body/horizontal-tail configurations.

Three test cases were studied in the workshop [4].

Case 1 was grid convergence and down wash studies at Mach = 0.85. The Reynolds number based on the mean aerodynamic chord (Re_c) and reference temperature were fixed at 5×10^6 and 100 °F (= 310.928 K), respectively. In the grid convergence study, the tail incidence angle was fixed at 0°. Coarse, Medium, Fine, and Extra-Fine grids were prepared. In the downwash study, the effect of downwash of the main wings on the horizontal tails was examined using the Medium grid. Drag polars for $\alpha = 0.0°$, 1.0°, 1.5°, 2.0°, 2.5°, 3.0°, and 4.0° were required. The horizontal tail incidence angles i_H set at −2°, 0°, and +2° and tail off conditions were computed. Trimmed drag polars derived from polars at i_H set at −2°, 0°, and +2° and differential drag polar of tail off versus tail on configuration were also examined.

Case 2 was an optional case and was for studying Mach sweep. Drag rise curves were required at $C_L = 0.400$, 0.450, 0.500 varying Mach numbers for 0.70, 0.75, 0.80, 0.83, 0.85, 0.86 and 0.87 using the Medium grid. The tail incidence angle i_H was fixed at 0°. The Reynolds number and reference temperature were the same as those of the Case 1.

Case 3 was also optional and was for studying a Reynolds number at Mach = 0.85 and

$C_L = 0.500$ by employing the Medium grid. The tail incidence angle $i_H = 0$. Comparisons were performed between $Re_c = 5 \times 10^6$ and 20×10^6. The reference temperature for the $Re_c = 20 \times 10^6$ case was -250 °F.

Although individual results should be referred from the summary paper [4], the combined set of solutions in the DPW-IV clearly showed that there remains room for improvement of the state-of-the-art industrial CFD. However, this conclusion was relaxed by an observation that there exists a core set of CFD methods that consistently agree with each other on all test cases spanning the entire workshop series. Most noteworthy about this core set of solvers was that these methods were based on all grid types [4].

A.1.1.5 5th and 6th AIAA CFD Drag Prediction Workshop

After the DPW-IV, the workshop series is continuing. As the DPW-IV is the main target of this dissertation, the description of those newer workshops are simple.

The 5th AIAA CFD DPW (DPW-V) was held preceding the 30th AIAA Applied Aerodynamics Conference in 2012. The focus of the workshop was to continue studies with the NASA CRM performed in the DPW-IV. The DPW-V focused on force/moment predictions for the NASA CRM wing-body configuration, including a grid refinement study and an optional buffet study [17].

Next, the 6th AIAA CFD Drag Prediction Workshop (DPW-VI) was held during the AIAA Aviation 2016 Conference in 2016. Its summarized paper has not been published at this moment. The focus of this workshop was the NASA CRM with wind-tunnel-measured wing twist [96]; both wing-body and wing-body-nacelle-pylon configurations were considered. CFD predictions of absolute and incremental force and moment values were examined and compared. The workshop included grid convergence and code validation studies. Additionally, an angle-of-attack sweep with static aero-elastic deformations was considered. Grids was made available for all required cases.

A.1.2 NASA Common Research Model

The NASA CRM was newly developed for the 4th AIAA DPW (DPW-IV) as a modern and publicly available geometry to overcome the problems of the previously available geometries. It was also used in the DPW-V and DPW-VI. It is representative of a contemporary transonic commercial transport designed to cruise at $M = 0.85$ and $C_L = 0.5$ at a nominal altitude of 37,000 ft [1, 4]. The CRM fuselage fits with a Boeing 777-200 [97] but the

wing shape was originally designed for the DPW-IV. It comprises main wings, horizontal tails, and removable pylon-nacelles. The horizontal tail settings have three tail incidences of i_H =[−2°, 0°, +2°]. The DPW-IV focused on the prediction of both absolute and differential drag levels for wing-body and wing-body/horizontal-tail configurations of the NASA CRM [4]. The image of the NASA CRM wing-body/horizontal tail configuration is shown in Fig. A.1. The details of the design of the NASA CRM are described in [1], and the reference quantities of the NASA CRM are tabulated in Table A.1.

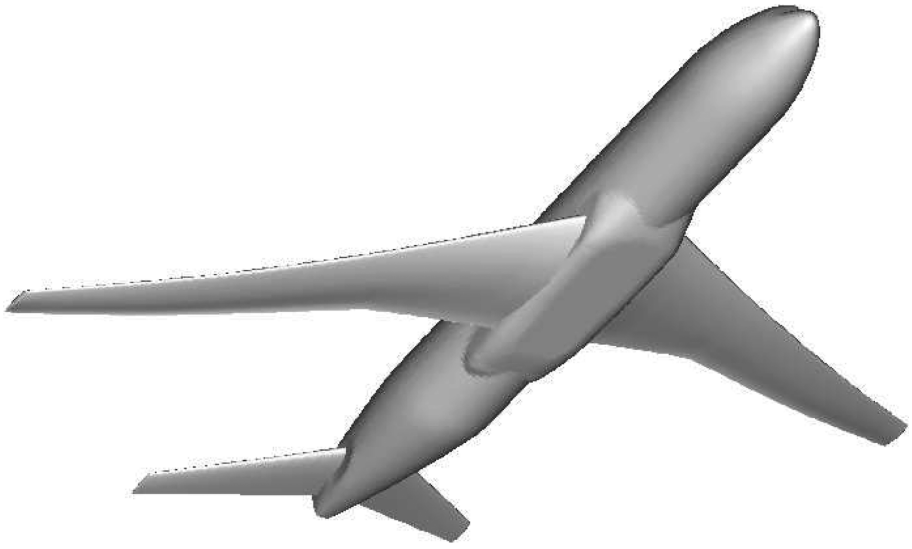

Figure A.1 NASA CRM wing-body/horizontal configuration [4].

Table A.1 Reference Quantities for the NASA CRM [1].

Reference Area, S_{ref}		594,720.0 in^2	383.689.6 m^2
Trap-Wing Area		576,000.0 in^2	371.6 m^2
Reference Chord, c_{ref}		275.80 in	7.0053 m
Span, b		2,313.50 in	58.7629 m
Reference Center	x	1,325.90 in	33.6779 m
	y	468.75 in	11.906 m
	z	177.95 in	5.5199 m
Taper Ratio, λ		0.275	
1/4 Chord Sweep Angle, $\Lambda_{C/4}$		35°	
Aspect Ratio, A		9.0	

The DPW-IV did not only compare the CFD solutions but comparisons were also conducted with the WTT results. As the experimental reference, NASA's Langley Research Center (LaRC) fabricated a wind tunnel model of the NASA CRM on which they conducted tests [18, 19, 20, 21, 22] and have been continuing further analyses [57, 39].

The NASA CRM was originally tested in the National Transonic Facility (NTF) at NASA LaRC and the NASA Ames Research Center 11-by 11-foot Transonic Wind Tunnel for the DPW-IV [18, 19]. The wind tunnel tests were performed after the DPW-IV, and thus the computations were completely a "blind test". The public geometry and exhaustive comparisons through CFD and WTT affected wind tunnel engineering circles as well. The Japan Aerospace Exploration Agency (JAXA) in Japan built an 80% scaled copy of the NASA CRM and conducted tests in the JAXA 2m $\times$ 2m Transonic Wind Tunnel (JTWT) [58, 59, 11]. In contrast, The European Strategic Wind tunnels Improved Research Potential (ESWI^{RP}) performed a high Reynolds number test of the original NASA CRM wind tunnel model of NASA at the European Transonic Windtunnel (ETW) [60, 23]. Eventually, the NASA CRM established its position as a de facto standard aerodynamic shape for a transonic transport.